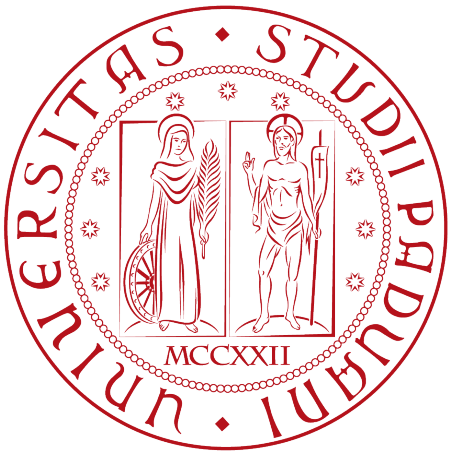


**UNIVERSITÀ DEGLI STUDI DI PADOVA**
**Dipartimento di Fisica e Astronomia "G. Galilei" - DFA**

Corso di dottorato in Fisica
XXIX CICLO

TESI DI DOTTORATO

# The Role of Interfaces in Microfluidic Systems: Oscillating Sessile Droplets and Confined Bacterial Suspensions

Tesi redatta con il contributo finanziario della Fondazione Cariparo

**Coordinatore**: Ch.mo Prof. Gianguido Dall'Agata
**Supervisore**: Ch.mo Prof. Matteo Pierno
**Co-supervisore**: Ch.mo Prof. Giampaolo Mistura

**Dottorando**: Paolo Sartori

*Alla mia famiglia*
*(felini compresi)*

*Gutta cavat lapidem, non bis, sed saepe cadendo:*
*Sic homo fit sapiens, non bis, sed saepe legendo.*

Giordano Bruno - *Il Candelaio* (a. III, sc. 6)

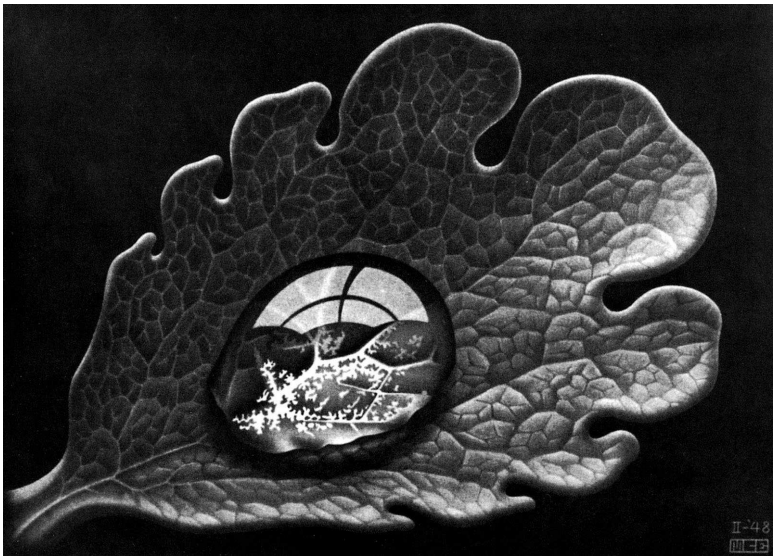

M.C. Escher - *Dewdrop*

# Riassunto

Questa tesi di dottorato prende in esame il ruolo delle interfacce che caratterizzano i sistemi microfluidici, come ad esempio l'interfaccia libera aria/acqua delle gocce o l'interfaccia liquido/solido di fluidi racchiusi in microcanali. Questo lavoro ha un duplice carattere: da una parte, abbiamo studiato la dinamica di gocce sessili soggette ad oscillazioni del substrato; dall'altra, abbiamo investigato come la distribuzione spaziale della concentrazione in sospensioni batteriche, prese come sistema modello per colloidi attivi, venga alterata da un confinamento geometrico.

**Dinamica di gocce sessili.** Il primo argomento rientra nel campo dei fenomeni di bagnabilità e della microfluidica aperta, che tratta il comportamento di gocce, tipicamente nel range dei nano-/microlitri, depositate su superfici aperte. A tali scale di lunghezza, questi sistemi sono dominati dalla capiallarità a possono produrre effetti inaspettati che non vengono comunemente osservati alle scale macroscopiche a cui siamo abituati. I nostri studi sono volti al raggiungimento del controllo attivo del moto e della forma delle gocce per mezzo di vibrazioni del substrato, con applicazioni dalla Chimica alla Biologia.

In particolare, è stato considerato il moto di gocce su in substrato inclinato sottoposto ad oscillazioni armoniche verticali. Normalmente, su superfici inclinate le goccioline rimangono ferme a causa dell'isteresi dell'angolo di contatto. Quando vengono applicate oscillazioni verticali le goccioline si sbloccano e scivolano giù. Sorprendentemente, per ampiezze di oscillazioni sufficientemente grandi le goccioline si movono verso l'atro cntro la forza di gravità. Un'analisi della risposta delle gocce al variare dell'accelerazione di picco e della frequenza di oscillazione, prendendo in esame fluidi con diverse tensioni superficiali e viscosità, ha permesso il controllo del moto unidimensionale lungo il piano inclinato.

Inoltre, abbiamo studiato le morfologie interfacciali di gocce d'acqua confnate sulla faccia superiore idrofilica di post rettangolari con larghezza 0.5 mm e varie lunghezze. Per piccoli volumi, il film liquido prende la forma di un filamento omogeneo con una cross-section uniforme simile ad un segmento circolare. Per volumi più grandi, l'interfaccia acqua/aria forma un rigonfiamento centrale, che cresce con il volume. Nel caso di post pi lunghi di una lunghezza caratteristica, la transizione tra le due forme al variare del volume  discontinua e mostra la bistabilità dei due stati morfologici associata ad un fenomeno di isteresi. Applicando al post, con volume d'acqua fissato corrispondente alla bistabilità, vibrazioni verticali con determinate frequenze si pu indurre una transizione irreversibile dallo stato di filamento omogeneo a quello rigonfiato

**Particelle auto-propulse sotto confinamento geometrico.** Il secondo argomento riguarda il comportamento di fluidi attivi, cioè sospensioni di colloidi auto-propulsi che costituiscono sistemi

intrinsecamente fuori equilibrio (Materia Attiva). In particolare, in presenza di strutture geometriche, tali sistemi si comportano in modo molto differente rispetto a colloidi Browniani all'equilibrio. Abbiamo analizzato il ruolo di diversi schemi di motilità sulla distribuzione di concentrazione di sospensioni batteriche confinate tra due pareti solide. considerando *E. coli* a *P. aeruginosa* wild-tye, che si muovono secondo gli schemi *Run and Tumble* e *Run and Reverse*, rispettivamente. I profili di concentrazione sono tati ottenuti contando i batteri motili a diverse distanze dalle pareti. In accordo con studi precedenti, si osservato un accumulo di batteri motili in prossimit delle pareti. Sono state testate diverse frazioni di batteri motili e diverse distanze di separazione tra le pareti, nel range tra 100 $\mu$m e 250 $\mu$m. I profili di concentrazione risultano indipendenti dalla distanza tra le pareti e dai differenti schemi di motilit e scalano con la frazione di batteri motili. Questi risultati sono confermati da simulazioni numeriche, basate su una collezione di particelle allungate auto-propulse che intragiscono solo tramite interazioni steriche.

**Keywords primarie:** bagnabilità, microfluidica aperta, gocce, colloidi attivi, batteri.

**Keywords secondarie:** oscillazioni, moto su substrati inclinati, transizioni morfologiche, microswimmers, accumulo alla parete.

Si ringrazia la Fondazione Cassa di Risparmio di Padova e Rovigo per il supporto finanziaro a questo dottorato di ricerca nell'ambito del "Progetto Dottorati di Ricerca 2013" in collaborazione con l'Università degli Studi di Padova.

# Abstract

This PhD thesis is focused on the role of interfaces that characterize microfluidic systems, such as the free air/liquid interface of drops or the liquid/solid interface of fluids enclosed in microchannels. This work has a twofold character: on one side, we studied the dynamics of sessile drops subject to oscillations of the substrate; on the other, we investigated the spatial concentration distribution of suspensions of motile bacteria, as a model system for active collids, tuned by geometrical confinement.

**Dynamics of sessile drops.** The first topic is related to the field of wetting phenomena and open microfluidics, which deals with the behaviour of drops, typically in the nano-/microliter range, deposited on open surfaces. At such length scale, these system are dominated by capillarity and may give rise to unexpected effects, not commonly observed at the larger scale we are used to. Our studies aim to the achievement of an active control on the motion and shape of drops by means of vibration of the substrates, for chemical or biological applications.

In particular, the motion of liquid drops on an inclined substrate subject to vertical harmonic oscillations has been considered. Typically, small droplets on inclined surfaces remain pinned because of contact angle hysteresis. When vertical oscillations are applied the droplets unpin and slide down. Surprisingly, for sufficiently large oscillation amplitude the droplets move upward against gravity. The systematical investigation of the response of drops on varying peak acceleration and frequency of oscillations, for fluids with different surface tensions and viscosity, allowed the control of the unidimensional motion along the substrate.

Then, we have studied the interfacial morphologies of water drops confined on the hydrophilic top face of rectangular posts of width 0.5 mm and various length. For small volumes, the liquid film adopts the shape of a homogeneous filament with a uniform cross section close to a circular segment. For larger volumes, the water interface forms a central bulge, which grows with the volume. In the case of posts longer than a characteristic length, the transition between the two film shapes on varying the volume is discontinuous and exhibits the bistability of the two morphologic states associated with a hysteresis phenomenon. Vertically oscillating the post, with fixed water volume corresponding tho the bistability, at certain frequencies induces an irreversible transition from the filament to the bulge state.

**Self-propelled particles under geometrical confinement.** The second topic deals with the behaviour of active fluids, i.e. self-propelled colloid suspensions which are intrinsically out of equilibrium systems (Active Matter). In particular, in the presence of geometrical structures, such systems behave in a very different way with respect to equilibrium Browinan colloids. We have analyzed the

role of different swimming patterns on the concentration distribution of bacterial suspensions confined between two flat walls, by considering wild-type *E. coli* and *P. aeruginosa*, which perform *Run and Tumble* and *Run and Reverse* patterns, respectively. The concentration profiles have been obtained by counting motile bacteria at different distances from the bottom wall. In agreement with previous studies, an accumulation of motile bacteria close to the walls was observed. Different fraction of motile bacteria and different wall separations, ranging from 100 $\mu$m to 250 $\mu$m, have been tested. The concentration profiles resulted to be independent on the walls separation and on the different kind of motility and to scale with the motile fraction. These results are confirmed by numerical simulations, based on a collection of self-propelled rod-like particles interacting only through steric interactions.

**Primary keywords:** Wetting, open microfluidics, drops, active colloids, bacteria

**Secondary keywords:** Oscillations, motion on inclined substrates, morphological transitions, microswimmers, wall accumulation

The bank foundation "Fondazione Cassa di Risparmio di Padova e Rovigo" is gratefully acknowledged for its financial support to this PhD in the frame of the PhD Program 2013 "Progetto Dottorati di Ricerca 2013" in partnership with the University of Padova (Italy).

# Contents

# List of Figures

# Introduction

The behaviour of a system in the presence of interfaces can be significantly different from the bulk behaviour. In microfluidic systems, consisting in small amount of fluids ($\sim$ nL – $\mu$L) confined at submillimetric scale, phenomena related to surfaces and interfaces becomes largely dominant with respect to bulk effects, as suggested by the small length limit of the surface to volume ratio. For instance, inertial and gravitational effects are negligible with respect to surface tension and viscosity. As a consequence of this unusual forces balance, the behaviour of such systems may result surprisingly different from what we are used to in our macroscopic scale experience.

Think of the capillary adhesion exerted by a thin layer of water between two glass slides. The force that keeps the two solid surfaces together is remarkably large, of the order of 10 N if we consider a drop of 1 $\mu$L squeezed in a 5 $\mu$m thick layer. Tree frogs exploit capillary adhesion to climb smooth surfaces by secreting a wetting watery liquid from their large toe pads (see figure 1). Another situation in which the presence of confining surfaces alters the properties of the system is represented by colloidal suspensions, in particular in the case of self-propelled particles. As we will detail later, geometrical coninement may modifie both their concentration and their motion near interfaces. We just mentioned a few examples: the interaction between surfaces and liquid at the micrometric scale are ubiquitous, from technological applications (e.g. water-repellency, anti-fogging, painting, aerosols) to biological aspects (e.g. cell membranes, soil microbiology, blood transport, filtering).

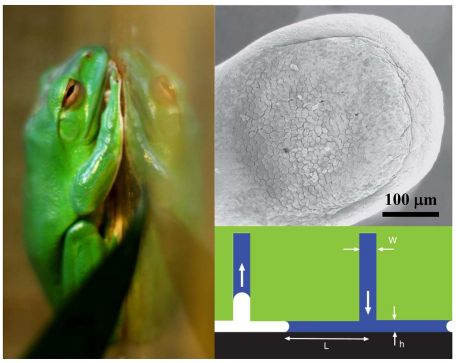


**Figure 1 :** Tree frogs exploit capillary adhesion to climb smooth surfaces [1, 2].

**Wetting phenomena and open microfluidics.** Capillary phenomena are of great impact in many aspects of everyday life or in many practical processes in which liquids are in contact with solids [3–5]. Let's think of the spreading of paint or ink, the deposition of pesticides on plants, the realization of water repellent surfaces or superlyophobic textiles, the water penetration into soil or porous materials, etc. In all these situations, it is of paramount importance to take into account capillary forces that are usually neglected at the macroscopic scale, where, for instance, gravity is dominant. To understand the relevance of capillarity over gravity in a micrometric system, we can consider a water drop with 100 $\mu$m size: the pressure jump across the air/water interface, related to its curvature and to surface tension, (the Laplace pressure, defined in section 1.1) is $\sim 10^3$ Pa while the hydrostatic pressure is $\sim 10^{-3}$ Pa.

The fundamental knowledge of wetting and capillarity is applied in the field of *open microfluidics* [6,7], which deals with the behaviour and the manipulation of small liquid volumes ($\sim$ nL – $\mu$L) on open surfaces, characterized by free liquid/vapour or liquid/liquid interfaces. With respect to traditional microfluidics [8,9], which handles single- or multi-phase laminar flows in closed microchannels with dimensions of tens to hundreds of micrometers, open microfluidics is emerging as a valuable alternative. It allows free access to the drops on the whole substrate and it avoids several drowbacks, e.g. microchannels are subject to clogging, air bubbles can remain trapped, driving the flow becomes more difficult as the channel cross-section becomes smaller and the fabrication is more challenging [10]. The final target of open microfluidics is the full control of drops or liquid films on the substrate, including formation, volume [11], shape [12–15], merging and splitting [16] and motion [17–19], offering important technological tools for a wide range of applications in chemistry, biology and pharmaceuticals, similary to what happens for close microfluidics [8,20–22]. Basically, there are two main strategies to achieve the control of drops: passive methods, based on chemical or topographical patterning of the substrates, or active methods, which employ external field, e.g. electric or magnetic fields.

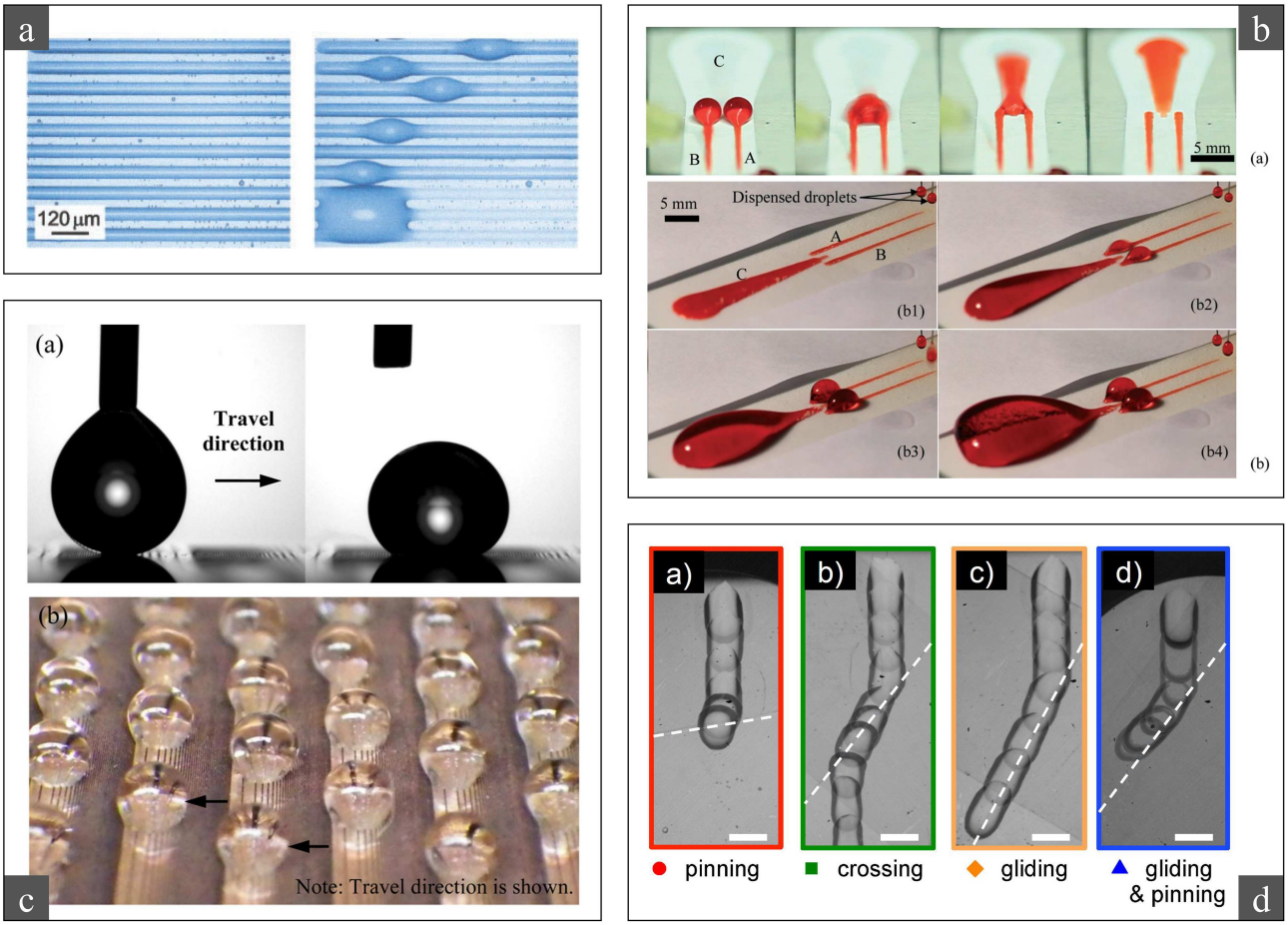


**Figure 2 :** Examples of passive methods to control drops: (a) interfacial morphologies corresponding to different volumes of water condensed on hydrophilic striped domains [12]; (b) drops deposited on narrow end of wedge-shaped superhydrophilic tracks are transported toward the wider end [16]; (c) droplets moving on a surface with a wettability gradient obtained by modulating the size of microstructure patterns [23]; (d) control of the trajectory of a drop sliding down an inclined surface presenting a linear chemical boundary between hydrophilic and hydrophobic regions [24].

Passive methods rely on wettability patterns and structurations of the substrate, such as suitably shaped hydrophilic domains on hydrophobic surfaces or grooved substrate. Several studies, both experimental and theoretical, demonstrated the possibility of controlling the liquid interface morphology by such methods [12, 13, 15]: water confined on striped hydrophilic domains or on linear grooves displays different interfacial shapes and morphological transitions between them depending on the liquid volume and the specific geometry (see figure 2c). Ghosh *et al.* [16] exploited wettability patterns to realize tracks that are capable to transport drops. Such tracks consist in wedge-shaped superhydrophilic domains on superhydrophobic background. The liquid drops, with size bigger then the average width of the track, deposited on the narrow end of the wedge are transported toward the wider end by Laplace pressure unbalance. The wedge-shaped tracks are the building blocks for a variety of designs with tasks from splitting and merging to meterd dispensing (see figure 2a). Anoher way to induce a directional motion of drops is substrate wettability gradient, which can be produced, for instance, by modulating the size of microstructure patterns [23, 25] (see figure 2b). Chemical patterns can be also employed to tune and direct the motion of a drop sliding down an inclined surface under gravitational pull [24, 26] (see figure 2d).

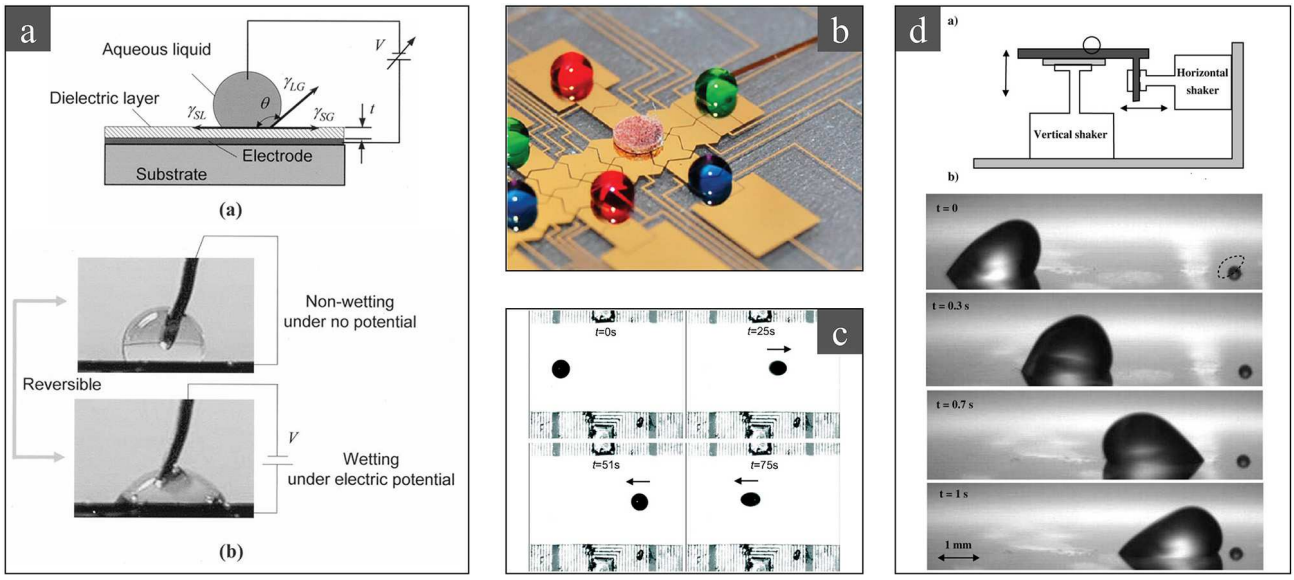


**Figure 3 :** Examples of active methods to control drops: (a) principle of electrowetting [27]; (b) dried blood spot analysis by digital microfluidics [28]; (c) manipulation of ferrofluid droplets using planar electromagnetic coils [29]; (d) motion of a drop lying on a substrate simultaneously subject to horizontal and vertical harmonic oscillations [30].

On the other side, active methods are based on the application of external fields. One of the most widespread technique is electrowetting [31, 32], which allows to modify in a controlled way the wettability of a surface by applying an electric potential difference between a polar liquid and the substrate (see figure 3a). If the substrate is paved with a pattern of electrodes, it is possible to change locally the wettability in such a way to induce the motion of the drop in the desired direction. This technique is at the base of the so-called digital microfluidics [27] that finds wide variety of applications in chemistry, biology and medicine [28, 33–36] (see figure 3b). Conversely, the use of magnetic fields is reserved to ferrofluids, i.e. colloidal suspension of ferromagnetic nanoparticles stabilized by surfactants,

employing planar microcoils in a similar fashion with respect to electrowetting [29, 37] (see figure 3c). We can also mention the application of surface acoustic waves (SAW), i.e. nanometer amplitude Rayleigh waves with frequency of order of MHz propagating on the surface of a piezoelectric substrate, to drive and actuate sessile droplets thanks to the propagation of the waves into the liquid medium resulting in fluid recirculation [17]. A different way to exploit vibrations is to apply rigid oscillation to the whole substrate with frequency from tens to hundreds Hz. If the substrate is subject to just vertical or horizontal harmonic oscillations the average drop displacement over a cycle is null because of the symmetry of the system. In order to achieve a net displacement, such symmetry has to be broken, for instance, by applying oscillations with an asymmetric waveform [38], by combining vertical and horizontal harmonic vibrations [30] (see figure 3d) or by vertically oscillating an inclined plane [39]. In this way, the asymmetric deformation of the free liquid interface, arising from the inertial coupling with the substrate oscillations, can induce a net motion of the drop that can be controlled by tuning oscillation frequency and amplitude.

Obviously, passive and active methods can be successfully combined together: Klingner and Mugele [14] applied electrowetting to induce morphological transitions of water microstructures on a pattern of hydrophilic stripes on hydrophobic background, Daniel and Choudhury [40] induced the motion of microliter drops by vibrating a substrate with a wettability gradient, just to cite a couple of examples.

**Active colloidal suspensions.** The field of *active matter* deals with a great variety of systems, spanning from macroscopic down to microscopic scales, with the common feature of consisting in large collections of self-propelled units. This units, also called active particles, have the capability to convert free energy from the environment into work, in order to move, grow, replicate, etc. Therefore, such systems are intrinsically out of thermodynamic equilibrium [41]. In some cases, the individual units may interact both directly and through perturbations propagating via the medium they are surrounded. As consequence of these interactions, collective behaviours and self-organization may emerge. Some examples are given by flocks of birds, schools of fishes and swarms of insects, at the macroscopic scale, motile bacteria, cell cytoskeleton and cytoplasma and molecular motors, at the micrometric scale. The latter category is also referred as *soft active matter* [42].

Among such a huge diversity of systems, we focus on *active suspensions*, i.e. self-propelled particles with colloidal size (from $\sim 1$ nm to $\sim 1$ $\mu$m) dispersed in a fluid medium. Their dynamics is characterized by both low Reynolds number hydrodynamics [43,44] and thermal fluctuations [45]. The most paradigmatic case of active suspension is represented by swimming microorganisms, in particular bacteria [46].

The study of microswimmers can be carried out on different levels. The first one is from the molecular and biochemical point of view, leading to the physiology of propelling mechanisms (e.g. flagella structure, motor proteins, etc.) [47]. A second level involves the analysis of the low Reynolds number hydrodynamics ruling the motion, the interactions and the swimming strategies of microorganisms in the fluid [43, 48]. Finally, a third level takes into account the global statistical properties of the motion, neglecting the particular details of the microorganisms and the hydrodynamic interactions [49]. Basically, in our study we focus on this third level.

Most part of swimming microorganisms live in geometrically confined environment at the micro-

metric scales. Besides fundamental research, this topic is of particular interest given the application from soil microbiology, water filtration, to bacterial pathogenesis. In this context, the role of surface and interfaces is of paramount importance. Many experiments have demonstrated that the interaction of microswimmers with surfaces and geometrical structures may alter both their spatial distribution and their motility patterns.

For instance, swimming bacteria are observed to swim in circular trajectories next to either a solid surface [50,51] or a liquid/air interface [52] with opposite directions as a consequence of hydrodynamic interaction with the interface (see figure 4).

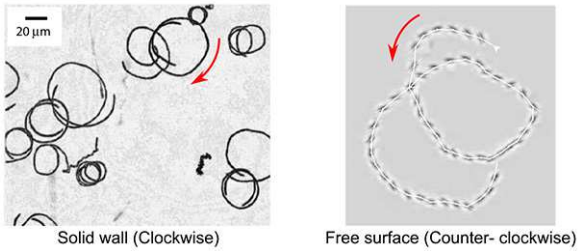


**Figure 4 :** Clockwise circular motion of bacteria close to a solid wall (left panel) [50] and counterclockwise circular motion close to a free surface (right panel) [52].

Another impressive example is given by the rectification phenomenon occurring when microswimmers display trajectories which break time-reversibility in the presence of structures with asymmetric geometries [45]. This is the case of motile bacteria, such as *E. coli*, in the presence of a wall made of funnel-shaped openings: bacteria do not uniformly distribute on both sides but they concentrate on the narrow opening side of the wall because of the asymmetrical shape of the surfaces and the hydrodynamic tendency to swim parallel to walls (see figure 5a-c) [53]. Furthermore, a similar effect consists in the rotation of an asymmetric micrometric gear due to the interaction with motile bacteria in suspension (see figure 5d) [54].

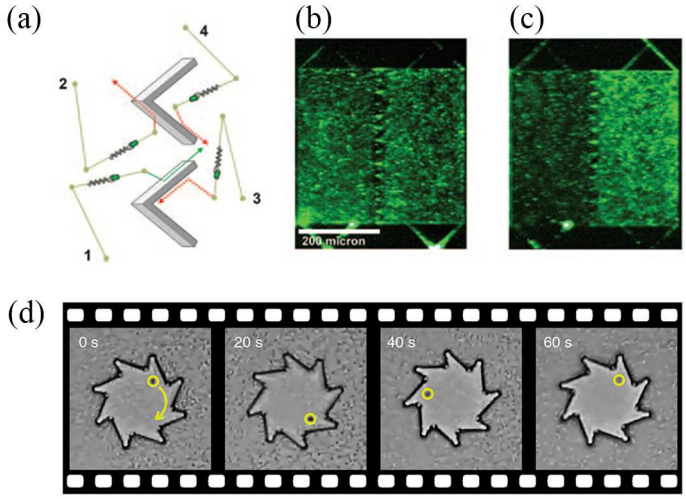


**Figure 5 :** Rectification effects: (a-c) accumulation of motile *E. coli* on the narrow opening side of the funnel-shaped wall [53]; rotation of an asymmetric gear due to the interaction with motile bacteria in suspension [54].

Finally, we mention the phenomenon we describe in chapter 5, i.e. the accumulation of motile bacteria close to a solid surface [55–60]. The origin of this aggregation is still under debate, in particular two mechanisms have been proposed: on one side a dipolar hydrodynamic attractive interaction between the microswimmer and the wall [56, 60], on the other a combination of self-propulsion, steric collisions with the wall and rotational diffusion [57, 58].

**This thesis.** Here we report experimental works concerning the role played by interfaces in microfluidic systems. Firstly, we have focused on capillary phenomena ruling the dynamics of small drops in contact with solid surfaces, related to the three interfaces between solid, liquid and vapour phases; then, we have taken into account the influence of interfaces on the physics of active colloidal suspensions, i.e. out of equilibrium particles that can propel themselves by extracting energy from their environment, that displays several dissimilarities from merely Brownian colloidal suspensions.

The manuscript is organized as follows:

- Part I: Oscillating sessile droplets
  - Chapter 1 introduces the fundamental concepts about wetting and capillary phenomena;
  - Chapter 2 describes the dynamics of drops on an inclined surface subject to vertical harmonic oscillations;
  - Chapter 3 shows the morphological transitions of water drops confined on rectangular posts induced by either volume variations or vibrations of the substrate;
- Part II: Confined bacterial suspensions
  - Chapter 4 gives some useful basic concepts for the understanding of the dynamics and the statistics of swimming microorganisms;
  - Chapter 5 illustrates the effects of a slit-like confinement on bacteria suspensions with different swimming patterns;
- Conclusions summarize the main results of this work.

# Part I

# Oscillating Sessile Droplets

# Chapter 1

# Fundamentals of Liquid Drops on Solid Substrates

In this chapter we present fundamental concepts about wetting and capillary phenomena ruling the behaviour of drops and liquid films on solid substrates. First of all, we introduce the concepts of surface tension, in section 1.1, and contact angle, characterizing the wettability of a surface, in section 1.2. In section 1.3 we describe how gravity affects the shape of sessile drop depending on its size. Sections 1.4 and 1.5 illustrate the dynamics of contact angle of drops on real surface in the presence of the contact angle hysteresis. In particular, section 1.6 analyzes the contact line pinning on macroscopic linear obstacles of chemical or physical nature. Section 1.7 describes the variety of interfacial shapes and the morphological transitions between them when solid substrates exhibit wettability patterns or topographical structurations and, finally, in section 1.8 we report the behaviour of sessile drops on oscillating surfaces.

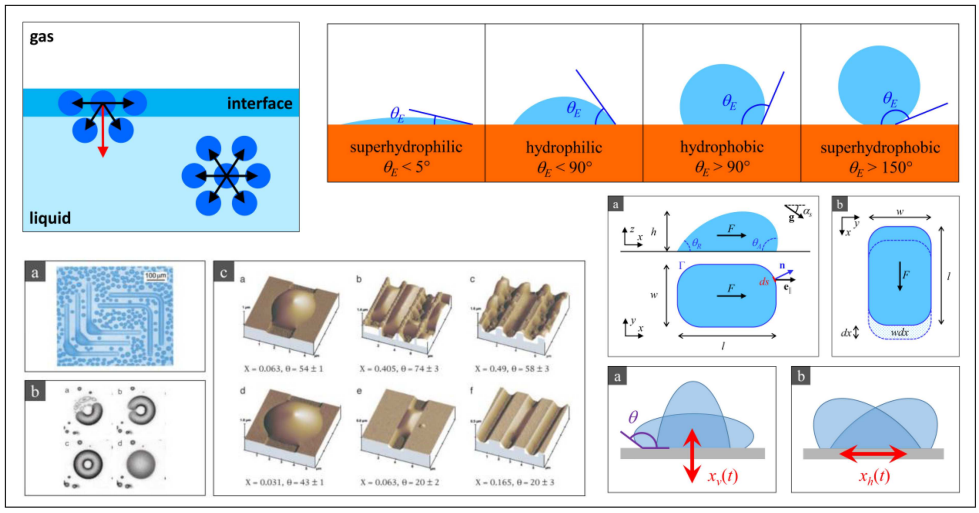

## § 1.1. Surface tension

A liquid interface, between a liquid and a gas phase or two liquid immiscible phases, behaves like an elastic stretched membrane. Its area tends to the minimum value allowed by the boundary conditions, e.g. the liquid volume or solid boundaries. The physical origin dwells at the molecular scale. Each molecule is subject to cohesive interactions (e.g. Van der Waals type, hydrogen bonds, etc.) exerted by the surrounding molecules. A molecule in the bulk is isotropically surrounded by neighbours yielding a resulting null force. Conversely, a molecule at the interface interacts anisotropically with less neighbours and it is subject to a net force directed at the bulk (see figure 1.1a). The number of unbalanced interactions, and the related energy, grows with the surface area, so that the system tries to assume the shape with the smallest possible liquid interface. The surface tension represents this energy per unit area. In order to evaluate the surface tension for some fluids, we can consider the "Moses' experiment" [61] (see figure 1.1b): if $U$ is the binding energy between two molecues and $a$ is the molecule's size, the energy $E$ required to open a fluid bulk and create two interfaces $\Sigma$ is equal to twice the surface energy $E_s$ of one interface and it is given by $E = 2E_s \approx (\Sigma/a^2)U$, where $\Sigma/a^2$ is an esteem of the number of molecules at the interface and the number of broken bonds. Consequently, the surface tension can be evaluate as

$$\sigma = \frac{E_s}{\Sigma} \approx \frac{U}{2a^2}. \tag{1.1}$$

For non-polar liquids, such as most oils, the interactions are Van der Waals type and the binding energy is of the order of the thermal energy, $U \approx k_B T$ ($k_B$ is the Boltzmann constant and $T$ is the temperature in K), which at 25° C is 25 meV. The corresponding surface tension for a liquid/gas interface is $\sigma \approx 20$ mJ/m$^2$. Water molecules interact via hydrogen bonds yielding an higher surface tension $\sigma \approx 72$ mJ/m$^2$. For mercury bonds are even stronger: $U \approx 1$ eV and $\sigma \approx 500$ mJ/m$^2$ [3].

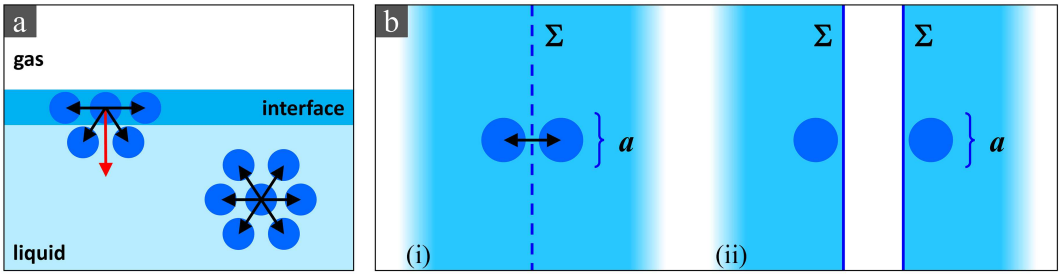


**Figure 1.1 :** (a) Microscopic origin of surface tension: molecules at the liquid/gas interface interact with less neighbours than molecules in the bulk. (b) "Moses' experiment": a fluid bulk is divided in two parts and two interfaces with area $\Sigma$ are created with an energy increase for the system.

We saw at microscopic scale that the creation of a surface is energetically costly. At macroscopic scale, we define the surface tension $\sigma$ as the work $W$ required to increase the surface area $A$ by one unit, so that:

$$\delta W = \sigma \, dA. \tag{1.2}$$

From the thermodynamic point of view, surface tension can be expressed in term of free energy $\mathcal{F}$

as:

$$\sigma = \left[\frac{\partial \mathcal{F}}{\partial A}\right]_{T,V,n} \tag{1.3}$$

where $V$ is the total volume and $n$ the number of molecules.

As written above, surface tension is an energy per unit area but it can also be thought as a force per unit length: if we consider an ideal line cutting the interface, both half-planes exert a force $dF_\perp$ perpendicularly on the portion of line $dl$ with opposite directions (see figure 1.2a). If we imagine to apply a force $dF$ per length $dl$ to open this cut by a width $dx$ with an area increase per length $dl$ of $dxdl$ (see figure 1.2b), the corresponding required work is $\delta W = dFdx = \sigma dxdl$, so that we have:

$$dF = \sigma\, dl. \tag{1.4}$$

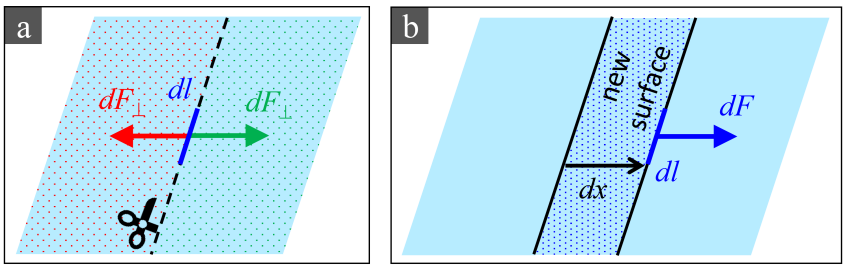


**Figure 1.2 :** Surface tension as a force for unit length. (a) An ideal line cuts the surface in two half-plane, both of which exert perpendicular forces on the line balancing each other. (b) An external force moves one side of the cut increasing the surface area.

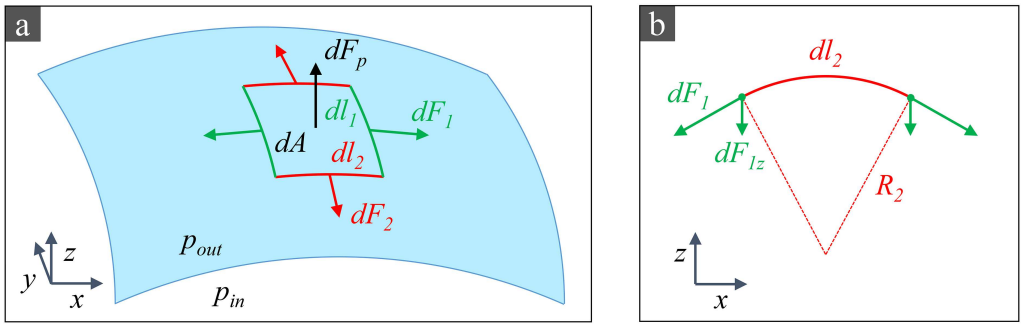


**Figure 1.3 :** (a) Forces acting on an elementary surface $dA = dl_1 dl_2$ of a curved interface with curvature radii $R_1$ and $R_2$: $dF_p$ is the force due to Laplace pressure, $dF_1$ and $dF_2$ are the capillary forces acting on the boundaries of the elementary surface. (b) Cross-section of the elementary surface in the $(x, z)$ plane.

In the case of a curved interface, surface tension forces tend to shrink the surface in order to reduce the associated energy, causing a pressure jump $\Delta p = p_{in} - p_{out}$ between inside and outside. This pressure jump is referred as *Laplace pressure*. At equilibrium Laplace pressure force and surface tension forces are in balance. With regard to figure 1.3, we can evaluate the equilibrium Laplace pressure across a curved interface with curvature radii $R_1$ and $R_2$. The forces acting on the elementary surface $dA = dl_1 dl_2$ are $dF_p = \Delta p\ dA$, due to Laplace pressue, $dF_1 = \sigma dl_1$ and $dF_2 = \sigma dl_2$ on the boundaries, due to surface tension. The balance along the $z$ axis is given by $dF_p = 2dF_{1z} + 2dF_{2z}$ and consequently:

$$\Delta p \, dl_1 dl_2 = \sigma dl_1 \frac{dl_2}{R_2} + \sigma dl_2 \frac{dl_1}{R_1}. \tag{1.5}$$

Summarizing, the *Laplace law* states that the pressure increase $\Delta p$ across a curved interface is given by the product of the surface tension $\sigma$ and the total curvature $C = (R_1^{-1} + R_2^{-1})$:

$$\Delta p = \sigma \left( \frac{1}{R_1} + \frac{1}{R_2} \right) = \sigma C. \tag{1.6}$$

If hydrostatic pressure is negligible, $\Delta p$ is constant as well as the total curvature $C$.

## § 1.2. Drops on ideal flat surfaces: the contact angle

In section 1.1 we dealt with liquid/gas or liquid/liquid interfaces. In the case of a liquid drop in contact with a solid substrate we are in the presence of three different phases: the solid, the liquid and the surrounding medium (let say gas but it can be an immiscible liquid). The intersection of the three interfaces between each couple of phases is called *triple line* or *contact line* and the area comprised is the *contact area*. If the substrate has an ideally flat homogeneous surface the contact area is circular. The angle $\theta$ between the liquid/gas and the solid/liquid interfaces (see figure 1.4a) is the *contact angle*. At equilibrium, on an ideal flat solid surface the contact angle $\theta_E$ is univocally determined by the *Young's law* that represents the mechanical balance of the three interfacial tensions considered as forces per unit length on the contact line, as sketched in figure 1.4b:

$$\sigma \cos\theta_E = \sigma_{SG} - \sigma_{SL}, \tag{1.7}$$

where $\sigma_{SL}$, $\sigma_{SG}$ and $\sigma$ are the solid/liquid, solid/gas and liquid/gas interfacial tensions, respectively. We can notice that the component of the capillary force normal to the solid surface is not zero. This force has to be balanced by a vincular reaction provided by the substrate. In the case of soft solids, the surface of the substrate can be deformed at the contact line [62, 63].

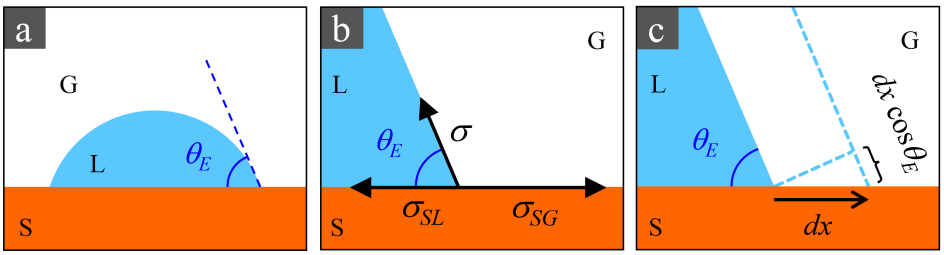


**Figure 1.4 :** (a) Liquid drop on an ideal flat solid surface. (b) Determination of $\theta_E$ via mechanical balance of surface tensions. (c) Determination of $\theta_E$ via energy minimization.

An equivalent way to derive the Young's law is from energy minimization. The work per unit length done for a displacement $dx$ of the contact line along the solid surface (see figure 1.4c) can be written as:

$$\delta W = \sigma_{SL} dx + \sigma dx \cos\theta_E - \sigma_{SG} dx. \tag{1.8}$$

At equilibrium the work $\delta W$ is zero, leading to Young's equation 1.7. In contrast to surface tensions, the contact angle can be directly and quite silmply measured by optical imaging (see section **??**). For this reason the wettability of a surface is defined in term of contact angle for a water drop [64] (see figure 1.5):

- if $\theta_E < 5°$ the surface is superhydrophilic;
- if $\theta_E < 90°$ the surface is hydrophilic;
- if $\theta_E > 90°$ the surface is hydrophobic;
- if $\theta_E > 150°$ the surface is superhydrophobic.

The *total wetting* regime is the case in which water completely spreads on the substrate forming a thin film and corresponds to the condition $\sigma \leq \sigma_{SG} - \sigma_{SL}$.

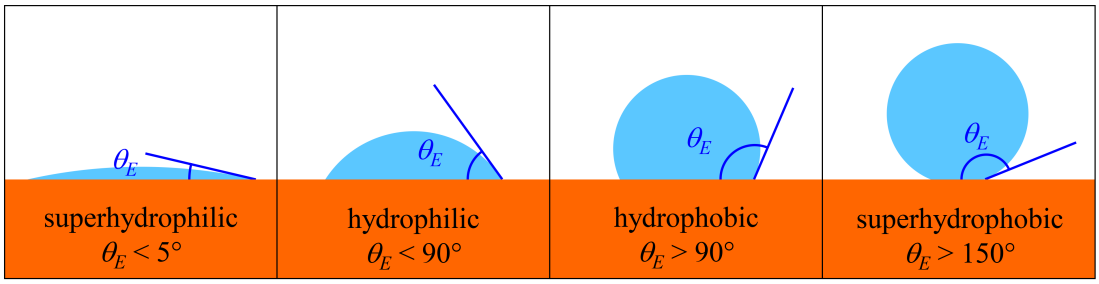


**Figure 1.5 :** Wettability of a solid surface defined by the contact angle of a sessile water drop [64].

Surface roughness can enhance the the natural wettability of the solid. With increasing roughness an hydrophobic (hydrophilic) surface can become superhydrophobic (superhydrophilic). On smooth surfaces the maximum contact angle observed is about 120°, so we cannot have superhydrophobicity [65].

In general, the term lyophobic (lyophilic) is used for liquids different from water, instead of hydrophobic (hydrophilic).

## § 1.3. Drops and gravity

If we neglect gravity, Laplace pressure is the only contribution to the pressure inside a sessile droplet, yielding a constant curvature of the liquid/gas interface, and, in the absence of constraints, the equilibrium shape is a spherical cap. In every day experience this is what we observe for small droplets, in which the capillary contribution is dominant. As drop size increases, the gravitational contribution gains significance and the drop tends to flatten. The length scale characterizing the transition between these two regimes is the *capillary length* $\kappa^{-1}$. It represents the drop size $R$ for which the Laplace pressure and the hydrostatic pressure are of the same order ($\sigma/R \approx \rho g R$):

$$\kappa^{-1} = \sqrt{\frac{\sigma}{\rho g}} \tag{1.9}$$

where $\rho$ is the liquid density and $g$ is the gravitational acceleration. For instance, the capillary length for water is about 2.7 mm and, typically, also for other liquids it is of the order of few millimeters. Droplets with size $R << \kappa^{-1}$ are spherical caps. On the other hand, large drops with $R >> \kappa^{-1}$ are flattened by gravity and their height is of the order of the capillary length [3, 5]. Moreover, the equilibrium contact angle, being a local quantity, does not depend on drop size (see figure 1.6).

The *Bond number* $Bo$ is a dimensionless parameter with a physical meaning similar to that of the capillary length. It is the ratio between the gravitational and the capillary contributions, represented by the hydrostatic pressure ($\rho g R$) and the Laplace pressure ($\sigma/R$), respectively:

$$Bo = \frac{gravity}{capillarity} = \frac{\rho g R^2}{\sigma}. \tag{1.10}$$

$Bo \ll 1$ corresponds to the capillary regime ($R \ll \kappa^{-1}$), while $Bo \gg 1$ corresponds to the regime in which gravity is dominant ($R \gg \kappa^{-1}$).

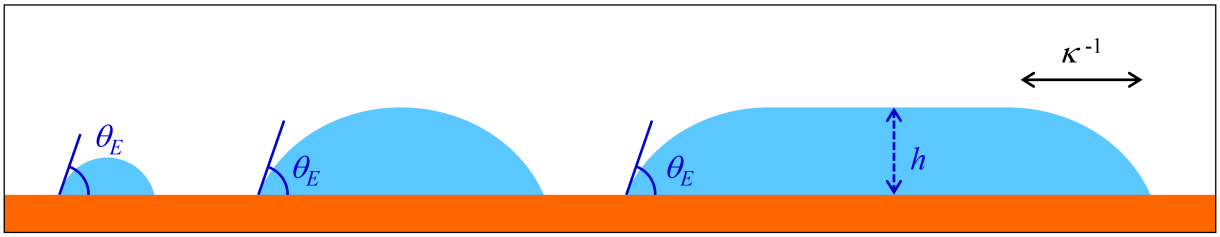


**Figure 1.6 :** Sketch of sessile drops with increasing size. Below the capillary length $\kappa^{-1}$ the drop is a spherical cap; above $\kappa^{-1}$ the drop has the shape of a pancake with height $h \sim \kappa^{-1}$. No matter the size, the contact angle is the same.

## § 1.4. Drops on real surfaces: the contact angle hysteresis

We saw that on an ideal smooth homogeneous plane the contact angle is univocally fixed by the surface tensions of the three interfaces, as predicted by Young's law 1.7. However, no surface is ideally perfect; real surfaces are characterized at microscopic scale by

- chemical defects (local variations in wettability),
- physical defects (surface morphological irregularities).

As a consequence, the contact line can be pinned by these defects and the static contact angle is no more the univocally determined $\theta_E$ of equation 1.7 but it can assume a range of values (see figure 1.7).

Suppose we deposit a sessile drop on a real surface and we first inflate and then deflate it (see figure 1.8a). We can observe that, as the volume grows, the contact angle $\theta$ increases while the contact line does not move. Eventually, the contact line unpins when $\theta$ reaches a threshold value $\theta_A$ called *advancing contac angle*. Similarly, as the volume diminishes, the contact angle $\theta$ decreases and the contact line is pinned as far as the $\theta$ reaches another threshold value $\theta_R$ called *receding contact angle*. At that point the contact line starts to displace. The typical time evolution of contact angle $\theta$ and contact line radius $r$ during inflation and deflation of the drop is reported in figure 1.8b [66]. Consequently,

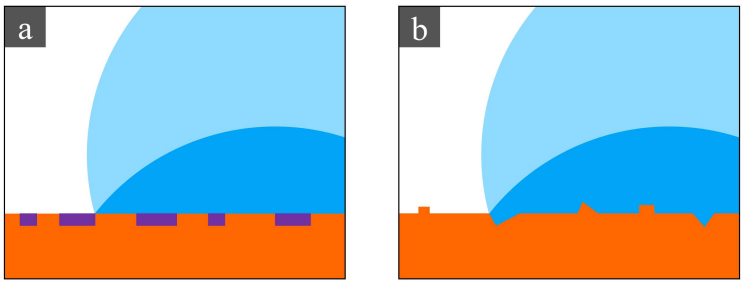


**Figure 1.7 :** Cartoons of real surfaces where the contact angle can assume a range of values because of the pinning of the contact line on: (a) chemical defects; (b) physical defects.

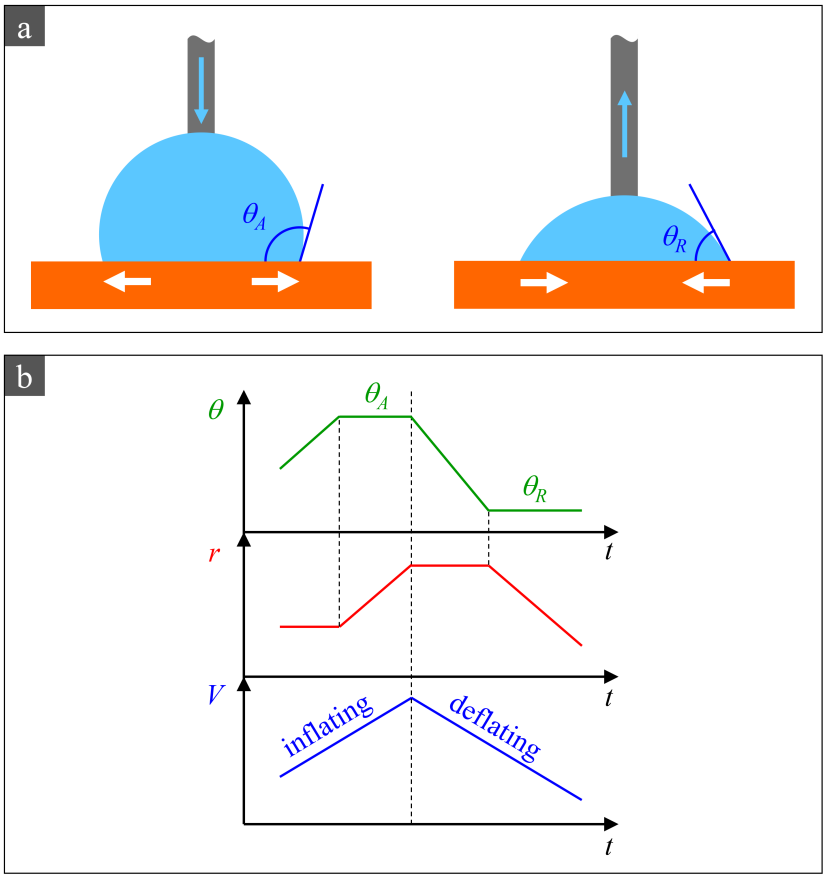


**Figure 1.8 :** (a) Operative definition of advancing ($\theta_A$) and receding ($\theta_R$) contact angles by inflating (left) and deflating (right) a sessile drop. (b) Typical time evolution of contact angle $\theta$ and contact line radius $r$ during inflation and deflation of drop volume $V$.

the contact angle can assume each value comprised between the receding and the advancing contact angles: $\theta_R \leq \theta \leq \theta_A$. To make it simple, we can say that the larger contact angle of the advancing front is due to a "slowing down" by local defects, whereas the smaller contact angle of the receding front is due to a "pulling back" by the same defects. The *contact angle hysteresis*, defined as the difference between advancing and receding contact angles $\Delta\theta = \theta_A - \theta_R$, gives a measure of how the contact line is pinned by defects on the surface*.

In order to characterize the wetting properties of a real surface, we need both the equilibrium contact angle $\theta_E$ and the contact angle hysteresis $\Delta\theta$. For instance, due to specific morphological patterns, we can find superhydrophobic surfaces with the same equilibrium contact angle ($\theta_E > 150°$) where water drops behave in opposite manners: in the case of the *lotus leaf effect* [67] the surface shows an extremely small hysteresis and water drops immediately roll off; on the other hand, in the case of the *rose petal effect* [68, 69] the surface shows a large hysteresis and drops remain stuck. Theoretical predictions of advancing and receding contac angles are very difficult, because hysteresis strongly depends on many parameters describing the details of the defects.

## § 1.5. Drops on inclined surfaces

A drop on an ideal tilted surface would slide down for any inclination angle $\alpha$ maintaining the equilibrium shape. Conversely, on an inclined real surface the drop profile looses its symmetry: the front (i.e. lower part) assumes a blunt shape and the rear (i.e. upper part) becomes thinner [70]. The contact angle is no more the same all along the contact line but it ranges from a minimum value $\theta_{up}$ at the upper point to a maximum value $\theta_{down}$ at the lower point (see figure 1.9a). As the inclination increases, $\theta_{up}$ decreases and $\theta_{down}$ grows. Because of contact angle hysteresis, the drop remains pinned on the surface as far as $\theta_{up} > \theta_R$ and $\theta_{down} < \theta_A$. The force opposing to the gravitational pull arises from a Laplace pressure difference due to the different curvatures at the two extremities of the drop. The inclination angle $\alpha_s$ at which the advancing and receding contact angles are reached and the drop starts sliding down is referred as the sliding angle (see figure 1.9b). The sliding angle can be calculated from the mechanical balance between the capillary forces, acting all along the contact line, and the component of gravity along the surface [71]:

$$\rho V g \sin\alpha_s = \sigma \oint_\Gamma \mathbf{e}_\parallel \cdot \mathbf{n} \cos\theta ds \tag{1.11}$$

where $V$ is the drop volume, $\Gamma$ is the contact line parametrized by the arc-length $s$, $\mathbf{e}_\parallel$ is the unit vector in the downhill direction and the unit vector $\mathbf{n}$ is the normal to the contact line in the plane of the substrate (see figure 1.10a).

If we assume, for simplicity, a drop with an almost rectangular contact area with width $w$, we can calculate the work $\delta W$ related to a displacement $dx$ downhill (see figure 1.10b) [72]. The work made to dewet a surface of area $wdx$ with contact angle $\theta_R$ and to wet the same amount of surface with contact angle $\theta_A$ is:

*Some author define the contact angle hysteresis with the cosine of advancing and receding contact angle: $\Delta\theta = \cos\theta_R - \cos\theta_A$. This definition can be more convenient to express capillary forces on the contact line as in equation 1.14

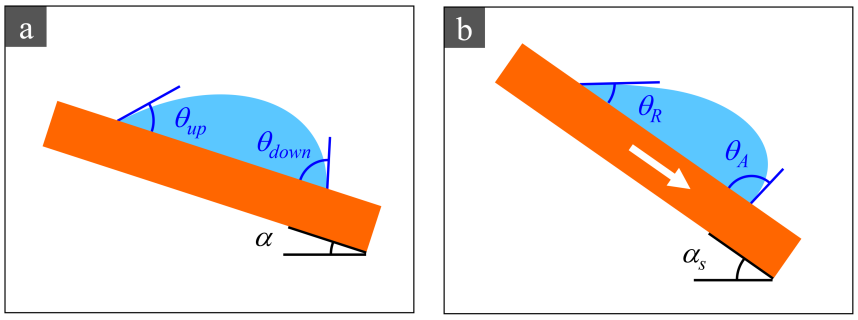


**Figure 1.9 :** A drop on a tilted surface has an asymmetric shape because of gravity: the upper contact angle $\theta_{up}$ is smaller than the lower contact angle $\theta_{down}$. (a) For small inclination angle $\alpha$, the deformation of the drop profile is not enough to overcome hysteresis. (b) For large enough $\alpha$, the upper and the lower contact angles reach the receding and the advancing contact angles, respectively, and the drop slides down.

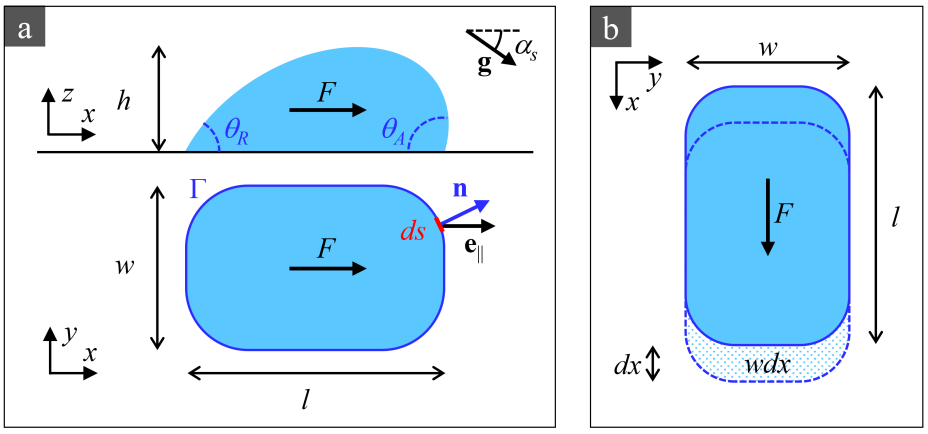


**Figure 1.10 :** (a) Side profile (top) and contour $\Gamma$ of the contact line (bottom) of a drop sliding down a plane with inclination $\alpha_s$ under the action of the gravitational pull $F = \rho V g \sin\alpha_s$. The $x$ axis represents the direction of motion. The total capillary force acting on the contact line can be calculated as the integral along $\Gamma$ of the force $\sigma ds\mathbf{n}$ on the element $ds$ [71]. (b) Displacement $dx$ down the inclined plane of a drop with almost rectangular contact line with width $w$. The correspondent work is $\delta W = wdx$.

$$\delta W = \sigma w dx \cos\theta_R - \sigma w dx \cos\theta_A. \tag{1.12}$$

Since it corresponds to the work made by the gravitational force $\delta W = \rho V g \sin\alpha_s dx$, we obtain:

$$\rho V g \sin\alpha_s = w\sigma(\cos\theta_R - \cos\theta_A). \tag{1.13}$$

In general, for drops of different shapes we can modify this equation as:

$$\rho V g \sin\alpha_s = kR\sigma(\cos\theta_R - \cos\theta_A). \tag{1.14}$$

where $R$ is the drop size, $V$ is its volume and $k$ is a non-dimensional parameter taking in accont the geometry of the contact line [73].

The sliding motion of the drop on an inclined plane is the result of the action of three forces [74] (see figure 1.11):

- the component of gravity parallel to the plane $\sim \rho U g \sin\alpha$;
- the viscous drag on the surface $\sim -\eta U V^{-1/3}$;
- the capillary force $\sim -\sigma V^{-1/3}\Delta_\theta$

where $\alpha$ is the plane inclination, $g$ is the gravitational acceleration, $\rho$ and $\eta$ are the density and the viscosity of the liquid, respectively, $V$ is the volume, $U$ is the sliding velocity and $\Delta_\theta$ is a dimensionless parameter depending on the contact angle distribution along the contact line and on its shape. After a trasient phase, the forces balance because of dissipation and the drop slides down with constant velocity and almost constant shape in a steady state [75–77]. The force balance implies a linear scaling law relating velocity $U$ and the sine of inclination angle $\alpha$ [74]:

$$Ca \approx Bo_\alpha - Bo_c \tag{1.15}$$

where

- $Ca = \dfrac{viscosity}{capillarity} = \dfrac{\eta U}{\sigma}$ is the *capillary number*;
- $Bo_\alpha = Bo \sin\alpha = \dfrac{\rho g \sin\alpha V^{2/3}}{\sigma}$ is the effective Bond number based on the component of gravity on the plane $g\sin\alpha$;
- $Bo_c$ is a constant depending on the contact angle hysteresis.

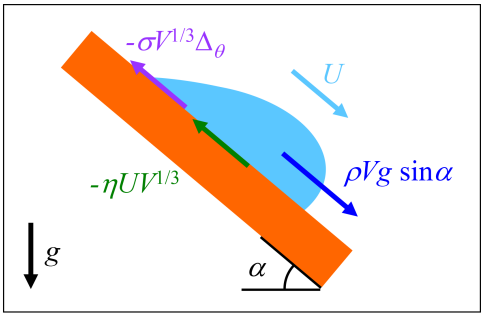


**Figure 1.11 :** Sketch of a drop sliding down an tilted surface with inclination $\alpha \geq \alpha_s$. The constant sliding velocity $U$ is the result of the balance between the forces parallel to the plane: the component of gravity, the viscous drag and the capillary force.

## § 1.6. Pinning on a line

In section 1.4 we saw that the contact line can be pinned by chemical or physical microscopic irregularities distributed on real surfaces, producing the contact angle hysteresis. Pinning may also occur on a single line obstacle when the surface is practically ideal, so that the contact angle away from the line is the one predicted by Young's law. This line can be the boundary between two regions of a flat surface with different chemical coatings, inducing a sharp wettability transition. Suppose that the two regions $S1$ and $S2$ have wettabilities defined by two Young contact angles $\theta_{E1}$ and $\theta_{E2}$, respectively, with $\theta_{E1} < \theta_{E2}$. When the contact line reaches the boundary coming from region $S1$ with contact angle $\theta_{E1}$ (for instance because of a volume increase of the drop), it remains pinned as long as the contact angle is comprised between $\theta_{E1}$ and $\theta_{E2}$, as shown in figure 1.12a:

$$\theta_{E1} < \theta < \theta_{E2}, \tag{1.16}$$

that in term of surface tensions it becomes

$$\arccos\left(\frac{\sigma_{S1G} - \sigma_{S1L}}{\sigma}\right) < \theta < \arccos\left(\frac{\sigma_{S2G} - \sigma_{S2L}}{\sigma}\right). \tag{1.17}$$

Once the contact angle $\theta$ exceeds $\theta_{E2}$ the contact line unpis and the liquid can pass in region $S2$.

Another case of pinning of the contact line is that on the edge between two flat half-plane with the same wettability, characterized by the Young contact angle $\theta_E$, forming an angle $\psi$ (see figure 1.12b). If the contact line is brought to the edge, it stays blocked until the contact angle $\theta$ satisfies the *Gibbs criterion*:

$$\theta_E < \theta < \theta_E + \pi - \psi. \tag{1.18}$$

An example of drop motion on a tilted flat surfaces with two regions characterized by different wettability can be found in [24], whereas the pinning at an edge is extensively studied in [78]. Another example of droplets with contact line pinned at the edge of square or circular pillars can be found in [79].

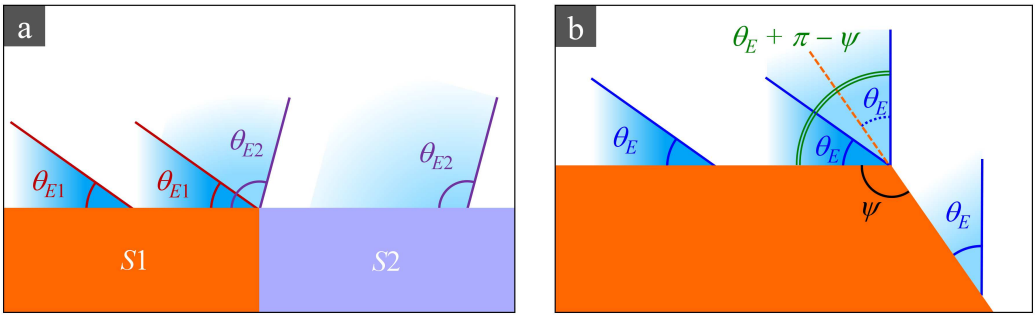


**Figure 1.12 :** (a) Pinning of the contact line at the boundary between two regions $S1$ and $S2$ with different wettability characterized by the Young contact angles $\theta_{E1}$ and $\theta_{E2}$, respectively. The contact line is pinned as long as the contact angle $\theta$ satisfies $\theta_{E1} < \theta < \theta_{E2}$. (b) Pinning of the contact line at the edge between two flat surfaces forming an angle $\psi$. The pinning condition is expressed by the Gibbs criterion $\theta_E < \theta < \theta_E + \pi - \psi$.

## § 1.7. Morphological transitions

On homogeneous flat surfaces, drops typically have an axisymmetric shape, in particular the shape of a spherical cap if the size is below the capillary length. The contact angle is the same all along the contact line and its value is predicted by Young's law, for smooth surfaces, or comprised between receding and advancing angles, for rough surfaces. We are now interested in drops on substrates characterized by surface modulations with length scale comparable to that of the drops (millimeter or sub-millimeter scale). This kind of modulated substrates can be exploited for the realization of open microfluidic systems. The two general strategies to modulate substrates employ:

- wettability patterns (e.g. hydrophobic substrate with hydrophilic domains, see figure 1.13a);
- nonplanar surface topographies (e.g. grooves with various cross-section, see figure 1.13b).

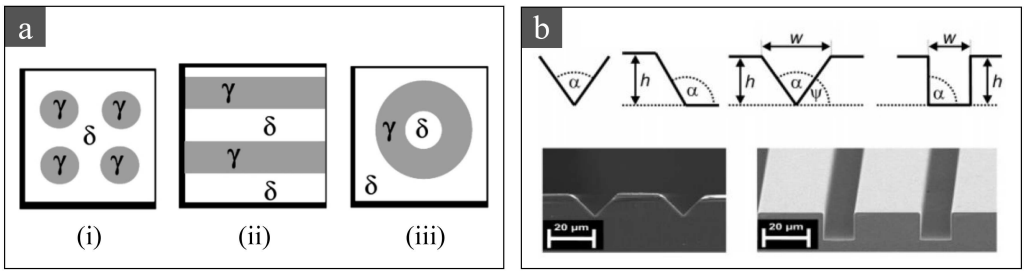


**Figure 1.13 :** (a) Top view sketch of different wettability patterns with hydrophilic domains $\gamma$ on hydrophobic matrix $\delta$ [80]. In the present text, the hydrophilic domains $\gamma$ and the hydrophobic matrix $\delta$ are denoted as $S1$ and $S2$, respectively. (b) Linear groove patterns: (top) sketch of various cross-sections; (bottom) SEM micrographs of triangular and rectangular grooves in silicon substrates [81].

In these cases, as described in the previous section, the contact line can be pinned on the wettability boundaries or on the edges and the contact angle can take values in the intervals defined by inequalities 1.16 or 1.18, respectively. This variability of the contact angle, combined with the geometry of the patterns, gives rise to complex scenarios featuring:

- a variety of interfacial shapes;
- novel instabilities of the liquid/gas interface;

- morphological transitions between different interfacial shapes.

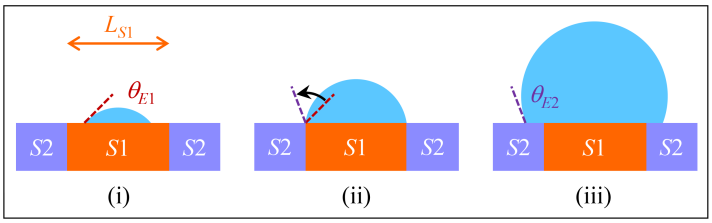


**Figure 1.14 :** Drop of increasing volume (from left to right) in the presence of a single circular hydrophilic domain $S1$, with diameter $L_{S1}$, on hydrophobic substrate $S2$. Given the axisymmetric geometry the drop is a spherical cap with contact angle: (i) $\theta = \theta_{E1}$ for small volume; (ii) $\theta_{E1} < \theta < \theta_{E2}$ for intermediate volumes; (iii) $\theta = \theta_{E2}$ for large volume.

The simplest example of wettability pattern is a single circular hydrophilic domain on an hydrophobic substrate (see figure 1.14). Given the axisymmetric geometry of the domain, a droplet can maintain the shape of a spherical cap even in the presence of the pattern. The only degrees of freedom in the shape are the contact angle and the size, depending on the drop volume. The interfacial behaviour becomes more interesting in the cases of a single domain with anisotropic geometry, a multiply connected single domain or a pattern of several disconnected domains [12, 80, 82–84] (see figure 1.15a-b). Some examples of this kind of patterns are shown in figure 1.13a-b. An interesting variety of interfacial morphologies is also present when substrates of different wettabilities are characterized by grooved topographies [13, 81, 85] (see figure 1.15c).

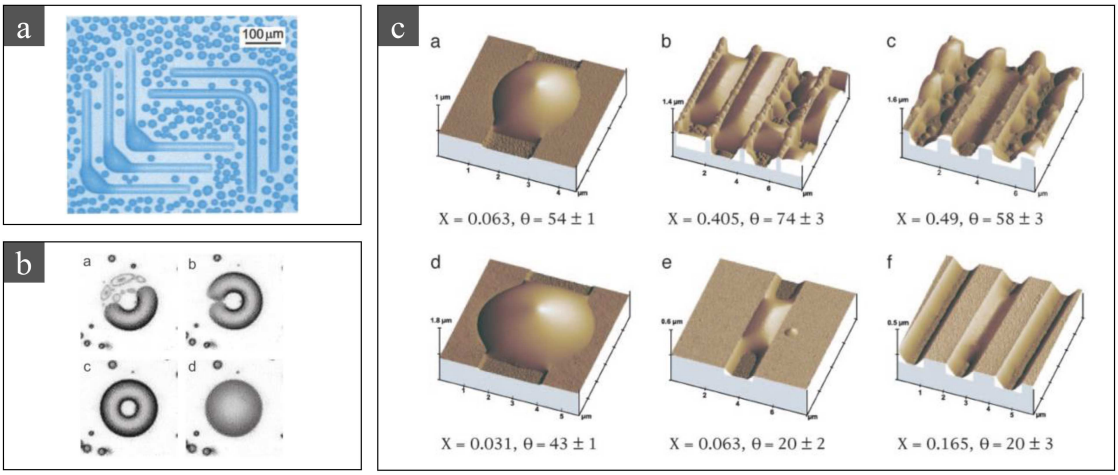


**Figure 1.15 :** (a) Liquid microchannels formed by water condensation on hydrophilic striped domains with corners [12]. For high enough liquid volume, the liquid interface undergoes an instability and bulges form at the corners. (b) Sequence of liquid morphologies, for increasing volume, on hydrophilic ring-shaped domains [84]. (c) AFM images of liquid structures in grooves with rectangular cross-section [13]. Different liquid morphologies can be observed, depending on the cross-section aspect ratio $X$ and the Young contact angle $\theta_E$.

Suppose that we deposit a drop on a hydrophobic substrate with a nontrivial pattern of hydrophilic domains. The morphology of the wetting layer is such as to maximize the contact area with the hydrophilic domains and, at the same time, to minimize the liquid/gas interface area. Depending on the particular pattern geometry and on the total volume $V$ of the wetting layer, several different morphologies may be stable and transitions between them can occur. Experimentally, it is convenient

to choose the total volume $V$ as control parameter by adjusting which it is possible to modify the shape of the liquid layer and induce these morphological transitions [80]. Each morphology is characterize by a total curvature $C$, that is constant on the whole interface, as predicted by Laplace law 1.6. In general, different morphologies have different total curvatures. It has been demonstrated [86] that a shape of maximal total curvature $C_{max}$ exists for any given position of the contact line. Consequently, when the contact line is pinned at the domains boundaries, each pattern geometry is characterized by an unique wetting morphology with maximal total curvature $C_{max}$ and corresponding volume $V(C_{max})$. For instance, in the simple case of a single circular hydorphilic domains (figure 1.14a) with diameter $L_{S1}$ the shape of maximal total curvature consists in an half sphere (which mens contact angle $\theta = \pi/2$) with the same diameter and volume $V(C_{max}) = (\pi/12)L_{S1}^2$.

We report, as an interesting example, the behaviour of liquid morphologies on a striped wettability pattern studied by Gau *et al.* [12] and Herminghaus *et al.* [82]. They produced a pattern of parallel highly hydrophilic stripes $S1$ ($\theta_{S1} \lesssim 5°$) by vapour thermal deposition of $MgF_2$ on a hydophobic silicone rubber substrate $S2$ ($\theta_{S2} \simeq 108°$). The geometry is that of pattern (ii) in figure 1.13a, with stripe width $L = L_{S1} = L_{S2} = 30$ $\mu$m, for both hydrophilic and hydrophobic surfaces. When the substrate is exposed to water vapour and cooled below the dew point, water condenses on the hydrophilic stripes $S1$[†]. At the beginning, when the condensed volume is small, the liquid on the domains $S1$ forms homogeneous channels shaped as cylindrical segments with uniform cross-section and contact line pinned on the boundaries (see figure 1.16a). As the volume grows the contact angle $\theta$ along the boundaries uniformly increases untill it exceeds the critical value $\theta = \pi/2$ and the channels undergo a sudden trasintion to a morphology in which each channel presents a single bulge (see figure 1.16b-c). For $\theta = \pi/2$, the the channel reaches the shape of an half cylinder corresponding to the maximal curvature $C_{max} = L/2$.

This transition can be explained by discussing the stability of the interface against liquid current fluctuations along the channel. We denote as $x$ the coordinate along the stripe and as $v(x)$ the local channel volume per unit length. If $r$ is the local curvature radius of the cylindrical surface the corresponding Laplace pressure is $p = \sigma/r = (2\sigma \sin\theta)/L$. Whereas the contact angle $\theta$ grows with $v$, the curvature $r^{-1}$ and, consequently, the pressure $p$ are not monotonic functions of $v$: if $\theta < \pi/2$ the pressure increases with $v$, while if $\theta > \pi/2$ pressure decreases with $v$. This means that:

- for $\theta < \pi/2$, a local positive fluctuation of $v$ causes a local overpressure which give rise to a restoring force against flow and the channel is stable;
- for $\theta > \pi/2$, a local volume increase in $x$ causes a local pressure decrease which fosters liquid flow into $x$ with a positive feedback and the channel is unstable

This instability, similar to the Plateau-Rayleigh instability [3,87], is the cause of the suddent transition to the bulged channel that occurs as soon as the contact angle exceeds $\pi/2$.

[†]The growth of droplets nucleating on hydrophobic surface $S2$ is prevented by the proximity (in the micrometric scale) of the channels on $S1$ because the much larger curvature of droplets respect to cilindrical channels results in a larger saturation pressure and hinders the condensation of water.

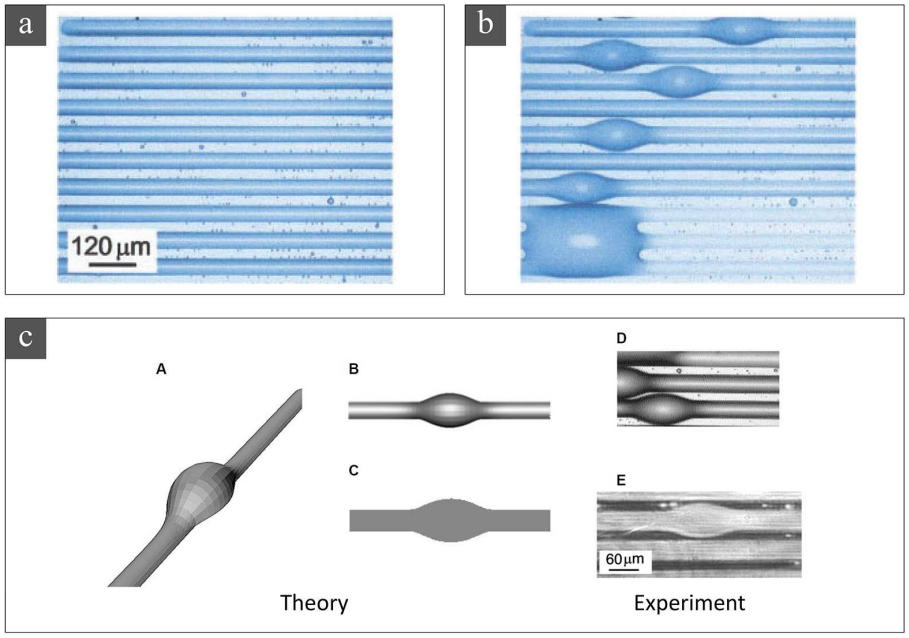


**Figure 1.16 :** Microchannels of water condensed on hydrophlic stripes [12]. (a) For small volume, the channels have uniform cross-section and small contact angle. (b) For large volume, the channels develop a bulge as soon as the contact angle exceed a critical value. (c) Comparison between theoretically predicted and experimentally observed shape of a bulged channel.

## § 1.8. Drops on oscillating substrates

Oscillations of free liquid drops have been investigated since the end of the $19^{\text{th}}$ century by Lord Kelvin [88] and Lord Rayleigh [89] and later by Lamb [90]. In particular, Lamb found a general expression for the resonance mode frequencies of capillary oscillations for a spherical liquid drop immersed in gas, in the absence of gravity (see also [91]):

$$f_r = \frac{1}{2\pi}\sqrt{\frac{l(l-1)(l+2)\sigma}{\rho R^3}} \tag{1.19}$$

with $l = 0, 1, ...$, density $\rho$ and radius $R$. For $l = 0$ and $l = 1$ the expression 1.19 vaishes. Due to the spherical simmetry, each mode $l$ has a $(2l+1)$-fold degeneracy. The mode $l = 0$ would represent radial oscillations, i.e. spherically symmetrical pulsations, that, for an incompressible fluid, are impossible. The mode $l = 1$ simply corresponds to a rigid traslatory motion. So, the fundamental mode is $l = 2$.

In the following, we focus on the behaviour of forced oscillations of sessile drops. This topics, unlike the case of free spherical drops, have been systematically studied just in the last decades [92–97], since the contact with the surface introduces an high complexity into the research for the eigenfrequencies, preventing analytic results. For instance, an issue arising from presence of the substrate is the dynamics of the contact line related to the contact angle hysteresis. In the case of a finite hysteresis, we can distinguish two regimes:

- for substrate acceleration below a characteristic threshold, i.e. small deformation of the drop profile, the contact line is pinned;

- for acceleration above the threshold, the profile deformation overcomes hysteresis and the contact line can move.

For sessile drops, the resonance modes are stationary surface waves on the liquid/gas interface, with a complicated three-dimensional wave pattern. Noblin *et al.* [95] devoloped an intuitive approximated model for the resonance frequencies of a pinned drop by assuming that the waves are one-dimensional and an integer or half-integer number of wavelength $\lambda$ fits along the profile length $L$, i.e. $L = n\lambda_n/2$, where $n = 1, 2, ...$ is the mode number (see figure 1.17a). The corresponding wavenumber is

$$q_n = \frac{2\pi}{\lambda_n} = \frac{\pi n}{L}. \tag{1.20}$$

The mode $n = 1$ requires a change in volume, which is not possible for drop with pinned contact line due to the incompressibility of the fluid. So the first allowed mode is $n = 2$.

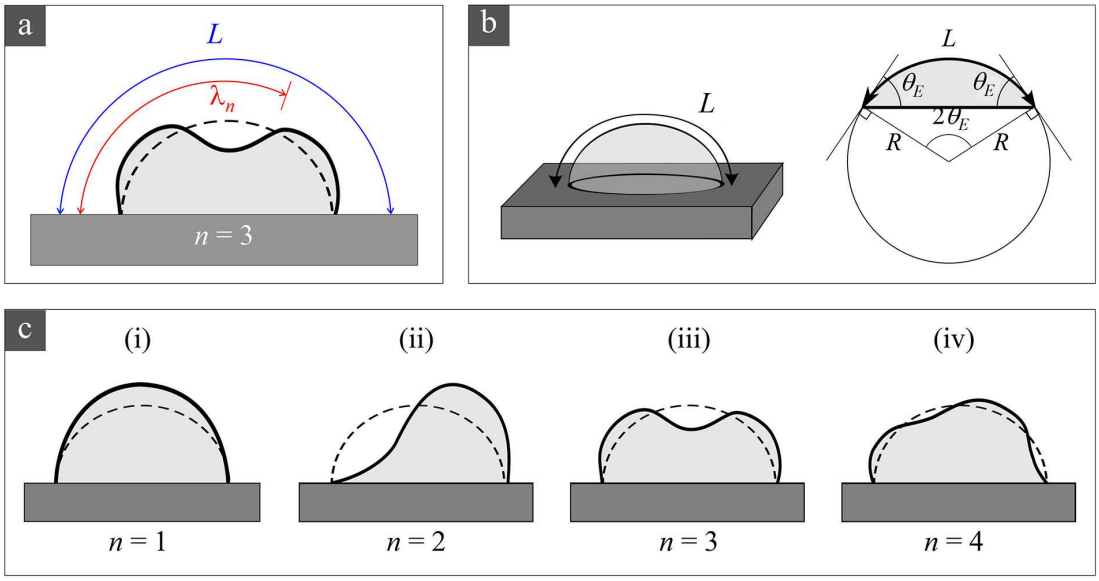


**Figure 1.17 :** (a) Wavelength $\lambda_n = (2/n)L$ of a 1D standing wave on the drop profile of lenght $L$ with pinned contact line. (b) Sketch of the profile of a drop with spherical cap shape. The profile length is given by $L = 2\theta_E R$, with $R$ curvature radius and $\theta_E$ equilibrium contact angle [98]. (c) Shapes of the $n = 1, 2, 3, 4$ modes. The mode $n = 1$ is not possible for drop with pinned contact line due to the incompressibility of the fluid. The first allowed mode is $n = 2$ [97].

In general, the profile length $L$ depends on drop volume and equilibrium contact angle. For small drops (below $\kappa^{-1}$) the length is simply $L = 2\theta_E R$, with $R$ curvature radius (see figure 1.17b). On the other hand, for flattened drops (above $\kappa^{-1}$) no analytical expression exists and $L$ has to be calculated numerically. The frequency of the resonant modes can be obtained from the expression for one-dimensional *capillary-gravity waves* on a liquid bath with finite depth $h$ [91], by taking, according to Noblin and co-workers, as the depth of the bath the mean height of the drop profile $h_m = V/(\pi r^2)$, where $r$ is the contact area radius and $V$ the drop volume:

$$f_n = \frac{1}{2\pi}\sqrt{\left(gq_n + \frac{\sigma}{\rho}q_n^3\right)\tanh\left(q_n\frac{V}{\pi r^2}\right)}. \tag{1.21}$$

Although this model is relatively simplistic, this result agrees well with experimental observations for drops flattened by gravity on an moderately hydrophilic substrate ($\theta_E = 85°$) [95].

If the drop size is below the capillary length, the gravitational effects can be ignored and the expression for the resonance modes frequencies of *capillary wave* becomes [91, 97]:

$$\begin{aligned} f_n &= \frac{1}{2\pi}\sqrt{\frac{\sigma}{\rho}q_n^3 \tanh\left(q_n \frac{V}{\pi r^2}\right)} \\ &= \frac{1}{2\pi}\sqrt{\frac{\sigma}{\rho}\left(\frac{\pi n}{2\theta_E}\right)^3 \tanh\left(q_n \frac{V}{\pi r^2}\right)} R^{-3/2} \end{aligned} \tag{1.22}$$

where, in the second line, we show the dependence of the resonant frequencies on the curvature radius $R$.

The elongation of a drop deposited on a surface characterized by an anisotropic wetting as shown in figure 1.18, due to substrate corrugation on length scale much smaller than the drop size, causes the splitting of the fundamental mode in two eigenfrequencies associated to standing waves on the drop profiles along the major and the minor axes [97]. In this case the two wavenumbers are $q_{long} = 2\pi/L_{long}$ and $q_{short} = 2\pi/L_{short}$, with $L_{long}$ and $L_{short}$ the profile lengths corresponding to major and minor axes, respectively.

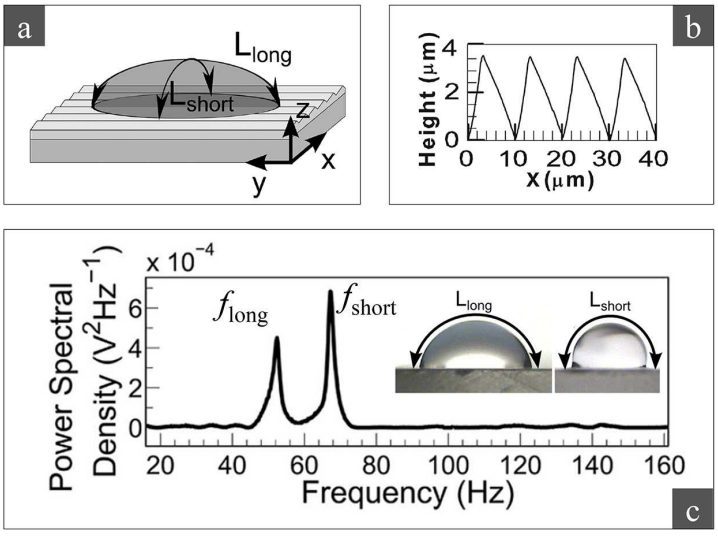


**Figure 1.18 :** Resonance mode of an elongated sessile drop. (a) Sketch of the geometry of a droplet placed on a surface patterned with horizontal grooves. The diagram illustrates how the long and the short profile lengths,$L_{long}$ and $L_{short}$ of the aspherical drop are defined. (b) AFM line profile of the substrate topography. (c) The power spectral density of the oscillations of the drop interface exhibits two peaks corresponding to capillary waves along the long and the short profiles, shown in the inset [97].

The simplest methods to apply forced oscillations to sessile drops employ vertical or horizontal harmonic oscillations of a horizontal substrate(see figure 1.19). The corresponding resonance modes are referred as *pumping modes* and *rocking modes*, respectively. We consider the case of rigid vibrations of the substrate, not to be confused with that of surface acoustic waves (SAW) on the substrate [17].

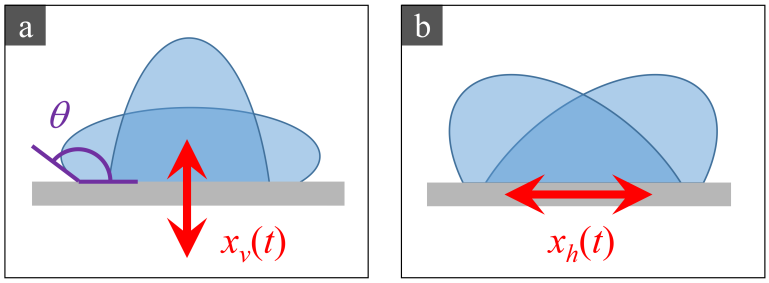


**Figure 1.19 :** Sessile drops on substrates subject to: (a) vertical oscillations (*pumping modes*); (b) horizontal oscillations (*rocking modes*).

### § 1.8.1. Vertical harmonic oscillations

First, we consider the case of a sessile drop lying on a horizontal substrate subject to vertical harmonic oscillations, as studied by Noblin and co-workers [95]. The acceleration of the substrate is given by:

$$a(t) = -(2\pi f)^2 A \cos(2\pi f t) \tag{1.23}$$

where $f$ and $A$ are the frequency and the maximum amplitude of the oscillations, respectively. As mentioned above, depending if the acceleration is smaller or larger the a characteristic threshold, the drop contact line can be completely pinned or can display an oscillatory movement, respectively. In the pinned contact line regime the oscillatory deformations of the drop profile preserve the axial symmetry. In the moving contact line regime, for some special conditions, the axial symmetry of drops with size larger than $\kappa^{-1}$ can be broken. It happens above a second higher acceleration threshold and for particular frequencies. These particular oscillation modes are called *triplons* [99]. Here we take into consideration just the case of axisymmetric oscillations.

In the pinned contact line regime we can apply equation 1.21 to find the resonance frequencies but the modes with even $n$ are forbidden, due to the symmetry of the system. Only the modes in which a half-integer number of wavelengths fits in the drop profile length, i.e. $(j - 1/2)\lambda_j = L$ (with $j = 2, 3, ...$), can be excited by vertically oscillating the substrate. With this new classification the modes $j$ correspond to the odd modes $n$, i.e. $n = 2j-1$ and the wave vector is given by $q_j = \pi(2j-1)/L$.

For an ideal substrate with no hysteresis the oscillations induce a periodic motion of the contact line with constant contact angle $\theta = \theta_E$. In this case, as depicted in figure 1.20b, an integer number of wavelengths fits in the profile length, i.e. $k\lambda_k = L$ (with $k = 1, 2, ...$). The integer $k$ corresponds to half the number of nodes along the drop interface.

In the more realistic case of a substrate with finite hysteresis and large acceleration, we have neither fixed conact line nor constant contact angle $\theta$ but, rather, a stick-slip motion of the contact line that displaces when $\theta > \theta_A$ or $\theta < \theta_R$ and remains pinned when $\theta_R < \theta < \theta_A$. In this kind of drop deformation both the contact line radius and the contact angle undergo periodic but non-harmonic oscillations, as shown in figure 1.20c.

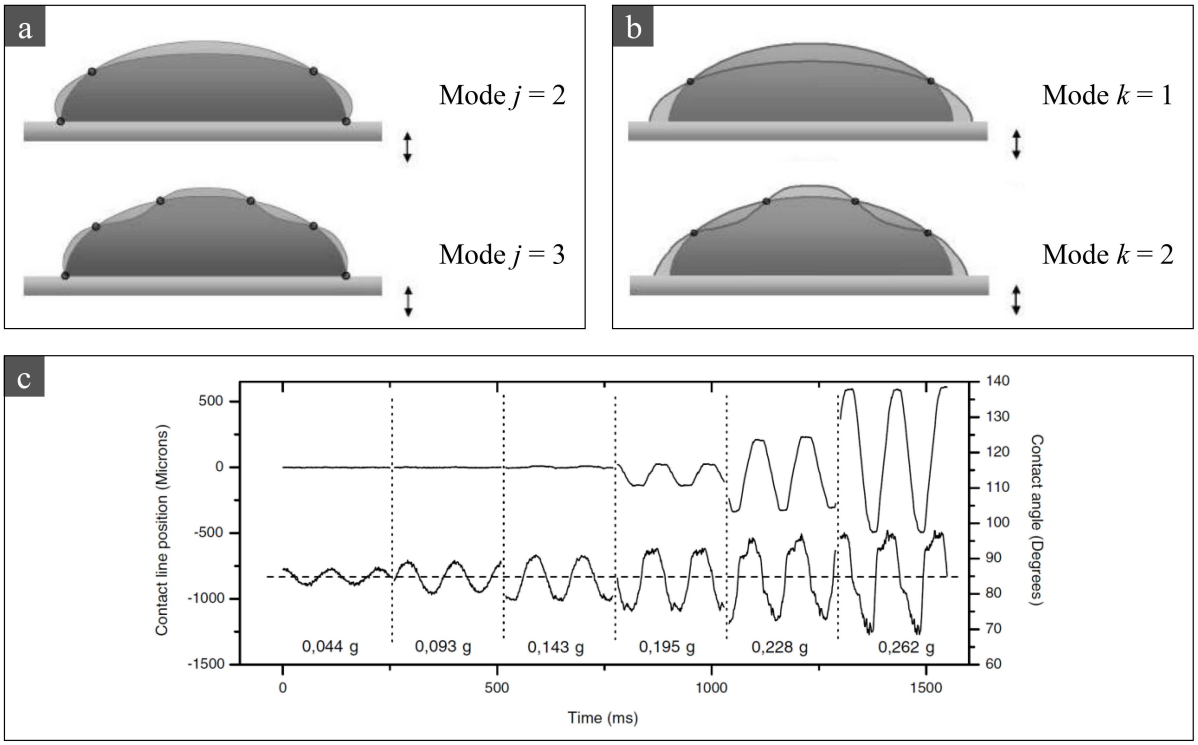


**Figure 1.20 :** Drop oscillations induced by harmonic vertical vibrations of the substrate. (a) First two modes $j = 2$ (4 nodes) and $j = 3$ (6 nodes) for a drop with pinned contact line. (b) First two modes $k = 1$ (2 nodes) and $k = 2$ (4 nodes) for a drop with moving contact line. (c) Transition between stick and stick-slip motions of the contact line. Lower curves are time evolutions of contact angle. The dashed line represents the equilibrium contact angle $\theta_E$. Higher curves are time evolutions of the contact line position around the starting position before vibrations. The six curves for different acceleration amplitudes, with fixed frequency $f = 9$ Hz and volume $V = 1$ mL, are joined together in the same plot for comparison [95].

### § 1.8.2. Horizontal harmonic oscillations

The oscillation modes with even $n$ are associated with horizontal harmonic vibrations of the substrate. The fundamental mode, corresponding to $n = 2$, has been studied by Celestini and Kofman [94]. They proposed a semianalytic expression for the first eigenfrequency of a drops with spherical cap shape and pinned contact line. In this model, the deformation of the drop is characterized by a displacement $dx$ of th center of mass and by a variation $\delta\theta$ of the contact angle. Assuming a symmetric variation, front and rear (with respect to the direction of the deformation) contact angle are given by $\theta_{front} = \theta_E + \delta\theta$ and $\theta_{rear} = \theta_E - \delta\theta$, respectively (see figure 1.21a). The corresponding surface variation can be written as

$$\Delta S = S_0 f(\theta_E)\delta\theta^2, \tag{1.24}$$

where $S_0$ is the surface of the drop at equilibrium and $f(\theta_E)$ is a geometrical factor depending on the equilibrium contact angle. The displacement of the center of mass is

$$dx = g(\theta_E)R\delta\theta, \tag{1.25}$$

where $R$ is the radius of curvature and $g(\theta_E)$ is another factor related to the drop shape. Combining equations 1.24 and 1.25 we have

$$\Delta S = \frac{S_0 h(\theta_E)}{R^2} dx^2, \tag{1.26}$$

with $h(\theta_E) = f(\theta_E)/g(\theta_E)^2$. A restoring force due to the surface tension $\sigma$ opposes deformation:

$$F = -\frac{\sigma \Delta S}{dx} = -\frac{\sigma S_0 h(\theta_E)}{R^2} dx. \tag{1.27}$$

Given the linear dependence of $F$ on $dx$, we can define an effective elastic constant $k_e$, from which we can obtain the frequency of the fundamental mode, $f_0 = (1/2\pi)\sqrt{k_e/(\rho V)}$. Considering the geometrical expressions for the surface $S_0$ and the volume $V$ of a spherical cap, we can write:

$$f_0 = \frac{1}{2\pi}\sqrt{\frac{\sigma}{\rho}\frac{6h(\theta_E)}{(1-\cos\theta_E)(2+\cos\theta_E)}} R^{-3/2}. \tag{1.28}$$

The geometrical factor $h(\theta_E)$ has been numerically computed with the hypothesis that the deformation corresponds to the equilibrium shape under a constant external force, by means of the program *Surface Evolver* [100] (see figure 1.21b). We can observe that the dependence of $f_0$ on the curvature radius $R$ is the same found in expression 1.22. The experimental data well reproduce this power law, with a slight underesteem. A better agreement can be found substituting in 1.28 an effective contact angle $\theta_{eff} < \theta_E$, which takes into account the fact that the momentum transfer from the substrate to the drop, due to the fluid viscosity, occurs in a layer of thickness of the order of the *Stokes length* [91].

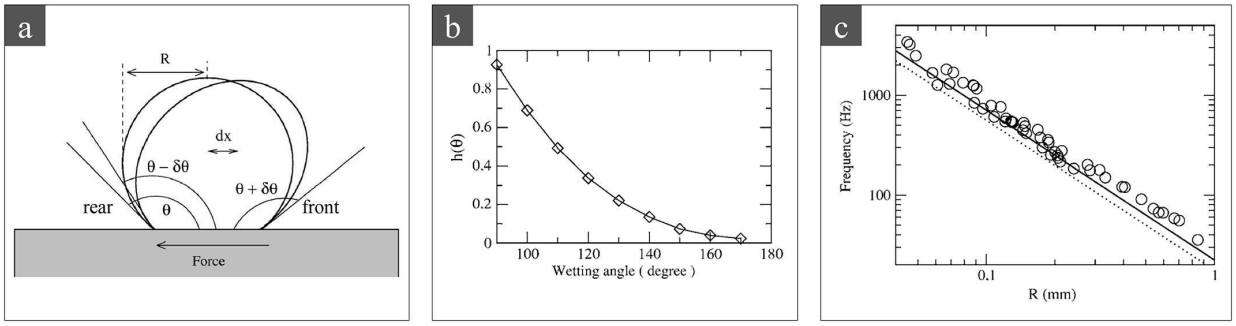


**Figure 1.21 :** Fundamental mode of drop oscillations induced by harmonic horizontal vibrations of the substrate. (a) Sketch of the drop deformation due to an external force. The deformation induces a displacement $dx$ of the center of mass and a variation $\delta\theta$ of the front and rear contact angles. (b) Numerical values obtained for $h(\theta_E)$. (c) Fundamental mode frequency as a function of the drop curvature radius $R$. Circles are experimental data, the dotted and the solid lines represent the result of equation 1.28 using $\theta_E$ and $\theta_{eff}$, respectively [94].

### § 1.8.3. Combination of vertical and horizontal oscillations

We saw that for high enough acceleration, the deformation of the drop profile, induced by vertical or horizontal harmonic oscillations of the substrate, is associated to the displacement of the contact line. Nevertheless, a net movement of the drop over a period cannot be achieved due to the left-right symmetry of the system:

- in the pumping modes, diametrically opposite point of the contact line displace in opposite directions;
- in the rocking modes, the contact line moves with equal and opposite displacements during two consecutive half-cycles.

There are several methods to break such a symmetry, for instance, by employing substrates with a wettability gradient [101] or by applying asymmetric horizontal vibrations [18, 38]. Another way to break the left-right symmetry and to achieve a net displacement of the drop is to apply a superposition of horizontal ($h$) and vertical ($v$) harmonic oscillation to the substrate (see figure 1.22a) [30]:

$$\begin{cases} x_h(t) = A_h \cos(2\pi f t) \\ x_v(t) = A_v \cos(2\pi f t + \Delta\Phi) \end{cases}, \tag{1.29}$$

where $A_h$ and $A_v$ are the maximum oscillation amplitudes, $f$ is the oscillation frequency and $\Delta\Phi$ is the phase shift between the two oscillations. With this combination, when the drop is deformed by the horizontal oscillations, the deformation is different whether the vertical movement of the substrate is upward or downward, leading to different displacements in one direction respect to the opposite one. Consequently, the drop performs a net displacement at each cycle, progressively moving in one direction (see figure 1.22b-c). The direction and the absolute value of the drop net velocity depend on the phase shift $\Delta\Phi$ and on the maximum oscillation amplitudes, as shown in figure 1.22d-e. Hence the possibility of control the drop motion by tuning these parameters.

As described in chapter 2, a similar superposition of oscillations in directions parallel and perpendicular to the substrate is obtained by vertically vibrating an inclined plane [39, 102]. In this

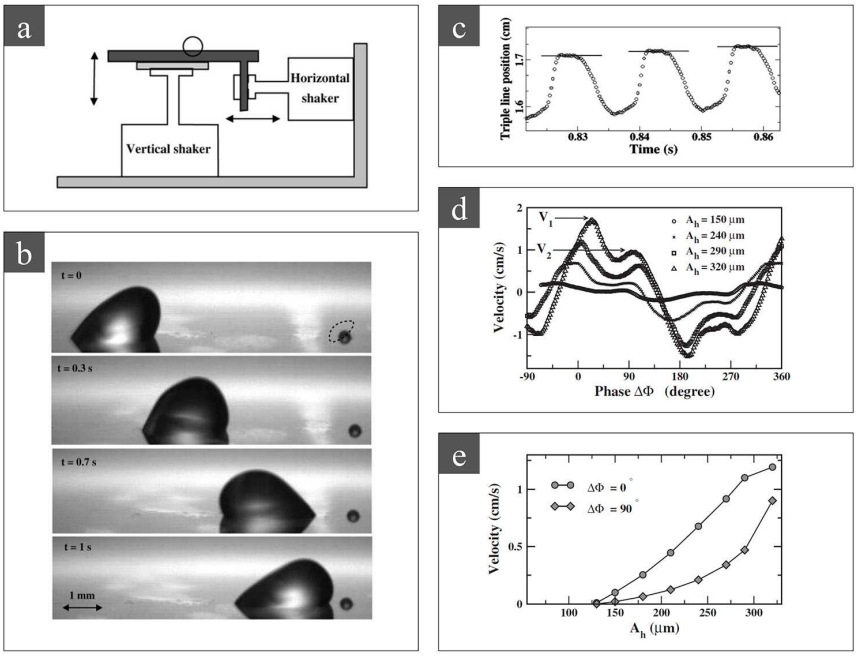


**Figure 1.22 :** (a) Experimental setup used to combine vertical and horizontal vibrations of the substrate. (b) Images taken from different vibration cycles at various oscillation phases. (c) Time evolution of the position of the right end of the contact line. (d) Drop velocity as a function of the phase shift $\Delta\Phi$ for various horizontal oscillation amplitude $A_h$. (e) Drop velocity as a function of $A_h$ [30].

way, the components of the oscillations in the two orthogonal directions are always in phase and the deformation of the drop profile is not symmetric due to the non-null component of gravity along the plane. Depending on oscillation frequency and maximum acceleration, the drop can move upward or downward.

# Chapter 2

# Drop motion induced by vertical vibrations

In section 1.8, we saw the possibility of induce the motion of a sessile drop by means of oscillations of the substate. This method is particularly promising because the wide field of application to any kind of drops, due to the inertial coupling with the liquid. For instance, it is not limited only to polar fluids as in the case of electrowetting techniques. The active control on the one-dimensional motion of the drop can be achieved by a superposition of oscillations in the directions parallel and perpendicular to the solid surface, by tuning amplitudes and phase shift between the two independent oscillations [30]. A similar result can be obtained by vertically vibrating an inclined plane, as first shown by Brunet and collaborators [39]. Given the complexity of this problem, in this chapter we present a further investigation of this latter system, from both the experimental and theoretical/numerical point of view [102], aimed to a better understanding of the drop dynamics, which can allow a practical exploitation of the phenomenon.

After an introduction (section 2.1) about drop actuation and application of substrate vibrations, in sections 2.2 and 2.3 we illustrates our experimental procedure and the numerical method, respectively. The latter consist in 2D simulations performed by Prof. Casciola's group (La Sapienza - University of Rome, Dept. of Mechanical and Aerospace Engineering). Sections 2.4 and 2.5 describe the experimental and the numerical results, wich are summarized in the conclusion (section 2.6).

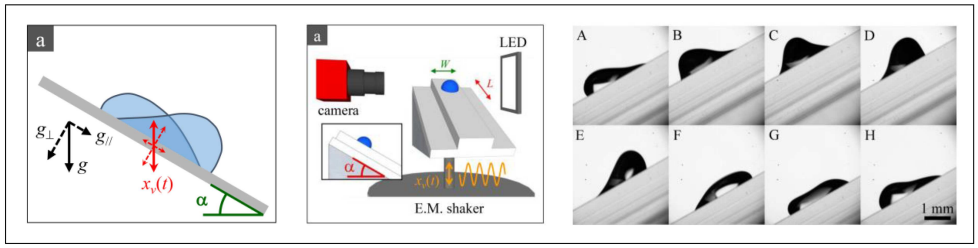

## § 2.1. Introduction

A drop deposited on a substrate, tilted with respect to the horizontal by a sufficiently small angle, does not move. Inclining the substrate above a certain characteristic angle induces downward sliding of the drop because of gravity. On a flat, homogenous surface sliding occurs at a characteristic constant speed $U$, which increases with the inclination angle. Such a motion is the result of a balance between the down-plane component of the drop weight and the viscous resistance, plus a capillary force related to the nonuniformity of the contact angle along the drop perimeter [74, 103]. Patterning the surface with parallel lyophilic and lyophobic stripes causes a stick-slip motion whose average speed is an order of magnitude smaller than that measured on a homogeneous surface having the same static contact angle [104]. More generally, experiments on chemically heterogeneous surfaces formed by domains of various shapes printed on substrates having different wettability and arranged in diverse symmetric patterns [26, 105, 106] show that the chemical pattern of a surface can passively tune the sliding behaviour of drops. A surface having a spatial gradient of hydrophobicity is also capable of causing drops of water placed on it to move upward [107]. Recently, upward motion of drops on inclined heterogeneous substrares has also been theoretically analyzed [108].

For polar liquids, electrowetting provides an active way to control drop motion on a solid surface [31]. Fluid manipulations at the microscale and beyond are powerfully enabled through the use of ultrasonic surface acoustic waves (SAW) [17]. A more exotic drop actuation relies on the so-called Leidenfrost phenomenon, that is the levitation of drops on a cushion of vapor produced when they are brought in contact with a hot solid [109]. Vibrations of the substrate are also used as an active way to control drop motion of any liquid because they couple to the liquid inertia. For instance, as we saw in section 1.8, drops on a horizontal plane subject to a superposition of parallel and perpendicular harmonic oscillations can overcome hysteresis and move [30]. Interestingly, Brunet *et al.* [39, 110] found that drops on an inclined plane subject to sufficiently strong vertical vibrations can climb against gravity.

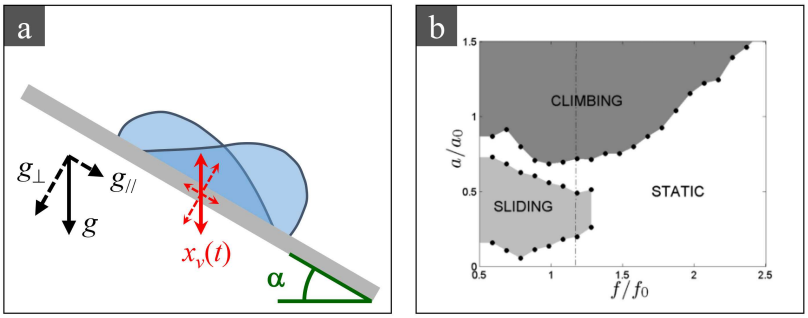


**Figure 2.1 :** (a) Sketch of the verically oscillating substrate with inclination *alpha*. (b) Phase diagram of the motion of a drop with volume $V = 5$ $\mu$L and kinematic viscosity $\nu$=31 mm$^2$/s. The inclination angle is $\alpha$=45°. The normalization factors are $f_0$= 50.77 Hz and $a_0$=174 m/s$^2$ [39]

The surprising drop climbing was originally explained as a breaking of the front-back symmetry of the oscillating drop and a nonlinear friction law between the drop and the plane [39]. This phenomenon was also studied theoretically assuming thin, two-dimensional drops. John and Thiele [111] examined the limit of low Reynolds numbers and modeled the drops contact line by precursor films due to van

der Waals forces. They found that the component of the vibration orthogonal to the plate induces a nonlinear response in the drop shape that causes an anharmonic response of the drop to the parallel vibration component. Benilov and Billingham [112] analyzed the opposite limit of low viscosity, with contact lines governed by a contact-line law and observed that the climbing motion is due to an interaction of oscillatory modes induced by vibrations. These studies were then extended to a first 3D modelling of climbing drops on oscillating substrates under the assumptions of weak vibrations, low viscosity and inertia of the liquid, thin drops and contact-line law [113]. The main conclusion was that, at low frequency, the 2D model [112] is qualitatively incorrect because it predicts that 2D drops can climb only for a very large acceleration of the plate, whereas, for 3D drops, the acceleration can be finite.

To better clarify this intriguing phenomenon, we have systematically studied the dynamics of various water solutions covering an ample range of kinematic viscosities and dynamic contact angles. The measurements have been compared with the results of numerical simulations based on a diffuse interface approach, performed by Prof. C.M. Casciola's group (La Sapienza - University of Rome, Dept. of Mechanical and Aerospace Engineering). In particular, the Cahn-Hilliard / Navier-Stokes (CHNS) model has been chosen because of its proven ability to handle the contact line dynamics [114, 115]. It is also embedded with capillary stresses all along the droplet interface and handles extreme interface deformations, up to the droplet breakup [116]. Several other approaches have been exploited to study flows with contact line motion [117]. Recently Kim *et al.* [118] applied a Lattice Boltzmann Method (LBM) to study the dynamics of a droplet on a moving wall, analyzing the effect of the wettability on the onset of the droplet pinch off. The motion onset of a drop on a homogenous plane, driven by a body force, was also investigated by Semprebon *et al.* [71] by means of the Surface Evolver. Sbragaglia *et al.* [119] instead applied a LBM to examine the sliding dynamics of a droplet on a heterogeneous patterned wall. A similar problem was investigated in [120] by means of the CHNS model. The Volume of Fluid method has also been applied to the sliding droplet problem and the influence of the contact angle hysteresis [121]. However, to the best of our knowledge, the motion of a droplet on a vibrating plate has not been studied using numerical methods which account for the fluid dynamics of the complete binary system. This is a challenging problem from the modeling and the computational points of view since the non-equilibrium contact angle dynamics plays a crucial role, especially in the high frequency range.

## § 2.2. Experimental details

The first issue of most part of wettability characterizations or capillary phenomena studies is the experimental observation of the shape of drops or, more generally, of liquid interfaces, from which several useful information can be obtained (e.g. contact angles, curvature radius, etc.). The first step is the acquisition of optical images of the drop profile, then the physical quantities required can be extracted by means of digital imaging techniques. The basic experimental apparatus needs a digital camera equipped with the proper optics, a light source and some device to supply small and controlled liquid volumes.

### § 2.2.1. Contact angles measurements

The setup we have used for the measurement of static and dynamic contact angles which characterize sessile drops of several liquid solutions on different substrates is represented in figure 2.2. It consists in:

- a horizontal sample holder whose height and position can be set by means of micrometric translators;
- a vertical syringe pump system (UltraMicroPump UMP3, World Precision Instruments) that allows the deposition of drops with controlled volume;
- two CCD cameras (Manta G-146, Allied Vision Technologies) with orthogonal line of view, equipped with 2× telecentric objectives (VS-TC2-110, VS Technology). Each camera can acquire image sequences with sample rate up to 17 Hz;
- two blue LED sources (Phlox), focused in the center of the sample holder, to back-illuminate the drop.

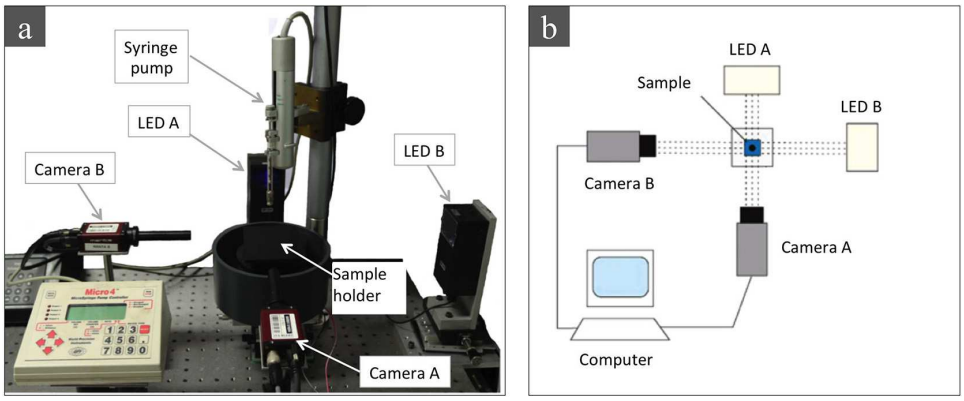


**Figure 2.2 :** Picture (a) and top view sketch (b) of the experimental setup for contact angle measurements.

The configuration with two orthogonal line of view allows the characterization of the wetting properties of anisotropic substrates, featuring grooves or striped wettability domains, such as those reported in section 1.7. The back-illumination of the drop results in a dark sharp contour on bright background (see figure 2.3), which is the best condition for the profile detection. Then, the acquired images are analyzed by means of a homemade program, developed in the LabVIEW environment. The software finds the drop profile, based on a contrast threshold, and fits its points with a polynomial curve (see figure 2.3b). By calculating the intersections of the interpolated profile with the baseline of the substrate and the tangent lines, we can determine the contact points positions and the contact angles.

By means of this setup, we have characterized the wettability of the substrates with respect of each liquid solution by measuring the equilibrium contact angle $\theta_E$ and the advancing (receding) contact angle $\theta_A$ ($\theta_R$). In particular, $\theta_A$ and $\theta_R$ are measured, respectively, by progressively inflating and deflating a drop deposited on the horizontal surface with the syringe pump (as sketched in figure

1.8a) and observing the profile when the contact line starts moving. This study is completed with the determination of the contact angle hysteresis $\Delta\theta = \theta_A$ - $\theta_R$, which quantifies the surface pinning. We have also measured the surface roughness of the top face of the PMMA ridge with a profilemeter and got an rms value less than a couple of nm.

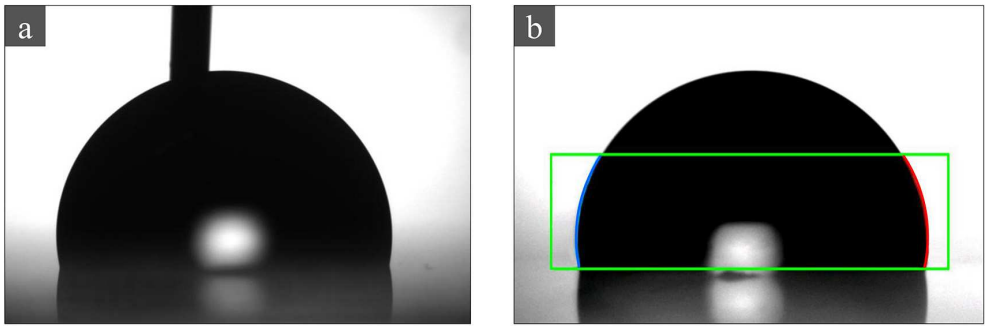


**Figure 2.3 :** Typical drop image for wetting studies. The back-illumination results in a dark drop on bright background. (a) Drop just deposited on the substrate. The needle of the syringe is still inside the drop. (b) Detection of the drop profile close to the contact points. The contact angle can be obtained from the polynomial fit of the contour.

### § 2.2.2. Oscillatory dynamics observation

We have studied the dynamics of drops deposited on inclined poly(methyl methacrylate) (PMMA) wedges attached to the moving shaft of an electromagnetic shaker (LDS V101 Brüel & Kjær) as shown in figure 2.4a.

In preliminary experiments [122–124] we considered different inclination angles $\alpha$ (30°, 45° and 60°) into account. For inclination at 60° the gravitational pull prevails and climbing is practically hindered. Eventually we focused on 30° inclination because the not too large influence of gravity allows climbing for a wide range of frequency and acceleration.

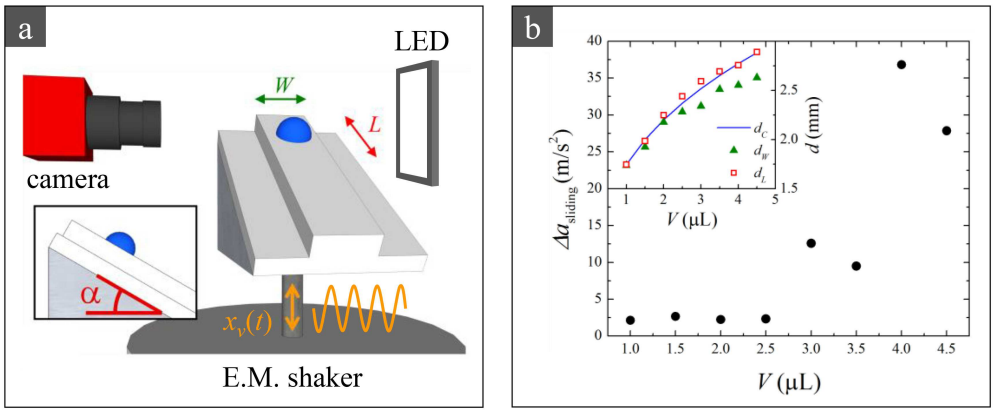


**Figure 2.4 :** (a) Schematic drawing of the experimental setup. The drop is placed on a PMMA ridge with width $W = 3$ mm. Side-view images of the back-illuminated drop are acquired by a fast camera. (b) Dispersion of the acceleration threshold for sliding $\Delta\ a_{sliding}$ as a function of the drop volume for a ridge with a width of 3 mm oscillating at a frequency of 80 Hz. Inset: comparison of the expected diameter $d_C$ of a hemispherical sessile drop of volume with the measured longitudinal $d_L$ and transversal $d_W$ elongations of the contact line.

The shaker oscillates vertically in the frequency range 10 Hz -10 KHz with a maximum amplitude

of 2.5 mm and the maximum force it can exert is 8.9 N. A mismatch in the location of the wedge mass center with the shaker axis may cause horizontal oscillations at certain resonance frequencies that can significantly affect the drop dynamics. To avoid this problem, we took particular care to balance the wedge on the axis by adding some extra little loads at specific points. Figure 2.5 shows the results of this tuning operation. The top image represents a portion of the screw attached to the wedge with the shaker off. The middle image shows the screw vibrating at a frequency of 65 Hz and amplitude of 100 $\mu$m during an exposure time of 50 ms. The shadows of the contour clearly indicate that there is a horizontal oscillation with an amplitude of about 200 $\mu$m superimposed to the vertical vibration. The bottom image refers to the shaker driven at the same conditions as above but after the tuning the center of mass of the wedge. The motion is now purely along the vertical direction. Similar tests have been carried at different frequencies and amplitudes, in particular close to the maximum driving amplitude.

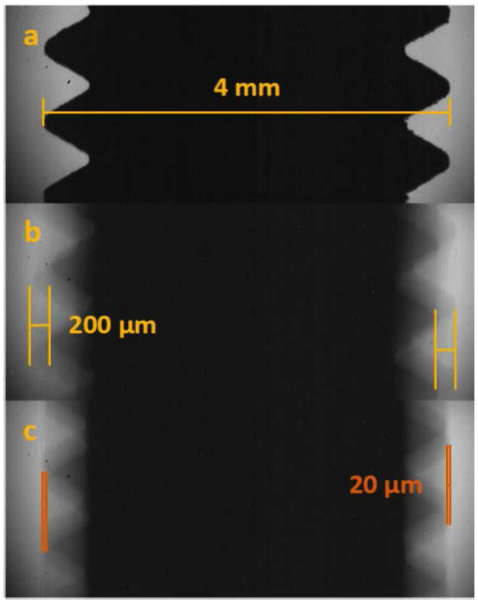


**Figure 2.5 :** (a) Shaker off. (b) Shaker driven at a frequency of 65 Hz and amplitude of 100 $\mu$m. Vertical and lateral vibrations can be detected from the shadows at the contour. (c) Shaker driven at the same conditions as above but after the tuning the center of mass of the wedge.The horizontal vibrations are now highly reduced.

In order to constrain the drop motion to one dimension, we have sculpted channels of different cross-sections (circular, triangular and rectangular) and different widths (from about 0.2 mm to 4 mm) along the direction of the tangential component of the acceleration of gravity [124]. The one we found most effective is a square ridge having height of 2 mm and width of 3 mm (see figure 2.4a). Its vertical extension allowed us to more easily focus the side-view camera to the drop back-lighted by the diffuse LED source. For the detection of drop shape, contact angles and contact points during vibrations we exploited a fast camera (Phantom v7.3, Vision Research) with full-frame sample rate up to 8 kHz, equipped with a 2× telecentric objective.

To find the most appropriate drop volume, we have systematically investigated the reproducibility of the drop dynamics. Water drops of increasing volume are deposited by means of the vertical syringe pump at the center of the ridge. The drops are initially pinned to the surface. Vertical oscillations of the substrate above a given acceleration $a_{sliding}$ cause a downward sliding of the drop. The graph

of figure 2.4b shows the dispersion of the acceleration threshold for sliding $\Delta a_{sliding}$ measured as a function of the drop volume for a ridge with a width of 3 mm and an oscillating frequency of 80 Hz. The dispersion $\Delta a_{sliding}$ is the root mean square deviation calculated from a statistical ensemble of at least five data points acquired at the same nominal conditions. The graph shows a sudden increase in $\Delta a_{sliding}$ just above 2.5 $\mu$L. We explain it as due to the interaction of the drop contact line with the lateral, irregular edges of the ridge. Actually, the inset compares the expected diameter $d_C$ of a hemispherical sessile drop of volume $V$ with the measured longitudinal $d_L$ and transversal $d_W$ elongations of the contact line. At small volumes, these three quantities coincide confirming that the contact line is circular. Above 2.5 $\mu$L, $d_W$ lies below $d_C$ confirming that one side of the contact touches the edge. The fact that $d_L$ remains equal to $d_C$ means that the lateral contact angle is increased because of the geometric pinning at the edge (see section 1.6).

In our study we have then used drops of 2 $\mu$L because they can be easily and accurately detected with our optical set-up. Furthermore, the lateral extension of the ridge guarantees that during their motion the lateral displacement amounts to no more than 0.4 mm, otherwise they will pin to or fall down the edges. In this way, we can accurately track the (one-dimensional) motion of drops by using only one video camera. We have also compared the sliding of 2 $\mu$L water drops on the ridge with that on a flat surface and could not detect any appreciable difference between the two substrates.

Besides distilled water, we have also studied glycerol/water, ethanol/water and isopropanol/water solutions at different concentrations. In addition, we have modified the wettability of the PMMA by coating it with trichloroperfluorooctylsilane by vapour phase deposition. Their main physical parameters, together with the static and dynamic contact angles and contact angle hysteresis, are listed in table 2.1. The values of density $\rho$, viscosity $\eta$ and surface tension $\sigma$ refer to a temperature of 25°C and have been deduced from literature [125, 126]. The addition of ethanol and isopropanol mainly decreases the surface tension of the mixture, while that of glycerol increases the viscosity. The kinematic viscosities $\nu$ of these mixtures cover the range 1-39 mm$^2$/s, much wider than the interval between 31 and 55 mm$^2$/s of the glycerol-water mixtures originally studied by Brunet *et al.* [39].

## § 2.3. Numerical method

The numerical simulations modelling a drop on an oscillating surface are based on a diffuse interface approach, the Cahn-Hilliard / Navier-Stokes (CHNS) model, to deal with the flow of two immiscible fluids where capillary effects and contact line motion play a crucial role on the fluid dynamics. Here we briefly introduce the mathematical model with particular attention to the boundary conditions and we refer to [114, 115, 127, 128] for a detailed derivation and some applications.

The binary system constituted by two pure, immiscible fluids $A$ and $B$ of density $\rho_A$ and $\rho_B$, respectively, is described by a scalar function, the *phase field* $\Phi(\mathbf{x}, t)$, defined as

$$\Phi(\mathbf{x}, t) = \frac{2\rho(\mathbf{x}, t) - (\rho_A + \rho_B)}{(\rho_A - \rho_B)}, \tag{2.1}$$

where $\rho(\mathbf{x}, t)$ is the local density of the mixture, such that $-1 \leq \Phi \leq 1$ (see figure 2.6). The contact line can be defined as the isoline where $\Phi = 0$ on the solid surface.

The Cahn-Hilliard model corresponds to a non-local free energy functional

| Fluid solution | $c$ (w/w) | $\rho$ (g/cm$^3$) | $\eta$ (mPa s) | $\sigma$ (mN/m) | $\theta_E$ (deg.) | $\theta_A$ (deg.) | $\theta_R$ (deg.) | $\Delta\theta$ (deg.) | substrate |
|---|---|---|---|---|---|---|---|---|---|
| water | | 0.997 | 0.89 | 72 | 71±2 | 87±2 | 66±3 | 21±5 | PMMA |
| ethanol in water | 9% | 0.98 | 1.35 | 52.4 | 63±3 | 79±3 | 62±3 | 17±6 | PMMA |
| ethanol in water | 17% | 0.97 | 1.83 | 48.8 | 57±3 | 72±1 | 50±3 | 22±4 | PMMA |
| isopropanol in water | 5% | 0.988 | 1.12 | 49.6 | 64±3 | 75±3 | 43±3 | 32±5 | PMMA |
| isopropanol in water | 10% | 0.981 | 1.41 | 40.4 | 61±2 | 71±3 | 34±3 | 37±5 | PMMA |
| glycerol in water | 60% | 1.15 | 9 | 67.2 | 69±1 | 78±1 | 67±3 | 11±4 | PMMA |
| glycerol in water | 80% | 1.2 | 47 | 65 | 70±1 | 79±2 | 67±2 | 12±4 | PMMA |
| water | | 0.997 | 0.89 | 72 | 115±2 | 118±2 | 69±2 | 49±4 | silanized PMMA |

**Table 2.1 :** Main parameters of the different aqueous solutions used in this study. The concentration $c$ is reported in w/w. Density, viscosity and surface tension are labelled with $\rho$, $\eta$ and $\sigma$ respectively. Static ($\theta_E$) and dynamic contact angles ($\theta_A$ and $\theta_R$) and contact angle hysteresis ($\Delta\theta$) refer to sessile droplets on the substrate listed in the last column.

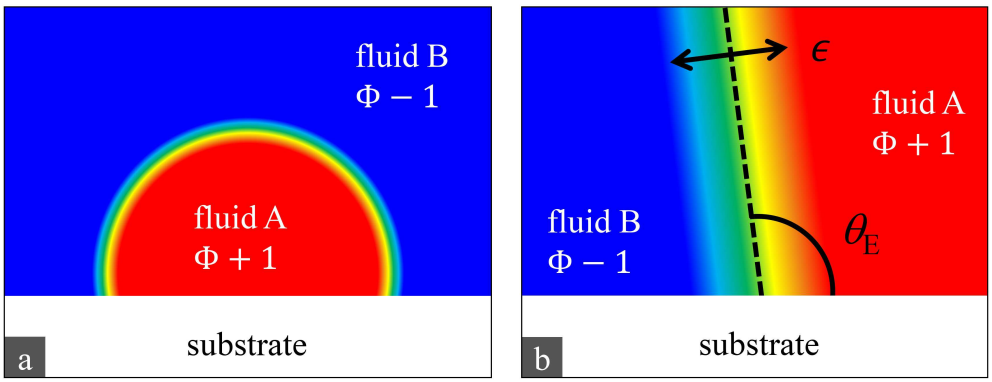


**Figure 2.6 :** 2D binary system constituted by two pure, immiscible fluids $A$ and $B$, described by the phase field $\Phi(\mathbf{x}, t)$ in the CHNS diffure interface model. (a) Sessile drop of fluid $A$ ($\Phi = +1$) surrounded by fluid $B$ ($\Phi = -1$). (b) Zoom of the diffuse interface, with thickness $\epsilon$, close to the triple point. The equilibrium contact angle $\theta_E$ is comprised between the solid surface and the isoline $\Phi = 0$.

$$\mathcal{F}[\Phi] = \int_\Omega \left( f_{bulk}(\Phi) + \frac{\lambda}{2}|\boldsymbol{\nabla}\Phi|^2 \right) dV + \int_{\partial\Omega} f_w(\Phi)\, dS\,, \tag{2.2}$$

where $\lambda = 3\sigma\epsilon/\sqrt{8}$ is a coefficient related to the fluid-fluid surface tension $\sigma$ and to the interface thickness $\epsilon$, combined with the constraint of mass conservation of the two species.

A common choice for the bulk free energy density is the double-well

$$f_{bulk} = \frac{\lambda(\Phi^2-1)^2}{4\epsilon^2} \tag{2.3}$$

with two minima in $\Phi = \pm 1$ (i.e. $\rho = \rho_A$ or $\rho = \rho_B$), which drives the system toward the segregation of the two species. Conversely, the gradient excess term $(\lambda/2)|\boldsymbol{\nabla}\Phi|^2$ energetically penalizes the formation of sharp interfaces. As a consequence of these two counteracting mechanisms, a finite thickness interface (width of order $\epsilon$), across which $\Phi$ varies smoothly, separates the two bulk fluids in such a way to minimize the interfacial energy. The presence of the wall modifies this equilibrium, as prescribed by the last term, which acconts for the fluid-wall interaction,

$$f_w(\Phi) = -\sigma\cos(\theta_E)\frac{\Phi(3-\Phi^2)}{4} + \frac{\sigma_{wA}+\sigma_{wB}}{2}, \tag{2.4}$$

with $\theta_E$ equilibrium contact angle (see figure 2.6b), $\sigma_{wA}$ and $\sigma_{wB}$ solid-fluid surface tensions. Because away from the contact line, i.e. in the portions of solid surface where $\Phi = \pm 1$, the interfacial energy density corresponds to the solid-fluid surface tensions $\sigma_{wA} = f_w(\Phi = +1)$ and $\sigma_{wB} = f_w(\Phi = -1)$, the definition of $f_w(\Phi)$ gives back the Young's law 1.7 $\sigma_{wB} - \sigma_{wA} = \sigma\cos(\theta_E)$

The model can be extended to unsteady isothermal conditions in presence of fluid motion described by the velocity field $\mathbf{u}$. Under the assumption of a small density variation, i.e. $2\,(\rho_A - \rho_B)\,/\,(\rho_A + \rho_B) \ll 1$, the velocity field is solenoidal to first order in the density variation, and the dimensionless form of the system reads

$$\boldsymbol{\nabla}\cdot\mathbf{u} = 0\,, \tag{2.5}$$

$$\frac{D\Phi}{Dt} = \frac{\mathrm{M}}{\mathrm{Cn}}\nabla^2\mu_c\,, \tag{2.6}$$

$$\frac{D\mathbf{u}}{Dt} = -\frac{1}{\rho}\boldsymbol{\nabla}p + \frac{1}{\mathrm{We}\,\mathrm{Cn}}\mu_c\boldsymbol{\nabla}\Phi + \frac{1}{\mathrm{Re}}\nabla^2\mathbf{u} + \frac{1}{\mathrm{Fr}}\,. \tag{2.7}$$

In equations 2.6 and 2.7 $\dfrac{D(\cdot)}{Dt} = \partial(\cdot)/\partial t + \mathbf{u}\cdot\boldsymbol{\nabla}(\cdot)$ is the material derivative, $\mathrm{M} = 3M^*\sigma/(sqrt8L^3f)$ is the dimensionless mobility coefficient where the mobility $M^*$ is related to the time needed by the two fluids to reach the equilibrium state inside the interface and $f$ is the oscillation frequency of the plane. $\mathrm{Cn} = \epsilon/L$ is the Cahn number, i.e. the ratio of interface thickness and macroscopic length scale $L$. The chemical potential $\mu_c$ is defined as the functional derivative of the free energy (2.2) with respect to the phase field, $\mu_c = \delta\mathcal{F}/\delta\Phi = \Phi^3 - \Phi - \mathrm{Cn}^2\nabla^2\Phi$. In equation 2.7, $p$ is the pressure, $\mathrm{Re} = \rho L^2 f/\eta$ is the Reynolds number with $\mu$ the viscosity, $\mathrm{We} = 3\rho f^2 L^3/(\sqrt{8}\sigma)$ is the Weber number, $\mathrm{Fr} = L\rho/(4\pi^2 A\Delta\rho)$ is the Froude number, $A$ the oscillation amplitude and $\Delta\rho = \rho_A - \rho_B$. In the

reference frame of the plane inclined by the angle $\alpha$, the vibration corresponds to a time dependent body force that gives rise to a buoyancy term. Assuming the peak acceleration of the vibrating plane much larger than the gravitational one, we can neglect the latter constan contribution. From the definition of $\Phi$, the density is expressed as $\rho = \rho_M + \Delta\rho/2$, with $\rho_M = (\rho_a + \rho_B)/2$ average density. For the sake of simplicity, we assume $\Delta\rho/\rho_M \ll 1$, so that, in the spirit of Boussinesq approximation, the only effect of buoyancy is retained in the body force

$$\mathbf{g}(t) = -\sin(2\pi t)(\sin(\alpha)\hat{\mathbf{e}}_{\mathbf{x}} + \cos(\alpha)\hat{\mathbf{e}}_{\mathbf{z}})\frac{\Phi}{2}, \tag{2.8}$$

with $\hat{\mathbf{e}}_{\mathbf{x},\mathbf{z}}$ the unit vectors in the two directions, parallel and perpendicular to the plane. At variance with the standard application of the Boussinesq approximantion, where the driving force is the temperature difference that leads to density variations via thermal expansion of the fluid, here the driving force is the phase field difference associated to the density contrast $\Delta\rho$.

In ordinary conditions the physical interface thickness is on the nanometer scale and the model cannot be exploited for macroscopic flows unless an artificial thickening of the interface is introduced. It is crucial that such artificial thickening does not alter the dynamics. Indeed the *sharp interface limit* is obtained when the macroscopic solution becomes independent of Cn and M at decreasing their values. In [127] the scaling law $\mathrm{M} \propto \mathrm{Cn}^2$ is shown to be crucial in approaching the physically meaningful solution in the limit of decreasing Cahn number, which is recovered at $\mathrm{Cn} = \mathcal{O}(10^{-2})$.

The system of equations is completed with the following boundary conditions:

$$\mathbf{u} = 0\,, \tag{2.9}$$

$$\boldsymbol{\nabla}\mu_c \cdot \mathbf{n} = 0\,, \tag{2.10}$$

implying the no-slip and no mass flux conditions at the wall, respectively, and

$$\frac{D\Phi}{Dt} = -\frac{\mathrm{Re}}{\mathrm{Dw}\,\mathrm{We}\,\mathrm{Cn}}\left(\Phi^2 - 1\right)\cos\theta_E - \frac{\mathrm{Re}}{\mathrm{Dw}\,\mathrm{We}}\frac{\partial\Phi}{\partial n}\,, \tag{2.11}$$

where $\mathrm{D_w} = \mu_f/\mu$, with $\mu_f$ an effective friction of the contact line, represents the ratio of the typical relaxation time in reaching the equilibrium contact angle to the macroscopic time scale [128]. Equation 2.11 represents the non-equilibrium boundary condition for the contact angle and links together the velocity of the contact line and the instantaneous contact angle [102].

In order to reach the sharp interface limit $\mathrm{Cn} = 0.025$ and $\mathrm{M} = \mathrm{Cn}^2 = 6.25 \times 10^{-4}$ has been used throughout the simulations. The equilibrium contact angle has been chosen slightly hydrophobic, $\theta_E = 97.5^\circ$ and, following [128], $D_w = 100$. The values chosen for density, viscosity and surface are the typical parameters for water reported in table 2.1. We considered a 1 mm radius drop and, in order to compare the numerical results with the experiments, we used $\Delta\rho/\rho = 1$ relying on the ability of the Boussinesq approximation to qualitatively reproduce the correct physics. More details about these simulations can be find in [102, 127].

## § 2.4. Experimental results

The motion of the drop is found to depend on the acceleration $a$ and on the frequency $f$ of the vertical vibrations. Figure 2.7 displays the dynamical phase diagrams of the five aqueous solutions obtained by scanning, at different constant frequencies, the vertical acceleration. To better compare them, the oscillating frequency is normalized [39] to the resonance frequency of the drops rocking mode corresponding to a supported drop vibrated in a direction parallel to the substrate [94], as we saw in subsection 1.8.2:

$$f_0 = \frac{1}{2\pi}\sqrt{\frac{\sigma}{\rho}\frac{6h(\theta_E)}{(1-\cos\theta_E)(2+\cos\theta_E)}}R^{-3/2} \tag{2.12}$$

where $R$ is the radius of the truncated spherical drop of volume $V$ and $h(\theta_E)$ is a dimensionless geometric function of the equilibrium contact angle $\theta_E$. For droplets on PMMA, $\theta_E$ is always less than 90° and then $h = 1$, while for water droplets on silanized PMMA $h(\theta_E{=}115°) = 0.4$. The radius $R$ can be calculated from [79]:

$$R^3 = \frac{3V}{\pi}\frac{1}{(1-\cos\theta_E)^2(2+\cos\theta_E)} \tag{2.13}$$

The acceleration is determined from the formula:

$$a = 4\pi^2 f^2 A \tag{2.14}$$

where $A$ is the oscillating amplitude, which is deduced from the maximum displacement of the ridge measured with the high frequency camera. The characteristic acceleration is taken as

$$a_0 = 4\pi^2 f_0^2 V^{1/3}. \tag{2.15}$$

For 2 $\mu$L water drops on PMMA, the two characteristic parameters are $f_0 = 70$ Hz and $a_0 = 241$ m/s$^2$, while on silanized PMMA $f_0 = 47$ Hz and $a_0 = 110$ m/s$^2$. For the other liquids on PMMA these values become smaller and are comprised in the ranges $f_0 = 34 - 59$ Hz and $a_0 = 59 - 173$ m/s$^2$. As can be evinced from the comparison with figure 2.1b, the phase diagrams of glycerol/water mixtures look quite similar to that originally reported for a drop of water-glycerol having $V = 5\mu$L and $\nu = 31$ mm$^2$/s deposited on an inclined plane with $\alpha = 45°$ [39] (the parabolic dashed lines in the diagrams of figure 2.7 represent the relative acceleration corresponding to the maximum peak-peak oscillating amplitude of our shaker equal to 2.5 mm). On the static ridge, the drops are always pinned to the surface. Vertically vibrating the ridge above a certain relative acceleration $a/a_0 \sim 0.2$, very similar to that found by Brunet *et al.* [39], yields sliding of the drop. Furthermore, sliding can be induced only for relative frequencies $f/f_0$ smaller than $\sim 1.5$, which is close to the cut-off of $\sim 1.3$ reported in figure 2.1b for a 5 $\mu$L glycerol/water drop for $\alpha = 45°$ [39]. At variance with previous experiments that could not detect sliding for drops of volume smaller than 5 $\mu$L [39, 110], we always observed a sliding region for all the 2 $\mu$L drops we investigated, an indication that our surfaces were not too defective. Also, no evidence of drop breaking was found during our measurements in contrast to what reported by Brunet et al. [39, 110], probably because of the smaller drops we used.

We now discuss in more detail the single phase diagrams, starting from that of pure water on PMMA that presents a pronounced sliding region at moderate accelerations: for $f/f_0$ =0.9 and $a/a_0$=0.4 the sliding velocity is about 6.4 mm/s. Further increasing the oscillating amplitude moves the drop upwards against gravity: for $f/f_0$ =1.1 and $a/a_0$=1.1 the climbing velocity is 4.3 mm/s. As expected, the overall phase diagram closely resembles those of mixtures of 9% (w/w) of ethanol in water and 5% (w/w) of isopropanol in water (not shown because it has fewer points) because these solutions have essentially the same viscosity and wetting properties of pure water. More interesting, it is also very similar to those of glycerol/water mixtures in spite of a variation in $\nu$ greater than a factor 10. This finding is consistent with the observation that the threshold for climbing with liquids of similar surface tensions does not depend on the liquid viscosity [110]. If instead we compare it with that of water on silanized PMMA, we notice that the sliding and climbing regions have been shifted to higher relative accelerations to balance the higher capillarity forces due to contact-angle hysteresis that, on silanized PMMA, is more than twice the value measured on PMMA, as reported in table 2.1. Arguably, the most interesting and original result of our experimental study is that drops of 17% (w/w) of ethanol in water and of 10% (w/w) of isopropanol in water do not climb within the $a/a_0$ range accessible to the experiment clearly indicating that a wettable ridge favors sliding only.

By means of the fast camera, we have analyzed the drop evolution during sliding and climbing with a sampling rate of 4 kHz. Figure 2.8 shows a sequence of side view snapshots taken over an oscillating period. They clearly show that the instantaneous drop profile varies differently in the two situations. The evolution of the climbing drop experiences a bigger variation in the profile: the peak becomes sharper (see E-D) and the bump is wider and shallower (see F-G).

From the analysis of these images, we have extracted the evolution of the upper and lower instantaneous contact angles, $\theta_{up}$ and $\theta_{down}$ respectively, which are shown in figure 2.9 for the two cases just discussed. In the same graphs, the corresponding positions of the contact points are also plotted. All quantities oscillate periodically over time. In particular, the positions display an oscillatory behaviour around a mean value that slowly moves downward (upward) when the drop slides (climbs). It is clearly evident that the lower (upper) contact point of a sliding drop moves downward when the corresponding contact angle is above (below) the advancing (receding) contact angle, as shown by the shaded areas in figure 2.9. Similarly, the upper (lower) contact point of a climbing drop moves upward when the corresponding contact angle is above (below) the advancing (receding) contact angle.

Furthermore, the contact angles, as well as the contact line positions, are out of phase with the oscillation of the inclined plate. The phase shift $\delta_{down}$ ($\delta_{up}$) between the lower (upper) contact point velocity and the lower (upper) contact angle for sliding and climbing drops driven at different frequencies are reported in figure 2.10. It results that the upper contact point velocity are always in phase with respect to the upper contact angle, while the lower contact point velocity is out of phase with the lower contact angle.

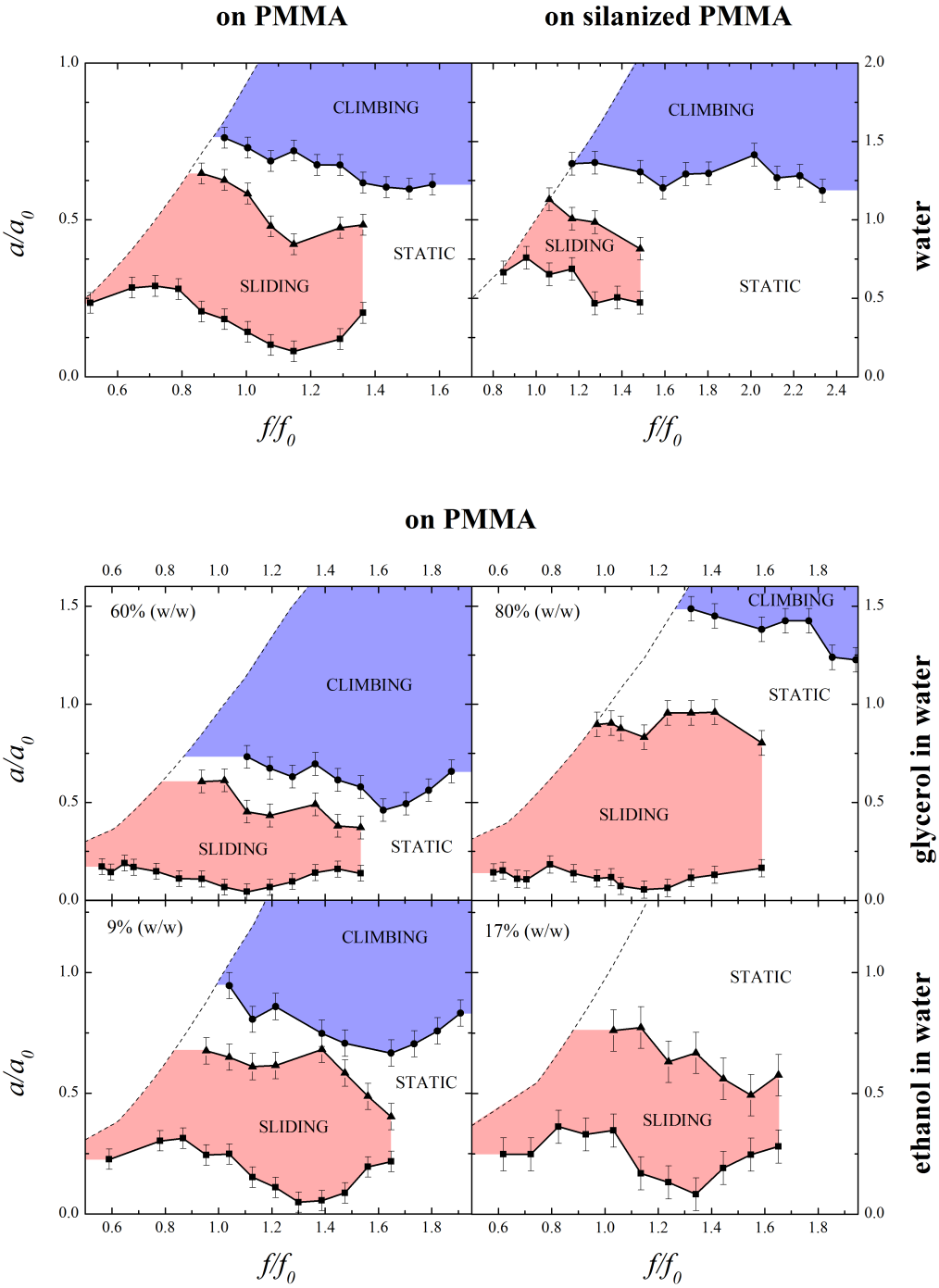


**Figure 2.7 :** Dynamical phase diagrams of drops of different aqueous solutions corresponding to $V = 2$ $\mu$L and $\alpha = 30°$. The normalization factors are $a_0 = 241$ m/s$^2$ and $f_0 = 70$ Hz for water on PMMA and $a_0 = 110$ m/s$^2$ and $f_0 = 47$ Hz for water on silanized PMMA. For the other liquids they are comprised in the ranges $a_0 = 117 - 173$ m/s$^2$ and $f_0 = 48 - 59$ Hz.

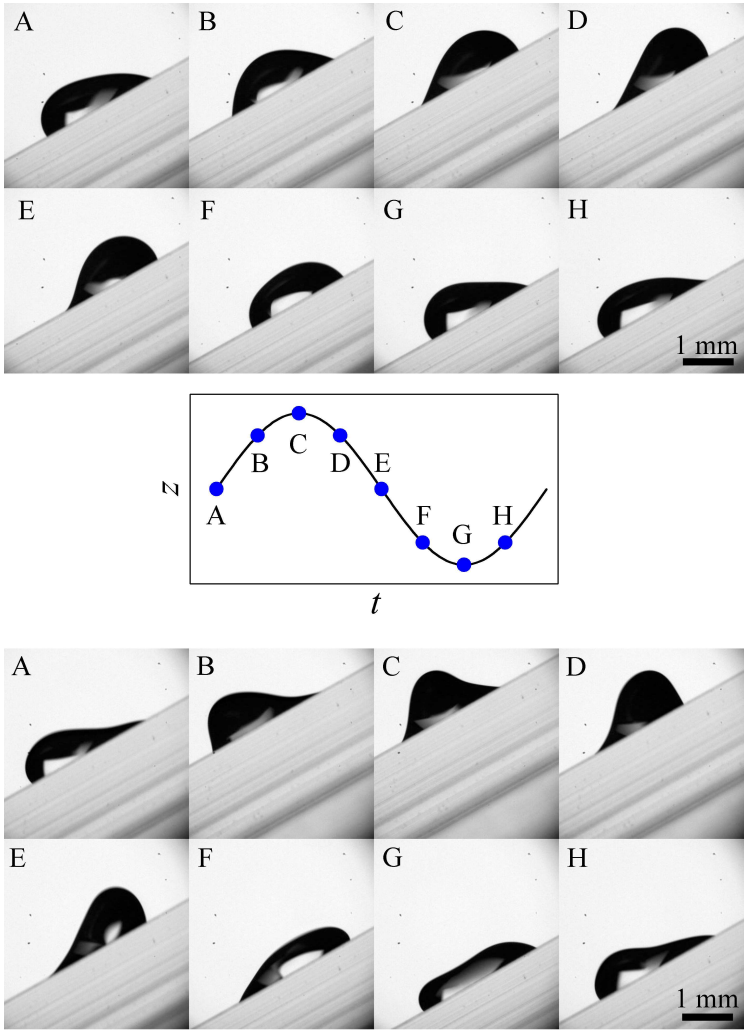


**Figure 2.8 :** Side views of a sliding (top) and climbing (bottom) water drop taken at different instants of a vibrating cycle of frequency $f$=65 Hz, e.g. $f/f_0 = 0.9$ for liding ($f$ = 80 Hz, e.g. $f/f_0 = 1.1$ for climbing) as indicated in the middle panel. The vertical accelerations are $a = 100$ m/s$^2$ ($a/a_0 = 0.4$) for the sliding drop and $a = 260$ m/s$^2$ ($a/a_0 = 1.1$) for the climbing drop.

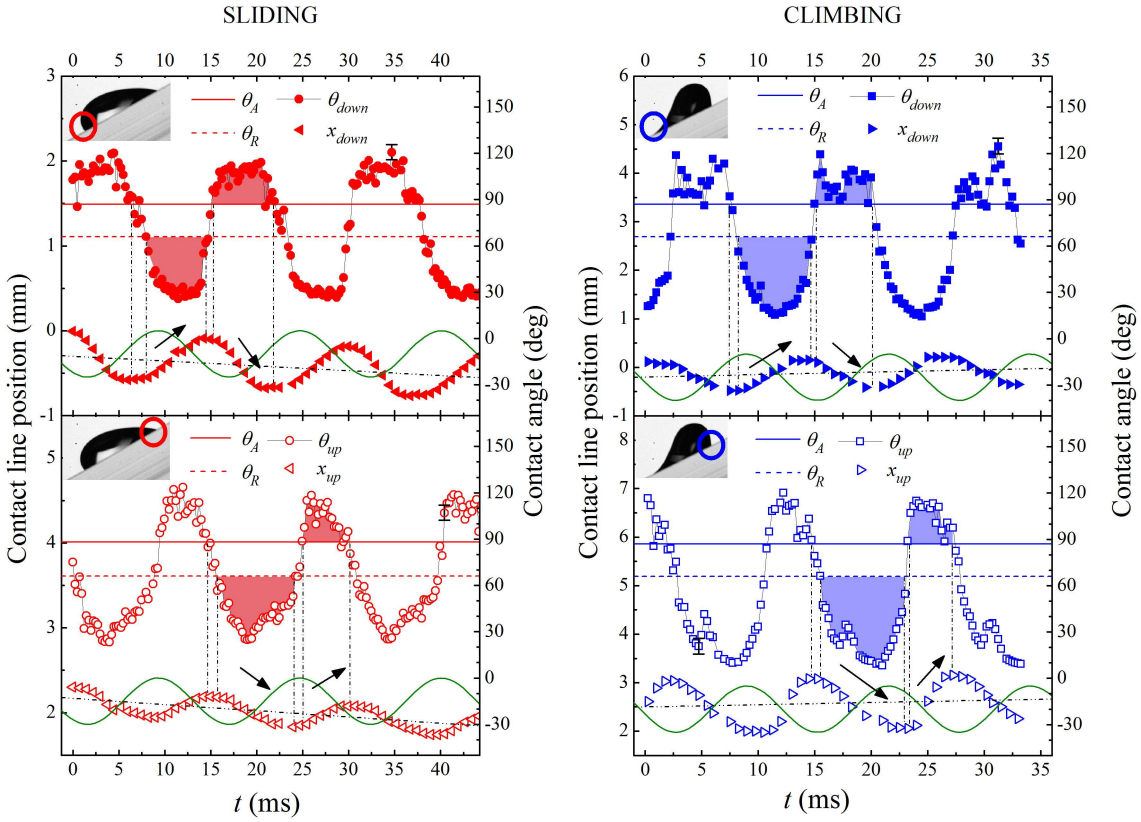


**Figure 2.9 :** Time evolution of the upper and lower contact angles for a water drop sliding down (left panels) and climbing up (right panels) the inclined ridge. The corresponding contact line positions along the $x$ direction of the inclined ridge are also plotted. Frequency and acceleration are $f = 65$ Hz and $a = 100$ m/s$^2$ for the sliding drop and $f = 80$ Hz and $a = 260$ m/s$^2$ for the climbing drop, respectively. The advancing (receding) contact angle is indicated by a continuous (dashed) horizontal line. The continuous sinusoidal lines represent the oscillation of the vertical position $z$ of the inclined plate (in arbitrary units). The error on the contact angle is about 5°. For the sake of clarity , the corresponding error bars are reported only in one point for each contact angle. Instead, the error bars on the position are smaller than the symbols.

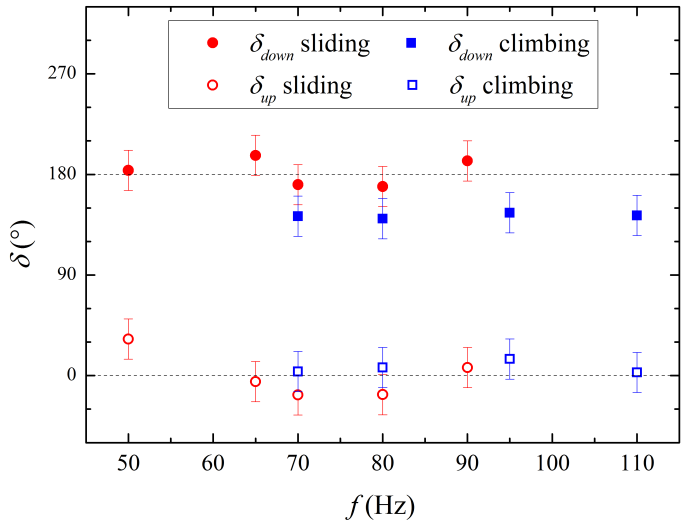


**Figure 2.10 :** Phase shift $\delta_{down}$ ($\delta_{up}$) between the lower (upper) contact point velocity and the lower (upper) contact angle for the sliding drop and the climbing drop. In the sliding case the peak acceleration is fixed at $a = 80$ m/s$^2$, while in the climbing one it is fixed at $a = 200$ m/s$^2$.

## § 2.5. Numerical results and comparison with experiments

Extensive numerical simulations have been performed by changing the frequency and the amplitude of the vibrating plate. Before discussing the results, we point out that several significant differences exist between the systems we have numerically simulated and the corresponding experiments:

(i) the simulations are two dimensional;

(ii) the two fluids (corresponding to droplet liquid and surrounding air, in the experiment) have the same viscosity and almost identical densities. More precisely, the Boussinesq approximation is adopted, which implies that the density is constant apart from the buoyancy term;

(iii) no pinning of the contact lines is considered;

(iv) the plate is hydrophobic ($\theta_E = 97.5°$).

Clearly, assumptions (i) and (ii) have been introduced for simplicity. Assumption (iii) is due to the lack of reliable models for pinning in the context of diffuse interface models. Finally, drop climbing has been found only by assuming iv). We cannot exclude that a more complete search could identify climbing also on slightly hydrophilic surfaces. Despite these differences, the dynamical phase diagram in figure 2.11 reproduces the main features observed in the experiments (see figure 2.7). At high acceleration the drop climbs. Reducing the oscillating amplitude at fixed frequency, a non-pinned static droplet is found. Because of the lack of pinning in the model, in this region the droplet periodically moves up and down without a mean displacement. Further decreasing $a/a_0$, the drop starts sliding. The numerical simulations cannot reproduce the static region found in the experiments at very low accelerations again because of the lack of pinning in the model. At very high accelerations, the drop detaches from the plane or, in some cases, breaks-up due to the extreme deformations. In the phase diagram in figure 2.11 the dashed curve identifies this breaking region. This sequence of dynamic transitions is found for all frequencies below a threshold value $\simeq 2f_0$, beyond which climbing disappears because the drop dynamics at high $a/a_0$ is dominated by detachment and break-up. This behaviour, not observed in our experiments, is likely due to the 2D nature of the drops since the reduced capillary stress (in 2D simulations the second main curvature is zero) leads to greater elongations that facilitate the drop break-up. Similarly, the numerical transitions are found at higher relative accelerations than the experimental ones. Notwithstanding these discrepancies, the overall qualitative behaviour is reproduced which means that neither the contact line pinning due to contact angle hysteresis, nor the density difference between the droplet and the ambient fluid, seems to be of crucial importance to describe the climbing mechanism.

The drop shape and the velocity field at different instants of the plate oscillating period are shown in figure 2.12 during both sliding and climbing. In agreement with the experiments (see figure 2.8), during sliding the drop undergoes smaller deformations: the border is more rounded and the maximum horizontal and vertical elongations are smaller. Furthermore the periodicity of the sliding drop is the same as that of the plate. Instead, the climbing drop shows a sub-harmonic response with twice the periodicity of the oscillating plate, which does not seem to be confirmed by the experiments and is

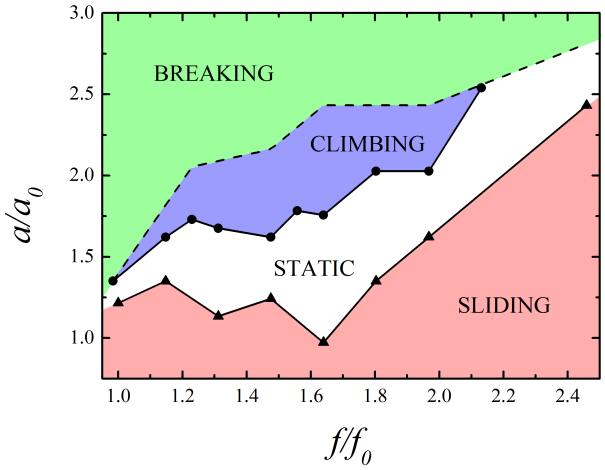


**Figure 2.11 :** Dynamical phase diagram of water obtained by numerical simulations. The data correspond to $\alpha = 30°$ and $\theta_E = 97.5°$. The normalization factors are $a_0$=185 m/s$^2$ and $f_0$=61 Hz.

probably related to the approximations introduced in the model (see Supplemental Material of [102] for a more complete discussion).

The time evolution of the contact line positions and of both upper and lower contact angles can be derived from the analysis of the droplet shape. Figure 2.13 compares the sliding (left panels) and the climbing (right panels) cases and the double period is again apparent in the upper front of the climbing drop. Full symbols correspond to the lower contact line, empty symbols to the upper contact line. As a reference, the vertical position of the plane is represented by a solid green line. In agreement with the experiments (see figure 2.9), the simulations of the sliding drop clearly show a phase shift of the contact line motion: when the plane goes up, the drop squeezes down and the lower contact line moves down while the other one goes up. The maximum tangential elongation is reached slightly before the plane reaches its maximum height. Overall, the capillary stresses act like a spring to restore the equilibrium shape. A similar dynamics is observed when the plane descends: the drop retracts and elongates vertically with the lower contact line moving up and the upper one going down. Again, the capillary stresses act against the strong deformation and the motion of the contact lines before the plane reaches its minimum height. The dynamic of the climbing drop is far more complicated as a result of the higher deformation experienced during the plate oscillation (see again the snapshots in figure 2.12). The phase shift is still present, but in the case shown in figure 2.13 it is not so pronounced. Moreover, the upper contact line stops sliding down during the plane descent, in a sort of dynamical pinning that enhances the climbing.

Beside the analysis of the drop shape, the numerical simulations provide details about the stress distribution. By numerically integration of equation 2.7 over the entire domain it is possible to extract the total force acting on the fluid. In particular the component in the $x$ direction (parallel to the wall) is (see [102] for more details)

$$F_{tot} = F_{visc} + F_{cap} + W, \tag{2.16}$$

where $W$ is the integral of the buoyancy force in the $x$ direction due to the plane vibration and $F_{visc}$ and $F_{cap}$ are the viscous and capillary forces, respectively. Figure 2.14 shows the time evolution of the

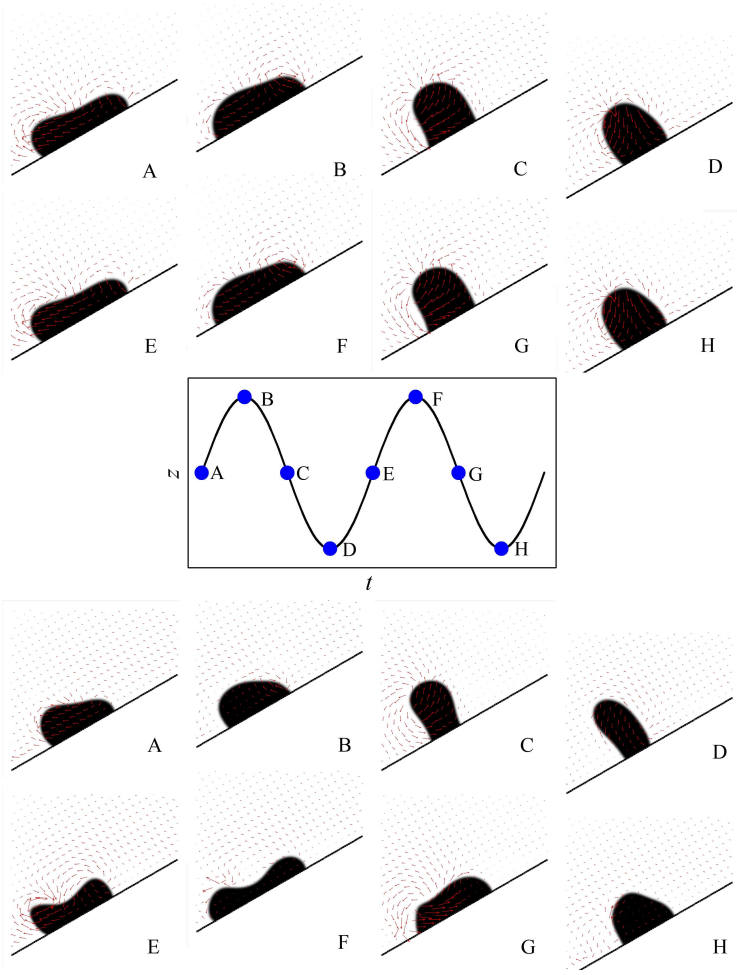


**Figure 2.12 :** Snapshots of a sliding (top) and climbing (bottom) 2D water drop taken at different instants of a vibrating cycle as indicated in the middle panel. The sliding drop corresponds to the case with $a/a_0 = 1$ and $f/f_0 = 1.33$, while the climbing drop to $a/a_0 = 1.9$ and $f/f_0 = 1.67$. The arrows represent the calculated velocity in both fluids.

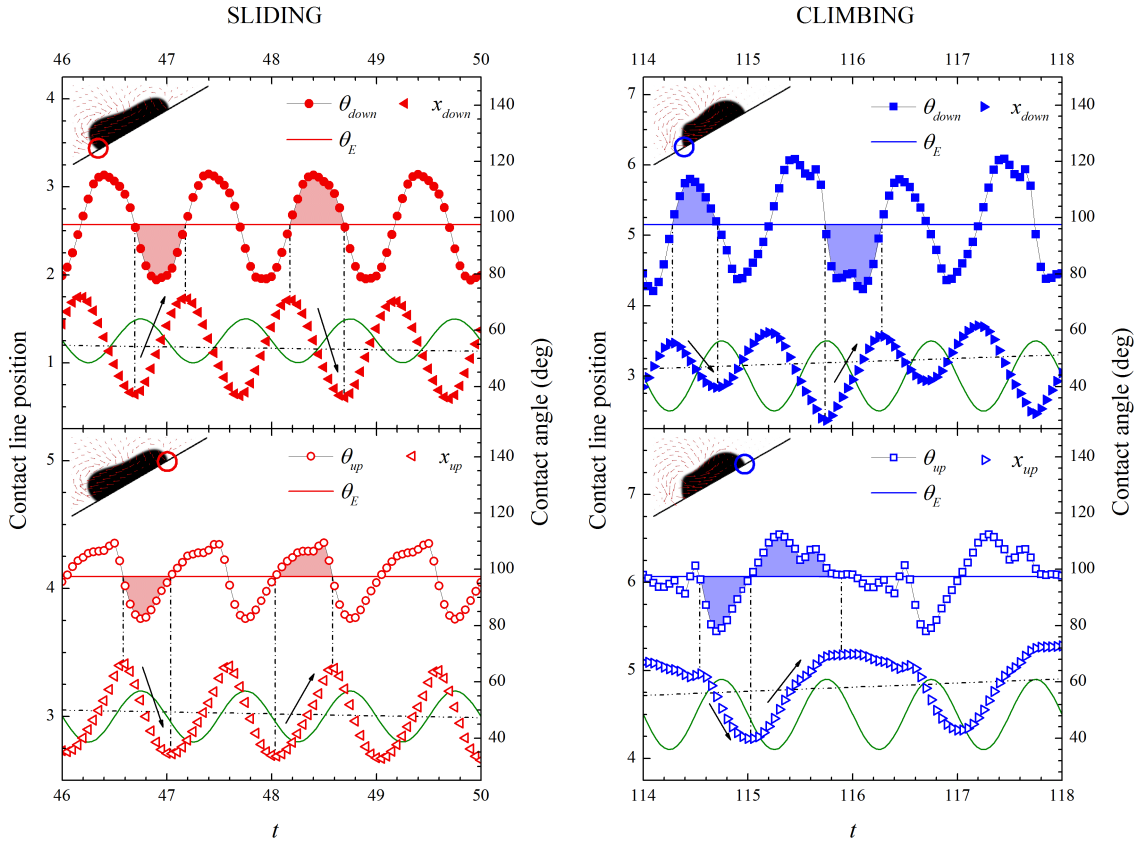


**Figure 2.13 :** Time evolution of the lower (full symbols) and upper (empty symbols) contact line positions (triangles) and of the contact angles (circles and squares) both in the sliding (left panels) and in the climbing (right panels) regime. The vertical position of the plane is indicated by a sinusoidal green solid line. The contact line position is expressed in unit of the resting drop radius (1 mm) and the time unit is the oscillation period.

viscous and capillary forces during two consecutive plate oscillations. The left panel refers to a sliding drop, the right one to a climbing drop. In both cases the two forces are not in phase with respect to the plate position. The time average of the resulting force equals zero since, on average, the motion is a steady sliding or climbing. The main difference between sliding or climbing is in the sign of the individual forces. We would like to remark that the mean viscous force always acts in the direction of the mean motion.

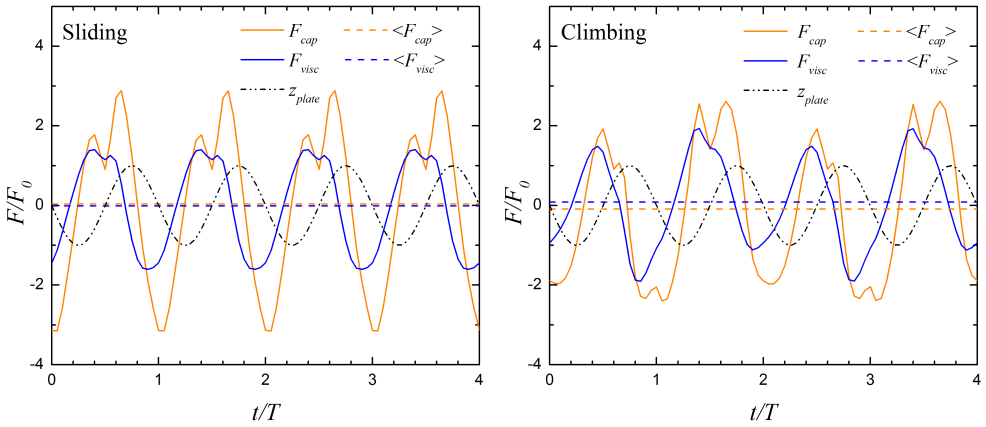


**Figure 2.14 :** Time evolution of the capillary and viscous forces acting on the drop. T is the period of the plane oscillation and $F_0$ is a reference force defined as $F_0 = \rho R^3/T^2$, with $\rho$ density of the liquid and $R$ radius of the drop. The left panel represents the sliding case, the right panel the climbing one. The vertical oscillation of the inclined plane $z_{plane}$ is represented in arbitrary unit.

This result suggests a possible mechanism for droplet motion: following the sketch in figure 2.15, a downhill-directed viscous force on the drop together with a mean motion in the same direction can be obtained by a circulatory motion of the fluid inside the drop. As a consequence, the droplet rolls down. On the contrary, when the drop climbs the plane, the circulatory motion reverts sign (up-hill rolling). To be more quantitative, we evaluated the mean circulation in the droplet interface by integrating the mean vorticity:

$$\langle \Gamma \rangle = \frac{1}{2T} \int_{2T} \oint_{\partial S} \mathbf{u} \cdot d\mathbf{l} = \frac{1}{2T} \int_{2T} \int_{S} \nabla \times \mathbf{u} dS dt \tag{2.17}$$

where the drop is identified as the region where $\Phi > 0$. All the sliding drops show positive values of $\langle \Gamma \rangle$ while climbing drops have $\langle \Gamma \rangle < 0$, confirming the conjectured rolling motion.

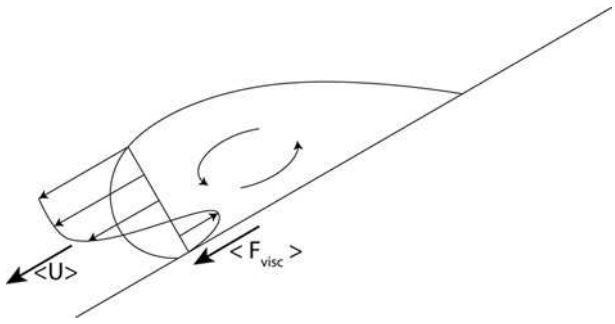


**Figure 2.15 :** Sketch of the rolling mean motion inside of a sliding droplet. Both the mean velocity and the mean viscous force are directed downhill.

## § 2.6. Conclusion

In conclusion, we have systematically studied the dynamics of liquid drops on an inclined plane subject to vertical vibrations. The liquids comprised distilled water and glycerol/water, ethanol/water and isopropanol/water solutions at different concentrations spanning the range 1-39 $mm^2/s$ in kinematic viscosity and 40 - 72 mN/m in surface tension. At sufficiently low oscillating amplitudes, the drops are always pinned to the surface. Vibrating the plate above a certain amplitude yields sliding of the drop. Further increasing the oscillating amplitude drives the drop upward against gravity. The viscosity of the liquid solution does not seem to affect significantly the dynamical phase diagrams, at least in the explored range 1-39 $mm^2/s$. Instead, low surface tensions, i.e. low contact angles, are found to hinder climbing and favor sliding of drops. Complementary numerical simulations of 2D drops based on a diffuse interface approach essentially confirm the experimental findings. The overall qualitative behaviour is reproduced suggesting that the contact line pinning due to contact angle hysteresis is not necessary to explain the drop climbing and that the direction of motion is related to the internal fluid circulation induced by plane oscillations. Images taken with a fast camera show that the drop profile evolves in a different way during sliding and climbing as also confirmed by the numerical simulation.

The exploitation of these effects offer the possibility to control and manipulate droplets on a substrate by tuning frequency and acceleration of the vertical vibration and drop volume. Because of the dependence of the dynamic behaviour of the drop on the volume and on the kind of fluid, drops with different size and/or composition subject to the same oscillation cane move in opposite directions up to meet and merge together (see Movie3 in supplemental material of [102]).

# Chapter 3

# Morphological Transitions of Droplets Confined on Rectangular Domains

In section 1.7 we introduced the morphological transitions occurring between different interfacial shapes of drops on patterned surfaces. This capillary phenomena allow a passive control on drop shape by chemically or geometrically modulating the substrate. An active control is possible too. Klingner and Mugele [14] showed it for the case of polar liquids by electrowetting on wettability patterns. In this chapter we demonstrate the possibility to control the shape of a drop confined on the top hydrophilic surface of a rectangular post by changing the liquid volume or by applying vertical vibrations to the substrate.

Section 3.1 introduces the morphological transitions occurring for water confined on rectangular domains. In section 3.2 we present the microfabrication procedures to realize the posts constituting the domains, while in section 3.3 we describe the experimental setup and procedure. Section 3.4 and 3.5 illustrate the transition between the two different morphologies characterizing the system, induced by volume variation and vibrations of the substrate, respectively. Finally, in section 3.6, we summarize the conclusions of this study.

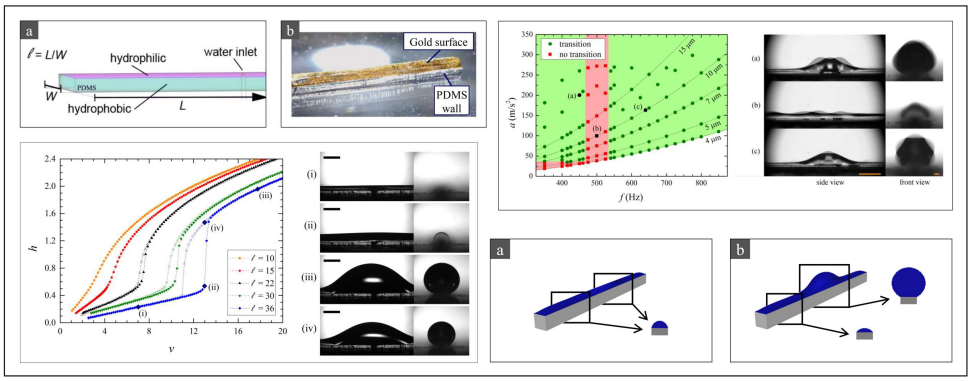

## § 3.1. Introduction

As we saw in section 1.7, interfacial morphologies and instabilities of liquid volumes on modulated substrates are subject to wide interest, from the point of view of both practical applications [11, 16] and fundamental study [12, 13, 129]. Below the capillary length interfacial phenomena are dominant and, in the context of Open Microfluidics, they can be exploited in order to passively control the formation, the shape and the motion of droplets by specific surface patterns.

Condensation experiments on hydrophilic stripes on hydrophobic substrate [12, 82] showed the transition between homogeneous liquid channels with circular segment cross-section and channels presenting a single bulge. The transition occurs when the liquid volume on the stripe reaches a value corresponding to the shape of maximum curvature, i.e. a half-cylinder. Similarly, as reported by Ferraro *et al.* [15], a water drop confined on a rectangular hydrophilic domain exhibits these two morphological states depending on the volume of the droplet $V$ and the aspect ratio $\ell$ (length to width ratio) of the rectangular domain. At variance with the previous experiments, in the latter the liquid volume $V$ on the domain has been controlled and measured and the dependence of the shape on $V$ has been studied. Increasing the volume lead to a transition between the homogeneous channel at small $V$ and the bulged channel at large $V$. This transition is continuous for small aspect ratios ($\ell < 16$) while for large aspect ratios ($\ell > 16$) it is a first order transition with a sharp discontinuity and a bistability volume interval where both the morphology are allowed.

We have retraced the experiment in [15], studying the morphological transition of water droplets confined on the top hydrophilic surface of a rectangular post induced by volume variations, and in addition we have focused on the behaviour of the interfacial morphology when perturbed by vertical vibrations of the substrate. In particular, we have considered the dependence on oscillation frequency and amplitude of the channel-to-bulge transition in the bistability region. The possibility of inducing the transition by vibrations allows an active control on the shape of the drops.

## § 3.2. Microfabrication of posts with hydrophilic and hydrophobic surfaces

The system we have studied consists in a water volume confined on rectangular domains by contact line pinning at the perimeter. In order to reach an as high as possible pinning, we have produced rectangular posts with hydrophilic top surface and hydrophobic lateral walls, exploiting both the difference in wettability and the geometrical edge. Given the need to vary the liquid volume on the post without perturbing the free air/liquid interface, water has been injected or extracted through a small inlet in the middle of the top face (see figure 3.1a). The rectangular posts, having various length $L$ between 5 and 18 mm and width $W = 0.5$ mm, have been realized by using a combination of photo- and soft-lithografic techniques. The post width $W$ was subject to two opposite requirements:

- $W$, taken as the characteristic length of the system, has to be smaller enough than the capillary length $\kappa^{-1}$ to safely neglect gravity;
- the post dimensions have to be large enough to allow an easy production of the water inlet.

Consequently, a post width of 0.5 mm was chosen. This value corresponds to a Bond number $Bo = 0.0341$ (calculated with $\rho = 1.0 \times 10^3$ kg/m$^3$ and $\sigma = 7.2 \times 10^{-2}$ N/m).

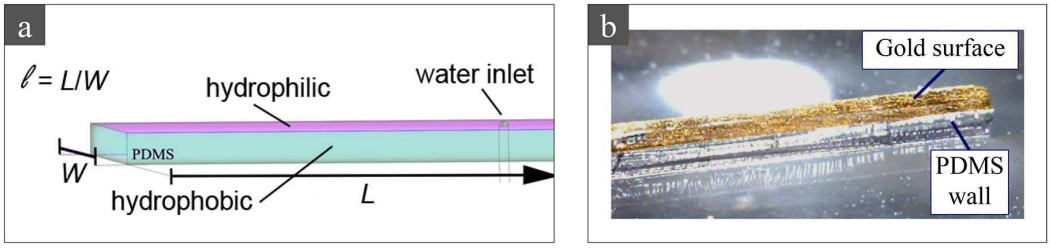


**Figure 3.1 :** (a)Sketch of a post with length $L$ and width $W$. The top surface is hydrophilic while the vertical walls are hydrophobic. (b) Picture of the final structure in PDMS and top surface covered by a layer of gold.

Master copies of the posts, with typical height of $150 - 200$ $\mu$m, were made by standard photolithography using SU-8 2050 negative photoresist (MicroChem Corp.) on silicon wafer (see figure 3.2) [130]. The details of the process are reported in appendix A. Positive copies of the master were produced by soft-lithography (see figure 3.3) [79, 131], in particular by a double replica molding procedure in poly(dimethilsiloxane) (PDMS) (Sylgard 184, Dow Corning), an elastomeric silicon-based organic polymer. In order to employ the silicon master as mold for PDMS, it was functionalized by evaporation with an anti-stick layer of trichloroperfluorooctylsilane. A first negative copy was cast by puring on the master a mixture of PDMS pre-polymer and curing agent and heating at 80° for 40 minutes. A thin teflon-coated steel wire, of diameter $\sim 150$ $\mu$m, was vertically inserted in the middle of the horizontal face of the negative post. The first negative PDMS copy was also silanized to be used as master. Then, a second PDMS replica was cast on the first one. The result was a positive PDMS replica of the original SU-8 master, with a thin channel opening in the middle of the top surface.

Since native PDMS is hydrophobic with contact angle $\approx 110°$ for water, the next step of the fabrication procedure was aimed to make exclusively the top surface of the post hydrophilic. A thin gold layer, $\approx 200$ nm thick, was evaporated on the post by magneto-sputtering (see figure 3.1b). To avoid metal deposition on the vertical walls, they were covered with NOA 61 (Norland Products), a UV-curable optical adhesive, taking particular care to cover the walls up to the edges and not the top surface. Right before starting each experiment, the gold surface was activated by UV/ozone cleaner (UVO-Cleaner 42, Jelight Company Inc.) and just then the NOA 61 coating was peeled off. After the treatment, the gold surface presented a contact angle of $\approx 15°$ for water, stable for a couple of hours. It is very important not to expose the vertical walls to the UVO-cleaner treatment, which would make PDMS hydrophilic [132] (see figure 3.4).

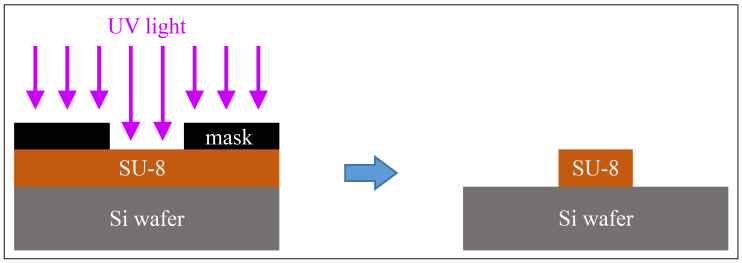


**Figure 3.2 :** Photolithographic fabrication of master copy of the post. (Left) A layer with the fequired thickness of uncross-linked SU-8 negative photoresist is deposited on silicon wafer by spin-coating and illuminated by UV light through a mask. (Right) The exposed portion of the SU-8 layer solidifies by UV light-induced cross-linking. After the removal of the uncross-linked photoresist, the final structure is obtained.

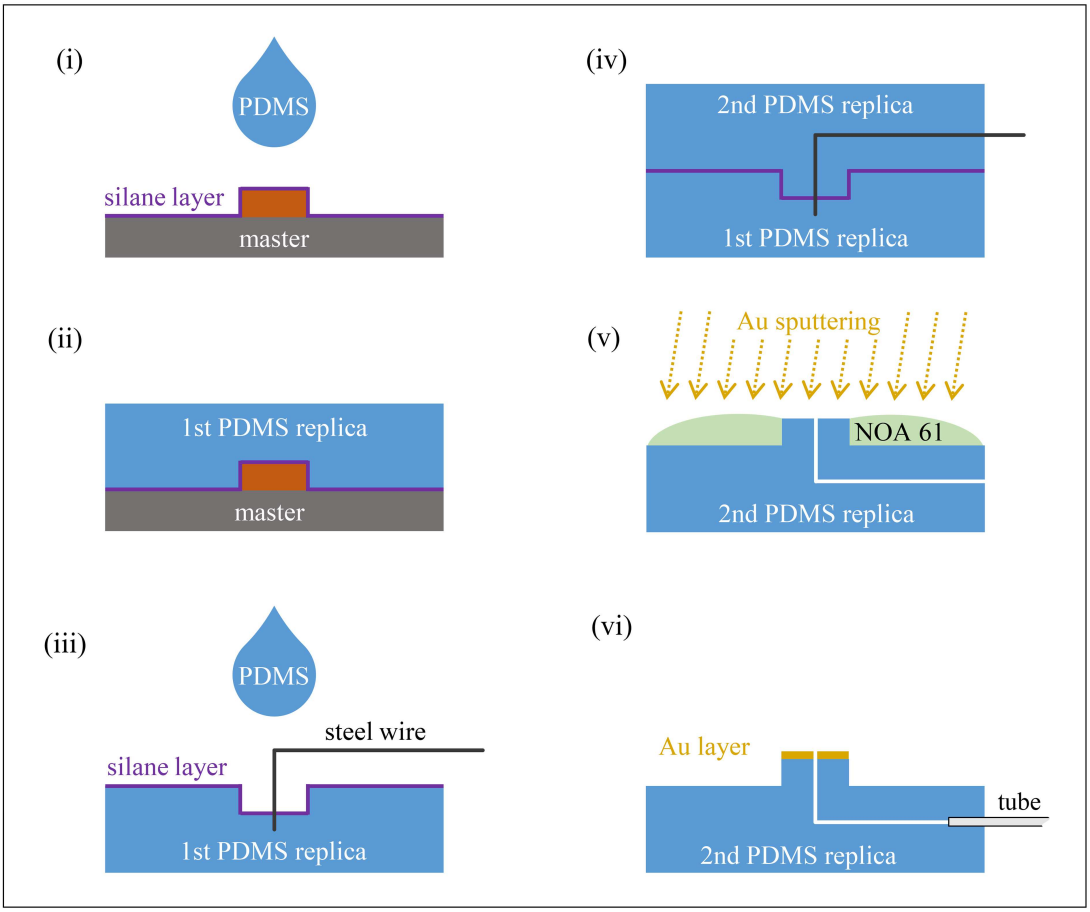


**Figure 3.3 :** Production of the post by double replica molding in PDMS of the master and gold deposition on the top surface of the post: (i) a mixture of PDMS pre-polymer and curing agent is poured on the master, coated with a fluorosilane anti-stick layer; (ii) a 1$^{st}$ negative PDMS replica is obtained by thermic curing at 80° for 40 minutes; (iii) the 1$^{st}$ replica, coated with a fluorosilane anti-stick layer and with the insertion of a $\sim$ 150 $\mu$m thick steel wire, is employed as master; (iv) a 2$^{nd}$ positive PDMS replica of the original master is obtained; (v) once the vertical walls of the post had been covered with NOA 61, a thin gold layer is evaporated on the top surface by magneto-sputtering; (vi) the final post with gold top surface and PDMS lateral walls features a water inlet conncted to silicon tubing.

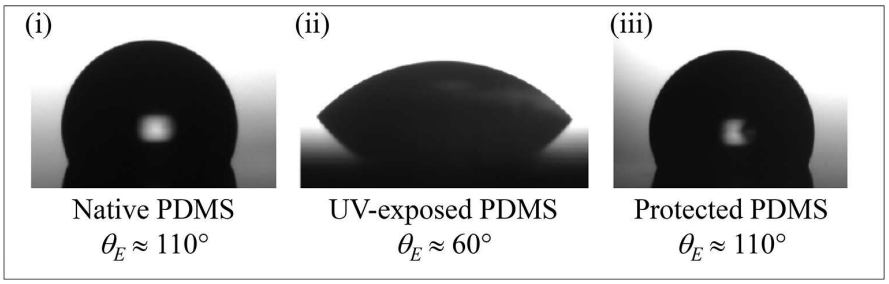


**Figure 3.4 :** Equilibrium contact angles for water drops on native PDMS (i), on PDMS exposed to UVO-cleaner treatment (ii) and on PDMS covered by NOA 61 and exposed to UVO-cleaner treatment (iii).

## § 3.3. Experimental details

Given the anisotropy of the interfacial morphologies of the drop confined on the rectangular domain, the drop profile has been simultaneously imaged along the two orthogonal symmetry axes (see figure 3.5) by the apparatus described in section 2.2. The central inlet of the post has been connected by a thin tube to a syringe-pump (PHD 22/2000, Harvard Apparatus) equipped with a 500 $\mu$L syringe (500F-LL-GT, Hamilton) in series with a flow-meter (FLOWELL, Fluigent) (see figure 3.6). This system allows the control and the accurate measure of the liquid volume on top of the post, which is an important improvement with respect to condensation experiments [12, 82].

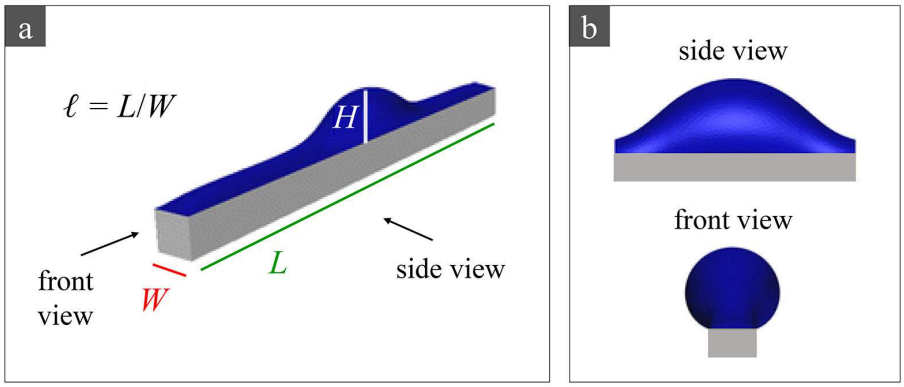


**Figure 3.5 :** (a) Sketch of the drop confined on the rectangular post with aspect ratio $\ell = L/W$. (b) Cartoon of front and side view profiles of the liquid interface.

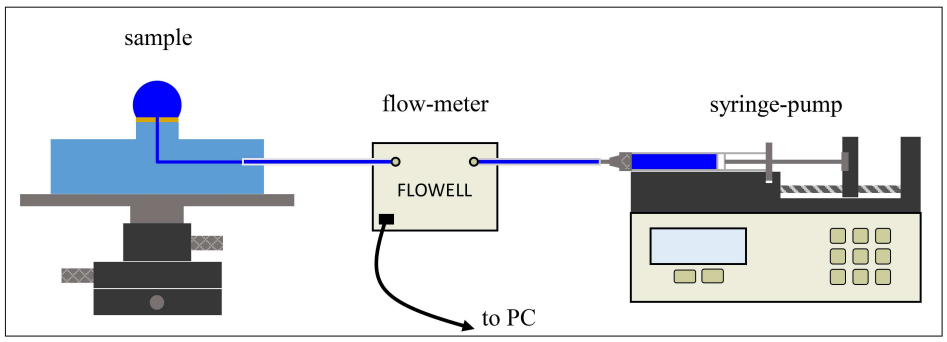


**Figure 3.6 :** Cartoon of the microfluidic system that allows to control and measure of the liquid volume confined on the post. The central inlet of the post has been connected by a thin tube to a syringe-pump equipped with 500 $\mu$L syringe in series with a flow-meter.

The experimental procedure consists in cycles of injection and extraction of distilled water on and from the rectangular domain. Starting from the spreading of a very thin layer on the whole domain we injected water until a maximum volume of $2 - 3$ $\mu$L and then we extracted it coming back to the thin layer. In the meanwhile we simultaneously acquired image sequences of the drop profile from both the orthogonal views and we measured the instantaneous volume on the domain. For each post, we repeated several cycles to achieve statistically robust results. We chose a flow-rate of 5 $\mu$L/min, that is sufficiently slow to not perturb the interface by inducing capillary waves. Since the repetition of several cycles at this flow-rate may last for a time of the order of ten minutes, water evaporation from the drop affected the volume measurement. In order to make evaporation negligible, we enclosed

the sample within a plexiglass box, whose interior featured several wet interfaces which manteined the air with a high humidity degree (see figure 3.7).

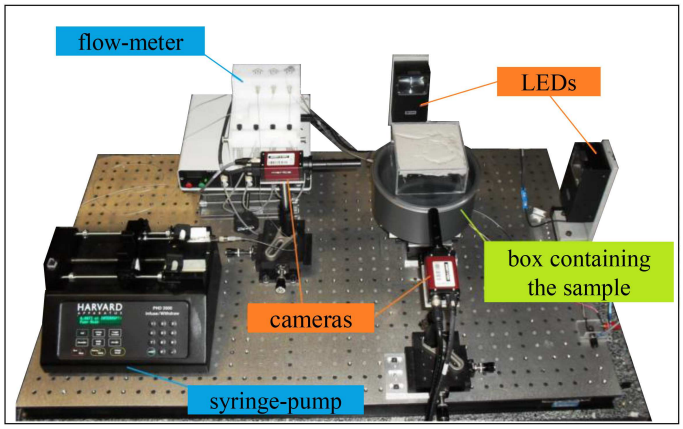


**Figure 3.7 :** Picture of the experimental setup. The sample is enclosed within the plexiglass box, whose interior features several wet interfaces keeping the air with an high humidity degree. The syringe-pump is connected to a flow-meter and can feed the drop from the inlet on the top surface of the post. The sample is imaged along two orthogonal lines of view.

The images was processed by means of an home-made program developed in IDL (Interactive Data Language) which can detect the profile of the liquid interface from the contrast difference between the dark drop and the bright background and evaluate the maximum height $H$ of the profile, with respect to the top surface of the post, for each image. The image sequence was synchronized with the volume time evolution measured by the flow-meter, so that the exact volume value was assigned to each profile, with an error of about 0.05 $\mu$L.

In order to apply vertical oscillation to the substrate, the sample has been mounted on the electromagnetic shaker described in section 2.2 (see figure 3.8). The oscillation amplitude was determined with an IR phototransistor that has been calibrated by optically measuring the net displacement of the shaker shaft. The resolution in amplitude was estimated to be $\approx 2$ $\mu$m. By means of a feedback circuit, it was also possible to sweep oscillation frequency maintaining constant amplitude (within the resolution) over a frequency interval of $\sim 500$ Hz. The system has been imaged by the high frame rate camera Phantom v7.3.

## § 3.4. Morphological transition induced by volume variation

In our experiments we have considered water confined on the top surface of rectangular posts with various aspect ratios $\ell = L/W$. For each, we observed the morphological transition between two interfacial shapes as the volume $V$ was changed:

- a homogeneous channel with almost uniform cross-section shaped as a circular segment, at small volume (see figure 3.9a),
- a channel with a central bulge, at large volume (see figure 3.9b),

in agreement with condensation experiments [12, 82] and with the study by Ferraro *et al.* [15].

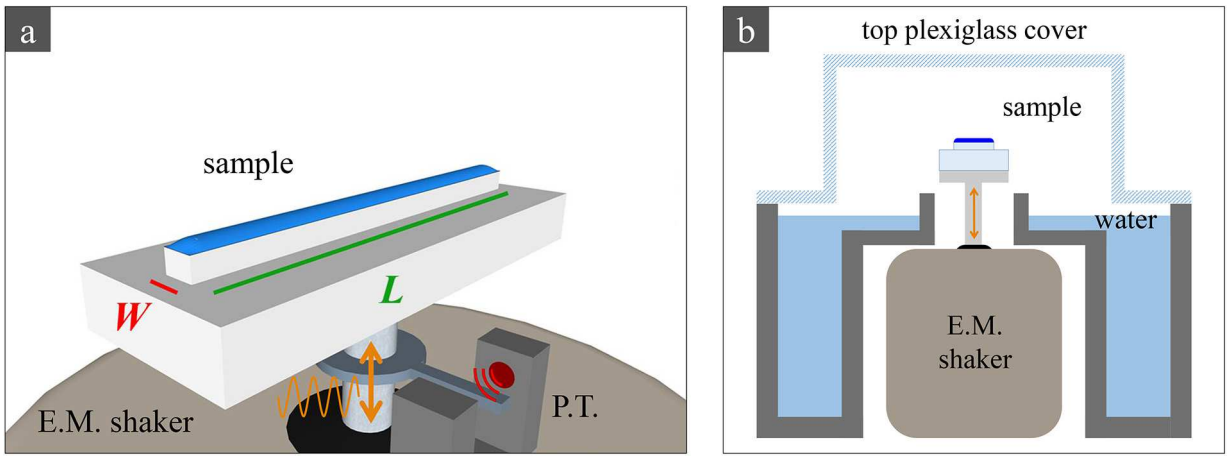


**Figure 3.8 :** (a) Cartoon of the sample mounted on the moving shaft of the electromagnetic shaker. The oscillation amplitude of the shaft is measured by a IR phototransistor (P.T.). (b) Sketch with the cross-section of the box enclosing the sample with the aim of prevent evaporation. A high humidity degree inside the box is maintained by free water interfaces.

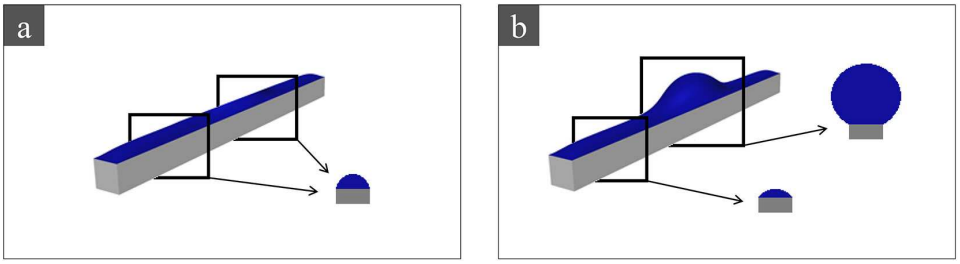


**Figure 3.9 :** Cartoons of the interfacial morphologies of water confined on the top surface of the post: (a) homogeneous channel with uniform cross-section shaped as a circular segment, for small volumes; (b) channel displaying a central bulge, for large volumes.

When water was pumped on the empty post, at first a thin liquid layer spread on the domain. At increasing volume, the interface assumed the shape of a homogeneous channel with almost uniform circular cross-section. It was different from a perfect cylindrical segment only in the terminal parts of the domain. For distances form the ends larger than $\sim W$ the cross section was uniform. Further increasing $V$, water tended to accumulate in the central part of the post and the interface started to form a central bulge, becoming larger and larger as the volume grew. The bulge formation involved a significant increase of the maximum heigh $H$ from the top surface of the post, as can be observed in right panel of figure 3.10. For this reason we chose the the maximum height $H$ of the liquid profile as order parameter to characterize quantitatively and distinguish the interfacial morphologies. We could also notice that as the bulge increased the tails became thinner.

Depending on the aspect ratio $\ell$ of the post, this transition could occur in different manners. For small aspect ratios, the system evolved from the homogeneous channel to the bulged channel with a smooth and continuous transition, while, for large aspect ratios, the evolution displayed a sharp transition. In the case of long domains, we observed that the transition from channel to bulge occurred when the pinned contact angle of the front view cross-section was approaching $\pi/2$ (see front view image (ii) in figure 3.10), corresponding to the maximum curvature of the liquid interface, i.e. the maximum Laplace pressure. This observation is in agreement with what happens for asymptotically long stripes ($\ell \to \infty$) [82].

In order to translate this qualitative observations into quantitative results, we have considered the variation of the reduced maximum height $h = H/W$ due to water reduced volume $v = V/W^3$ changes for several values of aspect ratios, $\ell = L/W = 10,\ 15,\ 22,\ 30,\ 36$. Reduced height $h$ as a function of reduced volume $v$ is reported in the plot of figure 3.10. We can observe that for small aspect ratio domains ($\ell = 10,\ 15$), there is a continuous cross-over between the homogeneous and the bulged channel with a smooth transition and it is not possible to clearly distinguish the two morphologies. In addition, the data points of $h(v)$ for increasing and decreasing $v$ lie on each other. Whereas, for large aspect ratio posts ($\ell = 22,\ 30,\ 36$), there is a clear distinction between the two morphologies and the passage from one to the other occurs with a sharp transition and a discontinuity in $h(v)$. Furthermore, the curves $h(v)$ for increasing and decreasing $v$ are different, displaying the opening of an hysteresis loop. For increasing $v$, the jump from homogeneous to bulged channel occurs when volume reaches the value $v_\uparrow$, while, for decreasing $v$, it occurs for a volume value $v_\downarrow < v_\uparrow$. For a volume $v$ comprised between $v_\downarrow$ and $v_\uparrow$ both the morphologies are stable and the system assumes one or the other depending if $v$ is reached from smaller or larger volume. The width of the hysteresis loop, $\Delta v = v_\uparrow - v_\downarrow$, becomes larger and the trasition sharper with increasing aspect ratio $\ell$.

This results compare well with numerical and experimental data presented in [15], in particular, they agree with the threshold aspect ratio $\ell^* \simeq 16$, above which $h(v)$ displays the hysteresis loop associated to the bistability volume interval $[v_\downarrow,\ v_\uparrow]$. Possible sources of discrepancies can be imperfections of the top surface of the post, in particular at the edges, due to fabrication defects, leading to a deviation of the contact line from the rectangular shape of the domain or to spilling of water along the vertical walls [79].

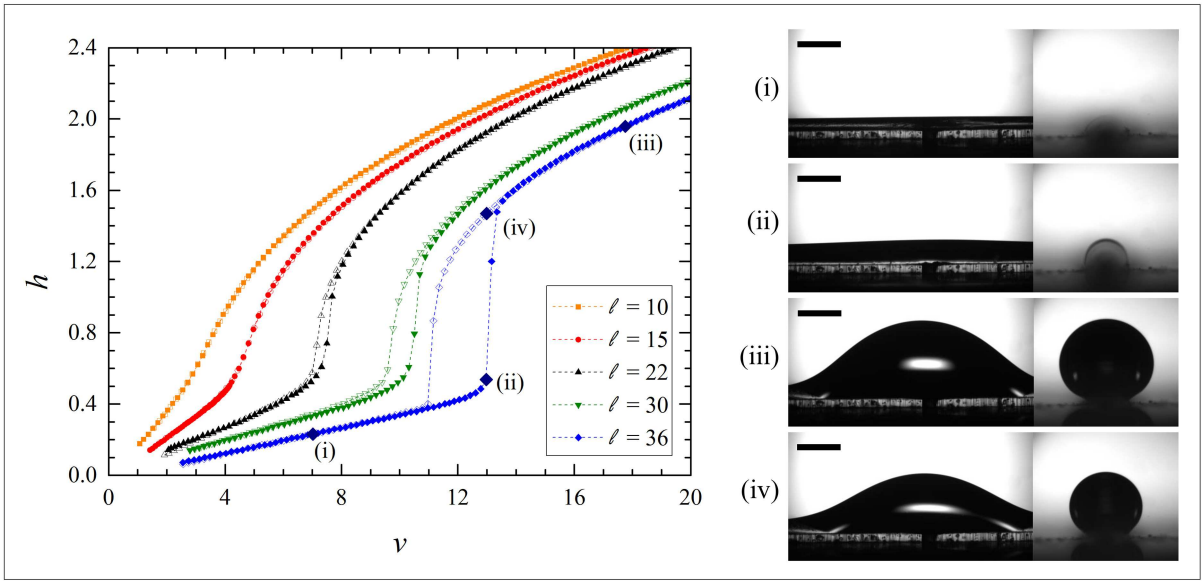


**Figure 3.10 :** Reduced height $h = H/W$ of the liquid interface on posts with various aspect ratios $\ell = L/W$ as a function of the reduced volume $v = V/W^3$. Full (empty) symbols represent data acquired during water injection (extraction). The points marked by bigger symbols correspond to the side and front view profiles reported on the right of the panel. The scale bars represent 0.5 mm.

## § 3.5. Morphological transition induced by substrate vibrations

The presence of a bistability volume interval for post with aspect ratio larger than $\ell^*$, where both the morphologies are allowed, suggests that for $v \in [v_\downarrow, v_\uparrow]$ the free energy as a function of $h$ presents two minima, to which a stable and a metastable state are associated. For small volumes the global minimum is the one at lower $h$, whereas for large volume it is the one at higher $h$, corresponding to the channel and the bulged morphology, respectively, similarly to the theoretical results found by Brinkmann and Lipowsky for the case of the striped domains in [83]. Consequently, for $v \in [v_\downarrow, v_\uparrow]$, we expected the possibility to induce the transition from the metastable to the stable morphology state by applying an external perturbation to overcome the free energy barrier. This perturbation can be constituted by capillary waves due to vertical oscillations of the substrate.

We considered the longest of our post, with $\ell = 36$, since it presented the widest bistability interval and the sharpest transition. Furthermore, we focused in the channel-to-bulge transition because, as can be seen in the plot of figure 3.10, it looks sharper than the opposite transition, making the individuation of $v_\uparrow$ easier with respect to $v_\downarrow$. Indeed, in the case of long posts, $v_\uparrow$ is characterized by a pinned contact angle at the long edge close to $\pi/2$, as observed from front view.

Water films with a volume corresponding to the upper limit $v_\uparrow$ of the bistability interval (around point (ii) of figure3.10) was then prepared on the post. With the film in the channel state, we turned on the vertical oscillations and recorded whether a transition to the bulge state is observed. We considered a frequency interval between 350 and 850 Hz. For frequency below 350 Hz, a sufficiently high accelerations were reached at large amplitude which made the apparatus mechanically unstable. On the other side, we did not exceed 850 Hz because the limited range of the feedback system. The dynamical phase diagram of figure 3.11 summarizes all the data taken. Each data point is the result

of at least ten complete runs taken in the same nominal conditions. Full green circles (red squares) indicate that at that acceleration and frequency a transition is (is not) found. The dashed parabolic lines represent the sweeps of the diagram taken at constant amplitude. To facilitate the reading of the diagram, the regions where the transition is admitted and prohibited are colored in green and red, respectively. The white region corresponds to oscillation amplitudes too small to be accurately measured ($A < 4$ $\mu$m). It is quite clear that between 460 and 530 Hz it is not possible to induce the transition to the bulge state up to the maximum acceleration achievable with our shaker. In addition, we observed an acceleration threshold for the transition at about 35 m/s$^2$. We point out that this transition is irreversible: once the film is in the bulge state, it cannot be driven back to the filament state by changing $A$ or even by turning off the shaker.

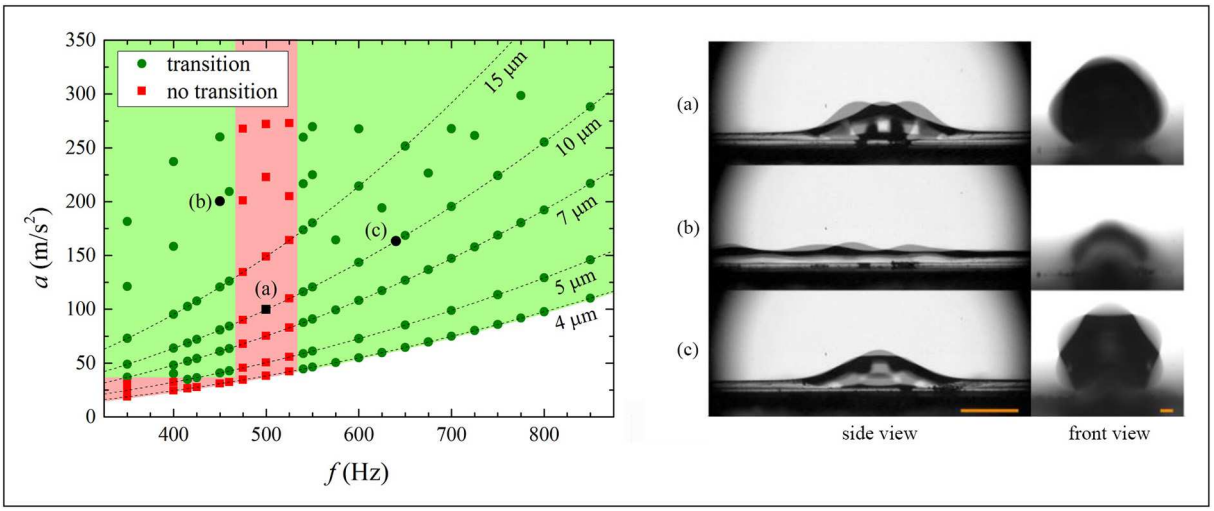


**Figure 3.11 :** (Left) Phase diagram of the transition from the homogeneous to the bulged channel induced by vertical vibrations of frequency $f$ and peak acceleration $a$. In the red region the system remains in the homogeneous channel state. Dashed lines indicate frequency sweeps of constant amplitude. The white region corresponds to oscillation amplitudes too small to be accurately measured. (Right) Side and front view images of the film profile, acquired with finite exposure time, taken at selected points in the phase diagram. For (a) and (c) the transition occurred and the system is in the bulge state. For (b) the system remains in the homogeneous channel state. The scale bars in the side view and in the front view correspond to 1 mm and 100 m, respectively.

To better understand the physical origin of this dynamical response, we took simultaneous lateral and frontal images of the liquid film. In particular, we observed that for a frequencies around 500 Hz, at which the transition did not occur, the channel morphology displayed a complex evolution of the water profile and the excitation of a longitudinal resonance, which was not seen at frequencies away from 500 Hz. This response to the vibrations is evident from side and front view images (b) in figure 3.11, due to a finite exposure time. We also show, as particular examples, the images corresponding to the selected points (a) at 450 Hz and (c) at 640 Hz of the phase diagram, in which the vibrations induced the transition and the final bulged morphology displayed longitudinal (side view) and transversal (front view) resonance modes, respectively. Figure 3.12 shows the time evolution of the front view profile during the transition from homogeneous to bulged channel corresponding to point (a) of the phase diagram of figure 3.11.

All these observations seem to indicate that the resonance mode of the channel state hinders the transition to the bulge state, whereas, away from this resonance, the oscillations of the liquid interface

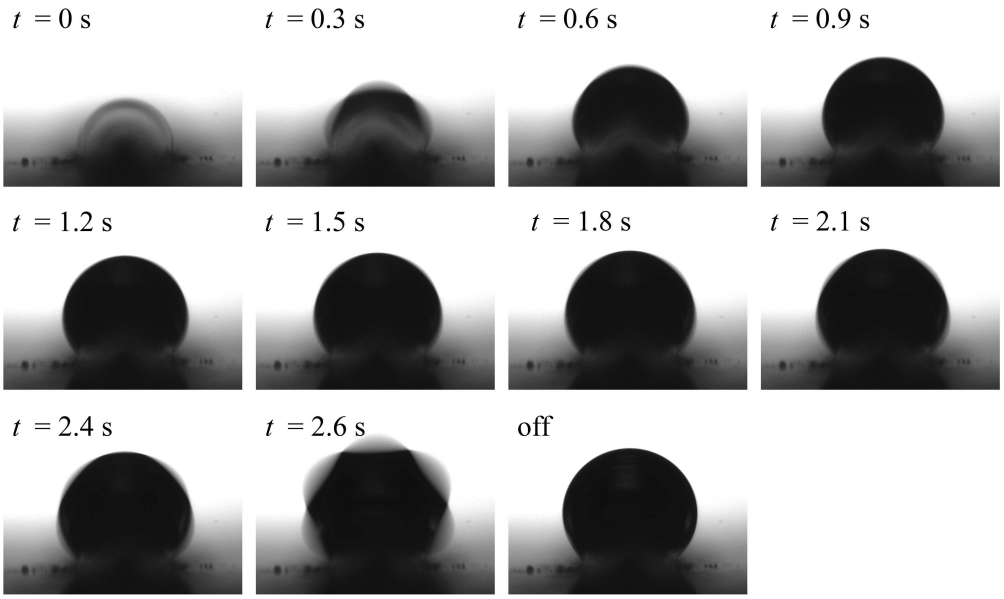


**Figure 3.12 :** Time evolution of the front view profile during the transition from homogeneous to bulged channel induced by vertical oscillation with frequency $f = 640$ Hz and acceleration $a = 160$ m/s$^2$. At time $t = 2.6$ s the interface reaches its final morphology which shows a resonant response to oscillations at 640 Hz. In the last image oscillations are turn off and the system remains in the bulged state.

induce the transition.

## § 3.6. Conclusions

In this chapter, we described the morphological transitions of water droplets confined of rectangular domains, with various aspect ratios $\ell$, induced by volume variation or by vertical oscillations of the substrate.

The rectangular domains consisted in the top hydophilic surface of rectangular posts with hydrophobic vertical walls. The posts were produced by photo and soft-lithographic techniques, starting from the realization of master copies which were replicated by a double replica molding procedure in PDMS. Then, a thin gold layer was deposited exclusively on the top surface of the posts in order to obtain hydrophilic domains. The liquid volume on the posts was changed by injecting/extracting water through a small inlet at the center of the top surface, without perturbing the liquid interface. A combination of syringe-pump and flow-meter allowed precise control and measure of the volume.

Depending on the liquid volume, we observed two different morphologies: a homogeneous channel with uniform circular cross-section and a channel with a central bulge, at small and large volumes, respectively. For short posts with aspect ratio $\ell = 10$, 15, smaller than the threshold $\ell^*$ found in [15], there was not a well defined separation between the two morphologies, but a continuous cross-over as the volume varied. On the other hand, for long posts with $\ell = 22$, 30, 36 $> \ell^*$, we found a clear distinction between the morphologies with a sharp and discontinuous transition for changing volume. Moreover, the transition was characterized by the opening of a hysteresis loop in the reduced height $h$ as a function of the reduce volume $v$, associated to a bistability volume interval.

In addition, given the bistability of the two morphological states for volumes in $[v_\downarrow, v_\uparrow]$ in the

case of long posts, we investigated the possibility that capillary waves on the interface could induce the transition at fixed volume. We applied vertical oscillations to our longest post ($\ell = 36$) with the system prepared in the channel state with volume corresponding to the upper limit of the bistability interval. Scanning oscillation frequency in the range between 350 and 850 Hz, we always observed the transition to the bulged channel except for frequencies around 500 Hz, at which the homogeneous channel displayed the excitation of a longitudinal resonance. This observation seems to indicate that the resonance mode of the channel state hinders the transition to the bulge state. Currently, a theoretical model explaining these intriguing experimental observations is still lacking.

# Part II

# Confined Bacterial Suspension

# Chapter 4

# Basic Concepts on Swimming Microorganisms

In this chapter we describe some basic concepts regarding the dynamics and the statistics of swimming microorganisms viewed as self-propelled particles. In section 4.1 we introduce the concept of active colloids applied to microswimmers. Section 4.2 deals with the Brownian motion characterizing passive colloids, while section 4.3 illustrates the hydrodynamic behaviour of microswimmers at low Reynolds number. Finally in section 4.4, we give an overview of the different motility patterns of bacteria.

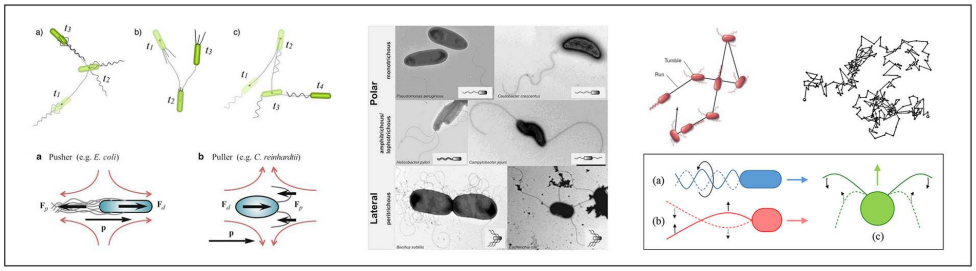

## § 4.1. Introduction to microswimmers

Many microorganisms (e.g., bacteria, algae) live in aqueous media and actively swim by assimilating energy from the environment [41, 133]. Due to micrometric size, their dynamics is characterized by both low Reynolds number hydrodynamics [43, 44, 134] and thermal fluctuations, so that they can be considered as a suspension of *active* colloids. With the term *active suspension* we define a large collection of particles with size in the colloidal range (from $\sim 1$ nm to $\sim 1$ $\mu$m) in liquid suspension that are capable to transduce chemical energy from the environment into mechanical work, in particular into movement resulting in self-propulsion [42, 46]. For this reason, such systems are intrinsically out of thermodynamic equilibrium, even without external driving [45].

Probably the most studied bacteria are the *Escherichia coli* and they can be taken as a paradigmatic example of active colloid. *E. coli* have a cylindrical-shaped body with lenght about 2 $\mu$m and diameter $\lesssim 1$ $\mu$m. The cell is propelled by several rotating helical flagella that push the cell body forward with speed of about $20 - 30$ $\mu$m/s [46, 48]. Many other different bacteria species are used in active colloid experiments, for instance *Vibrio alginolyticus*, *Pseudomonas aeruginosa* and *Calulobacter crescentus*, which have a very similar cell body with respect to *E. coli* but they are propelled by a single rotating polar flagellum. Another very popular self-propelled microorganism is the unicellular alga *Chlamydomonas reinhardtii*, although it is not strictly of colloidal size. Indeed, its body is roughly spherical with diameter of about 10 $\mu$m. The propulsion mechanism of this alga is based on two beating flexible flagella performing a sort of breaststroke pulling the cell body froward with speed average speed of about 100 $\mu$m/s [135, 136]. Finally, present technology allows the synthesis of artificial self-propelled particles. For instance Janus particles are polystyrene colloids with surface half coated with platinum and half with gold that become motile in aqueous solution of hydrogen peroxide because the two metals catalyze different chemical reactions at the two side resulting in a self-electrophoresis [137, 138].

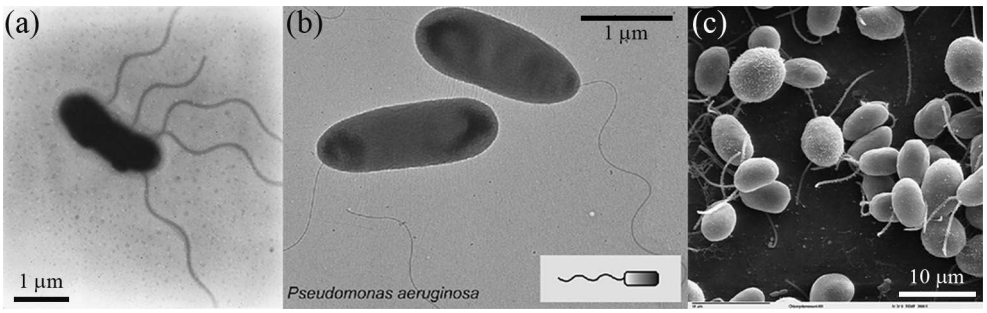


**Figure 4.1 :** Swimming unicellular microorganisms: negative-stained electron micrographs of (a) peritrichously flagellated *E. coli* [139] and (b) polar-flagellated *P. aeruginosa* [140]; (c) SEM image of *C. reinhardtii* algae (source: http://remf.dartmouth.edu/).

## § 4.2. Brownian particles

Before addressing the case of self-propelled colloids, we introduce the basic principle of diffusion characterizing colloidal particles. The colloidal nature is intimately linked to the concept of diffusion, being the definition itself based on Brownian motion: colloids are non-density-matched particles dispersed in a fluid, that remain suspended against gravity thanks to Brownian motion, i.e. erratic thermally driven motion due to the resultant of the forces exerted by each molecule of the surrounding fluid on the particle [46].

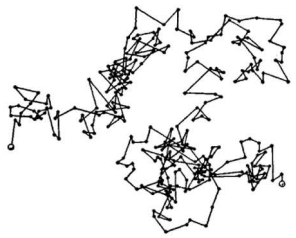

**Figure 4.2 :** Example of trajectory of a Brownian particle observed by Perrin [141].

A dilute particles suspension in thermodinamic equilibrium under the gravitational field is characterized by a number density $n$ as a function of height $z$ given by the exponential law [142]

$$n(z) = n(0)e^{-z/z_s}, \quad \text{with} \quad z_s = \frac{k_B T}{\Delta\rho V g} \tag{4.1}$$

where $z_s$ is called sedimentation height and $k_B$ is the Boltzmann's constant, $T$ the temperature expressed in K, $\Delta\rho$ the buoyant density, $V$ the particle volume and $g$ the gravitational acceleration. The definition of colloid provides a criterion to set the upper limit to the colloidal size range: particles of size $a$ are colloids if $a \lesssim z_0$. For a suspension of particles with typical densities of soft matter and at room temperature such limit corresponds to $a \lesssim 1$ $\mu$m.

Due to the randomness of the interaction between fluid molecules and the colloidal particle, Brownian motion is a stochastic process and, therefore, probabilistic and statistical quantities have to be introduced. One of the most relevant is the *mean square displacement*, that provides an average esteem of the amount of system explored by a particle during its migration. It is given by

$$\langle(\mathbf{x}(t) - \mathbf{x}(0))^2\rangle = 2dDt \tag{4.2}$$

where $\mathbf{x}$ is the position of the particle, $d$ is the dimensionality of the system and $D$ is the *diffusion coefficient* which represent the explored area per unit time.

A model for Brownian motion taking into account inertial effects was introduced by Langevin [143]. According to Newton's second law, the motion of a mesoscopic particle in a fluid is described by

$$m\frac{d\mathbf{v}}{dt} = \mathbf{F}_E + \mathbf{F}_T \tag{4.3}$$

where $\mathbf{v}$ is the particle velocity, $\mathbf{F}_E$ is the sum of the external forces (e.g. gravitational field, electric

field, etc.) and $\mathbf{F}_T = \sum_{i=1}^{N} \mathbf{F}_i$ is the sum of the forces $\mathbf{F}_i$ that each molecule of the surrounding fluid exerts on the particle. Since $N$ is of the order of the Avogadro's number, the solution of the full problem, corresponding to $N + 1$ coupled differential equations, is clearly impossible. Langevin's approach consists in decomposing $\mathbf{F}_t$ in two contributions:

- a deterministic damping term given by $-\alpha\mathbf{v}$ with $\alpha = 6\pi a\eta$ for a spherical particle in a fluid of viscosity $\eta$, in analogy with the Stokes law of the macroscopic hydrodynamics;
- a stochastic term $\mathbf{F}(t)$ representing the contributions of the collisions between molecules and particle. This term is supposed to have a Gaussian distribution with zero mean. Furthermore, since the collision time is much shorter than the characteristic time evolution of the particle motion, it can be supposed that $\mathbf{F}(t_1)$ and $\mathbf{F}(t_2)$ for $t_1 \neq t_2$ are independent random variables[†].

If no external force is present, equation 4.3 gives the Langevin's equation

$$m\frac{d\mathbf{v}}{dt} = -\alpha\mathbf{v} + \mathbf{F} \tag{4.4}$$

that is a stochastic differential equation. It can be solved by means of the Ornstein-Uhlenbeck's integration method [144], yielding, in the large time scale limit (diffusive regime) and assuming that the particle is in thermodynamic equilibrium with the fluid,

$$\langle(\mathbf{x}(t) - \mathbf{x}(0))^2\rangle = 2dDt, \quad \text{with} \quad D = \frac{k_B T}{\alpha} = \frac{k_B T}{6\pi a\eta}. \tag{4.5}$$

The expression for the diffusion coefficient $D$ is the Stokes-Einstein relation. For instance, the diffusion coefficient of a colloidal particle of size $\sim 1$ $\mu$m in water at room temperature is $\sim 0.1$ $\mu\text{m}^2/\text{s}$. This is more or less the case of non motile bacteria.

Besides translational diffusion, colloidal particles undergo also rotational diffusion, consisting in random reorientation of angle $\theta$. In analogy with the translational diffusion, the mean angular displacement around one axis is [145]

$$\langle(\theta(t) - \theta(0))^2\rangle = 2D_r t \tag{4.6}$$

where $D_r$ is rotational diffusion coefficient. For spherical particles of radius $a$ it is

$$D_{r,s} = \frac{k_B T}{8\pi a^3 \eta}. \tag{4.7}$$

For a sphere of radius $\sim 1$ $\mu$m in water at room temperature $D_{r,s} \sim 0.2$ $\text{s}^{-1}$. In the case of a prolate ellipsoid with semi-axes $a > b = c$, for rotations around the short axes, we have

$$D_{r,pe} = \frac{k_B T}{8\pi a^3 \eta} \times f(a/b), \tag{4.8}$$

where $f(c)$ is a geometric numerical factor [146].

We will see that in the case of the so-called smooth-swimming bacteria rotational diffusion has an important role.

[†]Formally, $\mathbf{F}(t)$ is supposed to be a $\delta$-correlated random force: $\langle\mathbf{F}(t_1)\mathbf{F}(t_2)\rangle \propto \delta(t_1 - t_2)$.

## § 4.3. Self-propelled colloids: swimming at low Reynolds number

Consider now colloids capable of self-propulsion, in particular swimming microorganisms (or *microswimmers*). We just saw that bacteria living in aqueous media can migrate by Brownian motion with a diffusion coefficient $D \sim 0.1\ \mu\text{m}^2/\text{s}$. This motion strategy is not successful, that is the reason why many microorganisms developped the ability of swimming with speed of the order of tens of $\mu$m/s. A comparison between the motion due to swimming and Browinan motion is given by the *Pecltet number*

$$Pe = \frac{advection}{diffusion} = \frac{UL}{D} \sim 10^2, \tag{4.9}$$

with $L \sim 1\ \mu$m and $U \sim 10\ \mu$m/2 the size and the speed of the bacterium, respectively. In order to evaluate the relative contributions of inertial and viscous effects in the dynamics of bacteria swimming in aqueous fluid at speed $U \sim 10\ \mu$m/s, we can look at the *Reynolds number*

$$Re = \frac{inertia}{viscosity} = \frac{\rho LU}{\eta} \sim 10^{-5} \tag{4.10}$$

with $\rho \sim 10^3$ kg/m$^3$ and $\eta \sim 10^{-3}$ Pa·s the density and the viscosity of the fluid, respectively. Typically, swimming microorganisms live at low Reynolds number ($Re \ll 1$) [134]. In such regime viscous effects are largely dominant over inertia. For comparison, the Reynolds number of a man swimming in a pool is $\sim 10^6$.

In general, the dynamics of a fluid (with density $\rho$ and Newtonian viscosity $\eta$) is described by the Navier-Stokes equation, that is basically the Newton's second law for a fluid element (per unit volume):

$$\rho\left(\frac{\partial \mathbf{v}}{\partial t} + \mathbf{v}\cdot\nabla\mathbf{v}\right) = -\nabla p + \eta\nabla^2\mathbf{v} + \mathbf{f}_E \tag{4.11}$$

where $\nabla p$ is the pressure ($p$) gradient, $\eta\nabla^2\mathbf{v}$ is the viscous stress and $\mathbf{f}_E$ is an external force per unit volume. Let us give a look at the magnitude order of the two inertial terms, being $U$ and $L$ the velocity and length scales of the system, respectively:

- the term $\rho\mathbf{v}\cdot\nabla\mathbf{v}$ scales as $\rho U^2/L$, whose ratio with the viscous term $\eta\nabla^2\mathbf{v} \sim \eta U/L^2$ gives the Reynolds number;
- the term $\rho(\partial\mathbf{v}/\partial t)$ scales as $\rho U/\tau$, with $\tau$ the characteristic time scale over which velocity changes. If we assume that $\tau$ is of the order of $L/U$, which constitutes the natural time of the flow, the ratio between this inertial term and the viscous one gives the Reynolds number too.

For $Re \ll 1$, both the inertial terms in equation 4.11 can be neglected and we obtain the Stokes equation

$$-\nabla p + \eta\nabla^2\mathbf{v} + \mathbf{f}_E = 0 \tag{4.12}$$

governing flow at low Reynolds number.

The lack of the inertial term, which means the absence of time derivative, results in an instantaneous response of the flow field to applied force. The dynamics at time $t$ is entirely determined by

the force exerted at $t$, with no influence of what happened before $t$[‡]. For instance, when a bacterium stops swimming it costs a distance of the order of 0.1 Å and it comes to rest after 1 $\mu$s [145] (actually the bacterium does not stop, because it is always subject to Brownian motion).

The properties of Stokes equation 4.12 have very important consequences:

- **Linearity.** Stokes equation is linear in the velocity $\mathbf{v}$. This property allows the superposition of elementary solutions to solve a particular problem.
- **Reversibility.** Given the time-independence of Stokes equation, changing $t$ to $-t$ does not modify the equation. If $\mathbf{v}(\mathbf{x})$ is a solution with associated pressure field $p(\mathbf{x})$, then $-\mathbf{v}(\mathbf{x})$ is a solution too with the external forces reversed and the reverse pressure gradient[§].

The reversibility propriety results in the Purcell's *scallop theorem* [43,134] that applies to swimming microorganisms: propulsion cannot be achieved by a sequence of body movements identical under time-reversal, i.e. by reciprocal movements, no matter the speed of the body movement. In order to keep swimming the microorganism has to deform its body cyclically. If the deformation is characterized by just one degree of freedom in the configuration space, the microorganism perform a reciprocating motion. This is the case of the scallop at $Re \ll 1$ that can only open and close its shell producing no net displacement.

Evolution solved the problem of propulsion by selecting swimming strategies based on non-reciprocal motion which consists in body shape deformations parametrized by more degrees of freedom or by just one degree that keeps increasing (see figure 4.3). The first is the case of eukaryotic cells swimming by means of flexible flagella (e.g. *C. Reinhardtii* or sperm cells), while the second is the case of bacteria that swimm by rotating rigid chiral helical flagella (e.g. *E. coli*, *P. aeruginosa*).

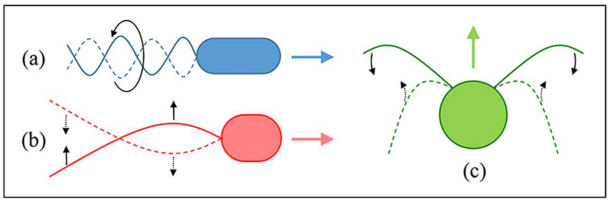


**Figure 4.3 :** Cartoons of non-reciprocal motions: (a) rotation of a rigid chiral helical flagellum of bacteria; (b) oscillation of the flexible flagellum of a sperm cell; (c) breaststroke-like movement of the two flexible flagella of *C. reinhardtii*.

Since microswimmers move autonomously, with no need of external force, the total force exerted by the swimmer on the fluid, and vice versa, is null: the propulsive thrust force $\mathbf{F}_p$ exerted by the flagella on the surrounding fluid, in the direction opposite to the swimming motion, is balanced by the equal and opposite viscous drag force $\mathbf{F}_d$ exerted by the cell body also on the fluid. This basic description of the forces exerted by the microswimmer suggests that the overall effect on the fluid can be modeled as that of a force dipole [147]. Depending on the relative positions of the application points of thrust and drag forces, we can have two different dipolar flow fields:

[‡]This is no more true in the case of visco-elastic fluids, because of the elastic storage of energy in the medium.

[§]A fascinating example is given by a famous experiment by G.I. Taylor. See *Low Reynolds Number Flows* at `http://web.mit.edu/hml/ncfmf.html`.

- if the flagella propell the cell body by *pushing* from behind (e.g. *E. coli* or sperm cells), the microswimmer (called *pusher*) repels fluid from the body along its axis and draws fluid in at the sides (see figure 4.4a);

- if the flagella propell the body by *pulling* from the front (e.g. *C. reinhardtii*), the microswimmer (called *puller*) draws fluid in along its axis and pulls fluid out from the sides (see figure 4.4b).

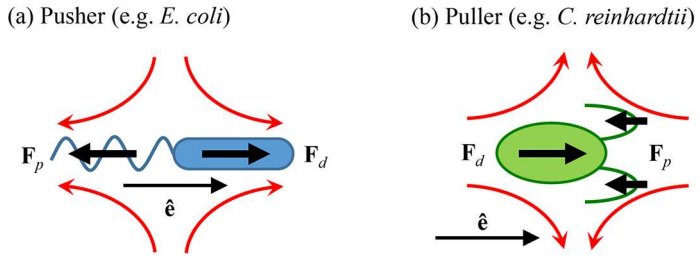


**Figure 4.4 :** Sketch of the flow field produced by pusher (a) or puller (b) microswimmers. The swimming direction is indicated with $\hat{\mathbf{e}}$, $\mathbf{F}_p$ and $\mathbf{F}_d$ are the propelling and the drag forces, respectively, and the red arrows show the direction of the induced fluid flow.

Mathematically, the force dipole is defined as $\mathbf{P} = F\,\mathbf{d}$, where $F = |\mathbf{F}_d| = |\mathbf{F}_p|$ and $\mathbf{d}$ is the relative position of application point of $\mathbf{F}_d$ with respect to that of $\mathbf{F}_p$, lying on the swimming direction of unit vector $\hat{\mathbf{e}}$. The dipole strenght $P = \mathbf{P} \cdot \hat{\mathbf{e}}$ can be either positive or negative, corresponding to a pusher or a puller microswimmer, respectively. The flow field induced at a distance $\mathbf{r}$ from the force dipole $\mathbf{P}$ is described by [147, 148]:

$$\mathbf{v}(\mathbf{r}) = \frac{P}{8\pi\eta r^3}\left[3\frac{(\mathbf{r}\cdot\hat{\mathbf{e}})^2}{r^2} - 1\right]\mathbf{r}. \tag{4.13}$$

## § 4.4. Swimming patterns of bacteria

As introduced in section 4.1, motile bacteria basically propelled themselves by the rotation of one or more rigid left-handed helical flagella. Despite there is not a great diversity on the shapes of cell body and of the flagellum, several different swimming strategies have evolved, selected by the particular environment where each species lives. The main source of this variety may be attributed to the number of flagella and on the location on the cell body as described by figure 4.5.

*E. coli* cell body is covered by four to eight peritrichous flagella [48], that can rotate either clockwise (CW) or counterclockwise (CCW) (viewed from behind the cell). Each of them is $7 - 8$ $\mu$m long, for a total cell length of about 10 $\mu$m [149]. The swimming pattern of wild-type strains can be described by a sequence of almost straight trajectories alternated with fast and random rotation of the cell (see figure 4.6a). The mechanism of such swimming pattern, referred as *Run and Tumble*, is the following: when flagella spin CCW they form a bundle that propels the cell forward in a nearly straight run with average speed of $20 - 30$ $\mu$m/s; when one or more flagella temporary switch to CW rotation the bundle separates and the cell changes orientation (tumble) before starting a new run [150].

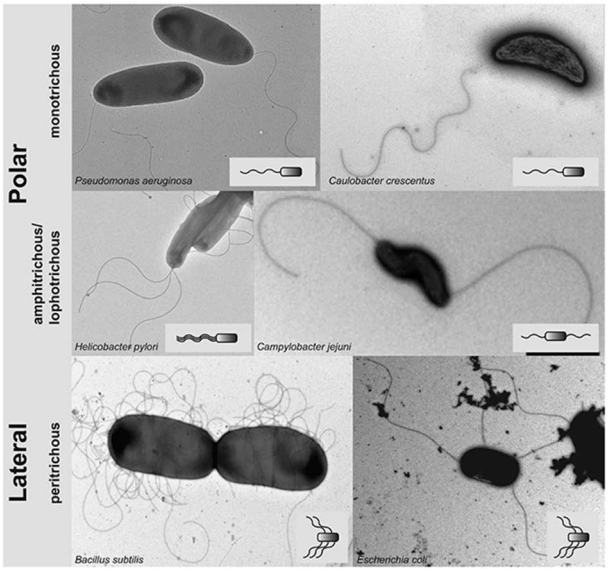


**Figure 4.5 :** Bacterial species vary in number and location of flagella. Negative-stained electron micrographs of monotrichous *P. aeruginosa* and *C. crescentus*, lophotrichous *H. pilori*, amphitrichous *C. jejuni* and peritrichous *B. subtilis* and *E. coli* [140].

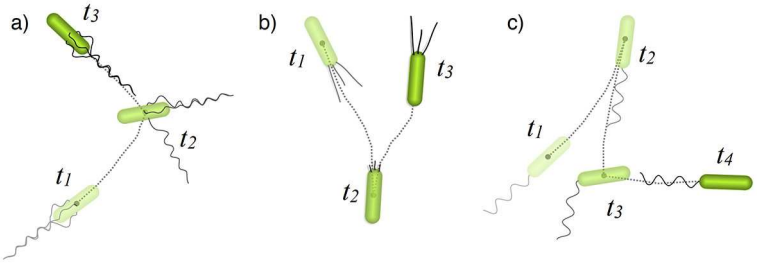


**Figure 4.6 :** Different swimming patterns: Run and Tumble (a), Run and Reverse (b) and Run-Reverse-Flick (c), characteristic of *E. coli*, *P. aeruginosa* and *V. alginolyticus*, respectively [151].

Typically the tumbling events occur with a frequency of about 1 Hz with duration ($\sim 0.1$ s) much shorter with respect to runs and average reorientation angle about 70°. A fully random reorientation would give an average angle of 90°, which means that its probability distribution is biased in the forward direction [145]. Conversely, the run duration follows a Poisson distribution, so that tumbles occurrence can be considered as a random event. Intuitively, we can understand that on a time scale much larger than the run duration the wild-type *E. coli* perform a three-dimensional random walk (see figure 4.7) with an effective diffusion coefficient that can be esteemed as

$$D_{eff} = \frac{v^2 \tau_r}{3} \sim 10^2 \mu \mathrm{m}^2/\mathrm{s}, \tag{4.14}$$

with $v$ the average speed and $\tau_r$ the average duration of the runs [45,145], that is $10^3$ times larger than the Brownian diffusion coefficient. It is clear that such "active" diffusion is much efficient in exploring and colonizing the environment with respect to Brownian motion.

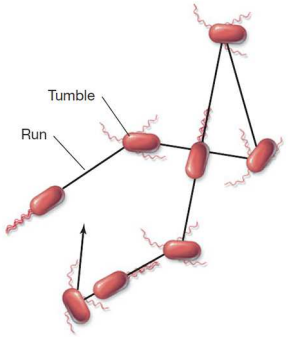


**Figure 4.7 :** Random walk resulting from Run and Tumble motion of wild-type *E.coli* [150].

A large variety of mutant strains of *E. coli* are available, characterized, for instance, by different swimming speed and tumbling frequency. Mutant strains lacking the tumble phase are referred as *smooth-swimmer* [48]. Despite for this kind of motility there is not an active reorientation mechanism, the cells still randomly change direction because of rotational diffusion.

The Run and Tumble pattern is common among peritrichously flagellated bacteria, beside *E. coli* we can mention *Salmonella typhimurium* and *Bacillus subtilis*.

On the other hand, there are monotrichous bacteria, e.g. *Pseudomonas* species, *Caulobacter crescentus* and *Vibrio alginolyticus*. They are propelled by a single polar flagellum that can spin either CCW or CW, pushing forward or pulling backward the cell body, respectively [152,153]. Therefore, differently from peritrichous bacteria that are pullers, monotrichous bacteria alternate puller and pusher behaviours. *P. aeruginosa* have been observed to spends equal time in both CCW and CW rotation phases. In addition, between the two phases, the flagellum briefly stops allowing an orientation change by rotational diffusion [154]. This motility pattern alternating forward and backward swimming is indicated as *Run and Reverse* (see figure 4.6b).

As further example, *V. alginolyticus* displays the *Run-Reverse-Flick* pattern, a variation of the Run and Reverse with an additional step called *flick*: after the foreward run and the $\sim 180°$ reverse, the flagellum develops a kink that produces an abrupt reorientation of about 90° (see figure 4.6c) [153,155].

# Chapter 5

# Bacteria of Different Motilities under Slit-like Confinement

In this chapter we report the results of a systematical investigation of the role of different swimming patterns in the concentration distribution of bacterial suspensions confined between two flat walls, considering wild-type *E. coli* and *P. aeruginosa*. In agreement with previous studies, an accumulation of motile bacteria close to the walls was observed. As original results, we found that the concentration profiles resulted to be independent on the walls separation and on the different kind of motility and to scale with the motile fraction. This results are confirmed by numerical simulations, based on a collection of self-propelled rod-like particles interacting only through steric interactions.

The numerical simulations here presented have been performed by Prof. E. Orlandini and Dr. A. Tiribocchi (University of Padova, Dept. of Physics and Astronomy "G. Galilei" - DFA), while Dr. P. Brun (University of Padova, Dept. of Molecular Medicine - DMM) has helped us in the preparation of microbiological samples.

After introducing the issue of active suspensions under confinement in section 5.1, we describe the material and the methods employed, in particular the preparation of motile bacterial suspensions (section 5.2), the experimental setup (section 5.3) and the theoretical model together with the numerical method (5.4). In section 5.5 we present and discuss the results of our experiments jointly with the numerical simulations and in section 5.6 we report the conclusions of our analysis.

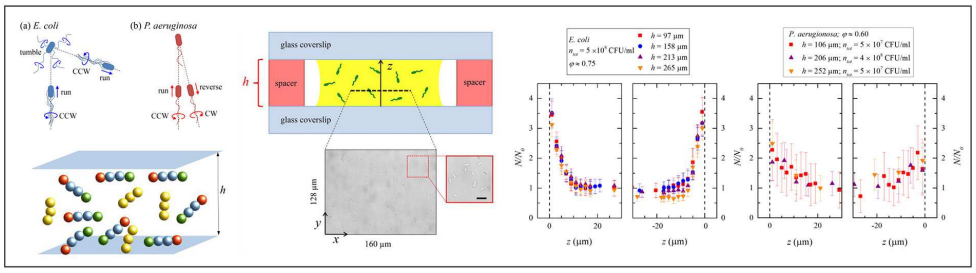

## § 5.1. Introduction

The motility behaviour near surfaces is of particular interest since very often bacteria can be found in geometrically confined environments (e.g., wet soil interstices, host living tissues, filters) [156]. The presence of surfaces and interfaces can alter bacterial motility and spatial distribution as consequence of both low Reynolds number hydrodynamics interactions and statistical effects arising from the non-equilibrium nature of these systems [45, 53, 147, 157].

For instance, *E. coli* bacteria are observed to swim in circular trajectories close to liquid-solid [50,51] or liquid-air interfaces [52] respectively in clockwise (CW) or counterclockwise (CCW) direction (seen from inside the liquid), as consequence of hydrodynamic interaction with the surface. Since the microswimmer is force and torque free, the CCW spinning of flagella induces a CW rotation of the cell body. A solid surface, associated to no-slip bounday condition, produces an increasing drag of the fluid comprised between the wall and the bacterium, resulting in a net torque rotating the cell direction to the right. Conversely, a free interface is associated to slip boundary condition that reduce the drag of the fluid between the interface and the swimmer. Therefore an opposite torque arises, making the cell direction rotate to the left [148].

In this chapter we focus on the phenomenon of accumulation of swimming microorgansims close to a solid surface, an effect that has been observed and studied by many authors since the '60s [55–60] but for which there is not still a general consensus on the possible mechanisms. In particular it is still under debate to which extent the bacteria density profile in proximity of the wall depends either on hyrodynamic interactions due to the dipolar flow field of pushers [56, 60] or by a combination of self-propulsion, steric collisions with the wall and rotational diffusion [57, 58]. A possible source of complexity is the wide variety of bacteria used in experiments, each with its own size, shape and motion mechanism that can give rise to measurable differences in bacteria accumulation at the walls [59].

Argubly, the most common bacteria used in experiments of microswimmers motility near surfaces is the *E. coli* [50–52, 56, 59, 60]. As described in section 4.4, the motion of the wild-type strains of *E. coli* is characterized by the Run and Tumble pattern, alternating straight trajectories and fast erratic reorientation events [149, 153, 158] (see Fig. 5.3a). For this bacteria the interplay between the random reorientation of the tumbling mechanism and the rectifying action of the surface is not yet completely understood [57, 59, 159], expecially if compared with its most studied mutant counterpart where the Run and Tumble mechanism is replaced by a smoother swimming motion [56–58, 60, 160]. Another swimming pattern is the Run and Reverse of wild-type *P. aeruginosa* that perform a back and forth motion [153, 161] (see Fig. 5.3b).

Although different swimming patterns and cell shapes can impact differently on the accumulation properties of bacteria near surfaces, to our knowledge no experimental work addresses this point sistematically and within the same investigational framework.

In this chapter, we present a joint experimental and computational study on the tendency of bacteria with different swimming pattern to aggregate in proximity of rigid walls. Experiments are performed on bacterial suspensions of wild-type motility (WTM) *E. coli* and *P. aeruginosa*, i.e. microswimmers that display a Run and Tumble and Run and Reverse motion, respectively. The experimental measurements of the density profile of the suspension across the confining region are compared with

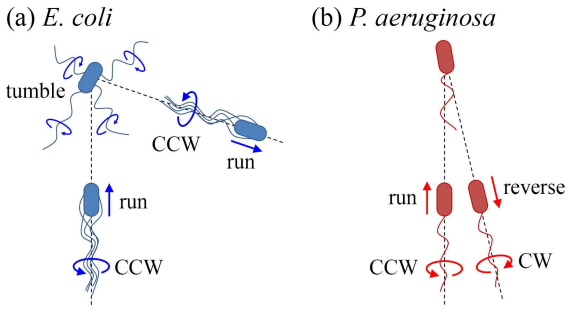


**Figure 5.1 :** Swimming patterns of wild-type bacteria: (a) *Run and Tumble* of *E. coli*; (b) *Run and Reverse* of *P. aeruginosa*.

the results of simulations based on a simple model of self-propelled based on just few physical properties such as the cell anisotropy, the cell-cell and wall-cell steric interactions and the roto-translational Brownian motion of each cell due to thermal fluctuations. Being very simple and generic, the model can be easily adapted to describe different motion mechanism and, specifically, self-propelled cells performing Run and Tumble and Run and Reverse motion. The agreement between the experimental findings and the simulation results demonstrate the reliability of the model in reproducing the cell aggregation in the proximity of the walls, a property that we further exploit to predict denisty profiles in situations that are barely accessible to experiments.

## § 5.2. Microbiological samples preparation

The preparation protocol adopted is in some extent based on the one specifically developed by Schwarz-Linek and collaborators [162] in order to obtain *E. coli* suitable for active colloid experiments. Indeed, generally, motility is not very high in the ranking of bacteria features in most part of microbiology laboratories.

Our samples consist of suspensions of WTM *E. coli* strain MG1655 (LGC Standards; Milan, Italy) or wild-type *P. aeruginosa* (isolated from a clinical specimen at the Microbiology and Virology Section, University Hospital of Padua, and identified by mass spectrometry). *E. coli* MG1655 strain has an insertion element in the genomic region regulating the transcription of flagellar genes encoding four or more flagella and making this strain hypermotile compare to the wild-type strains [163]. *E. coli* is grown at 30°C, shaken at 150 rpm in Lysogeny broth (1% Bacto-tryptone, 1% sodium chloride, 0.5% Yeast extract pH 7.5). The overnight bacterial cultures are then diluted 1:100 in 40 mL of Tryptone broth (TB; Becton Dickinson; Milan, Italy) containing 1% tryptone, 0.5% NaCl and grown at 30°C, shaken at 150 rpm until an optical density[§] $OD_{600} = 0.4$ is reached, corresponding to a middle-log phase. It has been demonstrated [162] that transferring *E. coli* cultures form Lysogeny broth to Tryptone broth results in higher average swimming speed. *P. aeruginosa* is grown and diluted at the same, using only Lysogeny broth. Bacterial cells are then harvested from culture media

[§]Bulk concentration of a bacterial suspension can be esteemed from the optical density (OD), i.e. the light absorbance $A_\lambda$, measured by means of a spectro-photometer on the basis of the Lamber-Beer law, $I/I_0 = e^{-\alpha_\lambda l} = e^{-A_\lambda}$, with $I$ and $I_0$ the transmitted and the incident light intensities, respectively, $\alpha_\lambda$ the absorption coefficient and $l$ the thickness of the suspension. Tipically, this kind of measure is performed at wavelength $\lambda = 600$ nm.

by centrifugation (2200 rpm, 5 min) and washed in prewarmed motility buffer (10 mM $K_2HPO_4$; 0.1 mM Na-EDTA, pH 7.0; 70 mM NaCl; 0.002% Tween 20). This process was repeated twice to achieve growth medium depletion and a suitable final bacterial concentration $n_{tot}$, expressed as colony forming unit (CFU)/ml and calculated from optical density ($OD_{600}$) measurement.

Due to the long time required to perform our experiments, the sedimentation of cells may become relevant. In order to prevent this problem, the suspensions are diluted 1 : 1 (vol/vol) with Percoll, a suspension of silica particles of $15-30$ nm diameter (23% w/w in water) coated with polyvinylpyrrolidone (PVP), to match cells and medium buoyant densities [164, 165]. A few microliters drop of bacterial suspension is closed between two glass coverslips separated by spacers of various thickness ranging between about 100 $\mu$m and 250 $\mu$m. The coverslips are previously cleaned in ethanol, dried by blowing nitrogn gas and dipped overnight in a 1% (w/w) Bovine Serum Albumin (BSA, Sigma; Milan, Italy) in water solution. The resulting BSA coating minimizes bacterial adhesion on glass surfaces due to electrostatic interactions with cell's membrane [166, 167].

At the end of each measurement, bacterial suspensions are aseptically diluted in warm PBS (Phosphate Buffer Saline), plated on Lysogeny agar plates and incubated at 37°C for at least 16 hrs to confirm bacterial vitality and load.

## § 5.3. Experimental setup and imaging

The sample is imaged in bright field by an inverted optical microscope (Nikon Eclipse Ti-E) with 100× magnification (Olympus LUMPlanFL 100×, water immersion, NA = 1, w.d. 1 mm, depth of field $\approx 2$ $\mu$m) and equipped with a C-MOS camera (Mikrotron EoSens MC1362). We observe a $160 \times 128$ $\mu m^2$ area of the sample on planes $(x, y)$ parallel to the glass walls (see figure5.2). The separation $h$ between top and bottom walls (in the $z$ direction) is scanned every 2 $\mu$m within 20 $\mu$m from the walls and every 10 $\mu$m in the central region, staring form the bottom wall up to the top wall. For each step we acquire a 50 s time-lapse movie at 2 fps, corresponding to 100 frames. The acquired images are analysed by a custom made routine, which recognizes objects in the field of view based on contrast difference with the background, in order to count the number of bacteria for each given $z$ plane. More precisely we estimate $N_{tot}(z)$, that is the total number of bacteria found at a given $z$ values averaged over 100 frames. Note that, among the whole set of bacteria some of them are non motile. The 2 fps acquisition rate is obviously not sufficiently high in order to track swimming bacteria, nevertheless it is enough to follow the displacement of non motile Brownian cells. We can identify and count Brownian bacteria by setting a speed threshold of 1 body length per second [56] and then subtract them from the total number $N_{tot}(z)$, obtaining the subset of motile ones, $N(z)$ for each given plane $z$. The total fraction of motile bacteria is then estimated by summing over all the planes $z_i$ imaged during the scan, namely $\varphi = \left(\sum_i N(z_i)\right) / \left(\sum_i N_{tot}(z_i)\right)$.

Finally, the swimming speed of our *E. coli* and *P. aeruginosa* is evaluated by tracking the motile cells on planes parallel and next to the two walls. In agreement with literature [153, 168], an average speed of about 30 $\mu$m/s and about 35 $\mu$m/s is found for *E. coli* and *P. aeruginosa*, respectively.

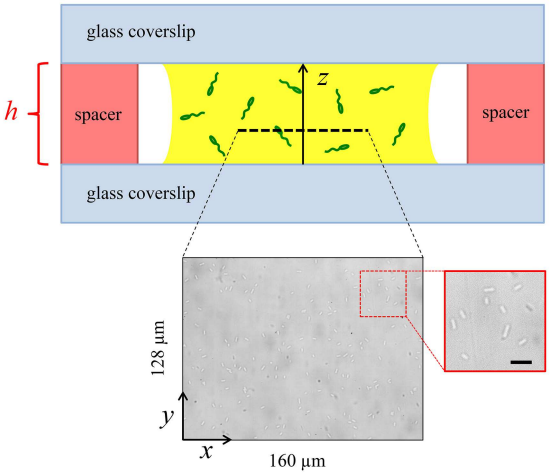


**Figure 5.2 :** Sketch of the experimental setup: a drop of bacterial suspension is closed between two glass coverslip with separation $h$ and it is observed in bright field along $z$ direction from below with focal plane $(x, y)$ parallel to the walls. The scale bar in the zoom of the field of view corresponds to 5 $\mu$m.

## § 5.4. Model and simulation settings

The simulations on motile particles confined within a slit rely on a coarse grained description of the micro-organism cell that neglects its flagella and models its body by a semi-flexible chain of $M$ beads, each of size $\sigma$ [169,170]. By fixing the length scale $\sigma$ and varying $M$, we can consider cells with different anisotropic ratio. Beads belonging to the same cell are kept together by finitely extensible nonlinear elastic (FENE) springs. The rigidity of each cell chain is achieved in terms of a Kratky-Porod potential

$$U_{KP} = \sum_{i=2}^{M} K \left( 1 - \frac{\mathbf{r}_{i-1} \cdot \mathbf{r}_i}{|\mathbf{r}_{i-1}| \, |\mathbf{r}_i|} \right) \tag{5.1}$$

where $\mathbf{b}_i \equiv \mathbf{r}_{i+1} - \mathbf{r}_i$ is the $i$-th chain bond and $K$ the bending parameter. Steric interactions between cells are enforced by assuming that beads belonging to different cells interact via a purely repulsive truncated and shifted Lennard-Jones (LJ) potential,

$$U_{i,j}^{LJ}(r) = \left\{ 4\epsilon \left[ \left( \frac{\sigma}{r} \right)^{12} - \left( \frac{\sigma}{r} \right)^{6} \right] - V_{LJ}(r = r_c) \right\} \theta(r - r_c) \tag{5.2}$$

where $r = |\mathbf{r}_i - \mathbf{r}_j|$ is the distance between the bead pair $(i, j)$ with position respectively $\mathbf{r}_i$ and $\mathbf{r}_j$, $r_c = 2^{1/6}\sigma$ and $\epsilon$ sets the strength of the interaction. A similar potential $U_W$ is used to describe the wall-bead interaction where $r = |\mathbf{r}_i - \mathbf{r}_w|$ is the distance between the $i$-th bead and the wall located at $\mathbf{r}_w$. In the simulations, the impenetrable walls are located at $z = 0$ and $z = h$ while along $x$ and $y$ periodic boundary conditions are assumed. The $i = 1$ and the $i = M$ bead are respectively the *head* and *tail* of the cell and self-propulsion is obtained by applying at each bead a force of strength $|\mathbf{F}_a|$ along the tail to head direction (cell *director*). This gives a total force per cell of modulus $M|\mathbf{F}_a|$. Since in our experiments there is always a fraction $1-\varphi$ of cells that are not motile, in the simulations we consider the possibility of having in the system a number $N_p$ of bodies for which $F_a = 0$. If we set

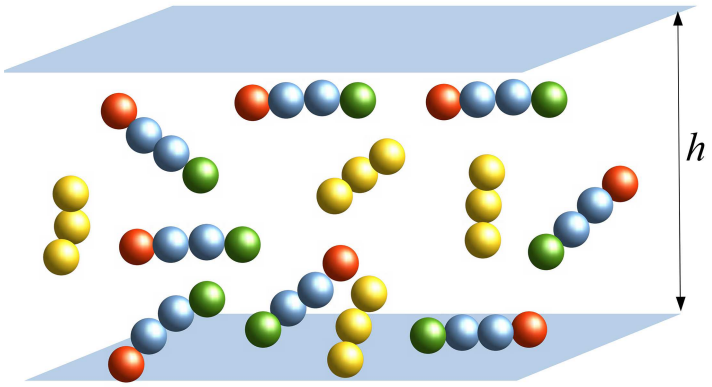


**Figure 5.3 :** Sketch of the model used in the simulations: for illustration purposes we made an example with bodies of different anisotropy: the multicolored ones are made by $M = 4$ beads and are characterized by a head (red) and a tail (green) bead. The active force $F_a$ is applied to each bead pointing along the tail-head direction. The yellow bodies are less anisotropic ($M = 3$). In this case no head-tail direction is highlighted since these bodies describe non motile cells ($F_a = 0$). Note that in the simulations reported in this work we have considered active and passive bodies with the same anisotropy (same $M$).

$U = U_{LJ} + U_{KP} + U_W$ as the full potential, the time evolution of the $i$-th bead follows a Langevin equation:

$$m_i \frac{d^2\mathbf{r}_i}{dt^2} = -\gamma \frac{d\mathbf{r}_i}{dt} - \nabla_i U + \boldsymbol{F}_a + \sqrt{2k_B T\gamma}\boldsymbol{\xi}_i(t), \tag{5.3}$$

where $\gamma$ is the viscous friction felt by each bead, $\nabla_i = \dfrac{\partial}{\partial \mathbf{r}_i}$, $k_B$ is the Boltzmann constant, $T$ is the temperature, $m_i \equiv m$ is the mass of the bead and $\boldsymbol{\xi}_i(t)$ is an uncorrelated Gaussian noise with zero mean and unit variance. It is important to notice that the total force acting on each bead in a cell is in general different, both in magnitude and direction, so that each cell rotates due to equation 5.3. Parameters are typically set to lead to strongly overdamped dynamics, which is realistic for microswimmers; the stiffness of the FENE springs is also strong enough that the distance between beads of the same cell is practically constant and equal to $\sigma$; similarly, the value of bending rigidity $K$ is chosen to be sufficiently large to reproduce an effectively rigid cell.

The above scheme describes a self-propelled anisotropic particle whose dynamics is essentially governed by the active deterministic force propelling the particle along its tail-head direction and the rotational/translation diffusion due to Brownian motion. To reproduce the run and tumble motility pattern of multiflagellated bacteria such as the wild-type *E. coli* strains, we include in the model the possibility that each body undergoes, from time to time, a tumbling mechanism. During a tumbling event, that we consider instantaneous, i.e. of duration $\tau_T \simeq dt$, the cell tries to perform a rigid rotation of a given angle $\theta_T$ around an axis passing through its center of mass and perpendicular to the cell axis. If the rotated cell overlaps with another cell, the move is rejected, otherwise the new position is updated. For simplicity, we fix the value of $\theta_T$ to $\sim 70°$, that is the expected average tumbling angle for wild type *E. coli* [48]. Between two tumbling events, the cell moves according to equation 5.3 (run). Since the total number of tumbles occurring up to a time $t$ is a Poisson process [145], the distribution of run duration is expected to be exponential. Hence, each cell attempts to perform a

tumbling motion after a run time $T_{run}$ that is randomly chosen from the distribution

$$p(T_{run} = t) = \frac{1}{\tau_R} e^{-t/\tau_R}, \tag{5.4}$$

where the average run time is of the order of $\tau_R \sim 10\tau_T \sim 1$ s [48] For a run and reverse motion we simply consider a run and tumble move with $\theta_T = 180°$.

Important dimensionless numbers to consider are the active *Peclet number*

$$Pe = \frac{F_a \sigma}{D_t \gamma} = \frac{F_a \sigma}{k_B T} \tag{5.5}$$

(where $D_t$ is the translational diffusion coefficient) and the volume fraction

$$\phi = \frac{MN \frac{4}{3}\pi \left(\frac{\sigma}{2}\right)^3}{V} = \frac{M\pi}{6}\frac{N}{V} \tag{5.6}$$

evaluated in terms of the total number of spheres present in the system. Since we fix $L_x = 200\sigma$ and $L_y = 200\sigma$, the system volume $V = L_x L_y h$ may vary with the slab height $h$ and, in order to keep $\phi$ fixed at the experimental value, the total number of cells $N$ in the system has to vary accordingly.

In order to devise and test a minimal model of motile particles that faithfully reproduces the experimental profiles and that can be used to extend the investigation to conditions non accessible to our experiments, we have simulated a system in which the beads chains are confined within a slit of height $h$ whose value is chosen coherently with the experimental one. For the cell body, we have neglected the contribution of the flagella in cell/cell and cell/wall steric interactions and assumed cells with aspect ratio 1/3, i.e. cells made by $M = 3$ beads each. In terms of physical lengths, by assuming $\sigma = 0.7$ $\mu$m this would give cells 2.1 $\mu$m long and 0.7 $\mu$m wide, in agreement with the sizes of the bacteria in the experiments. The system is initialized by inserting, one by one, in an ordered fashion, a total number $N$ of cells in the simulation box. This initial configuration that, by construction, does not present overlaps between cells, is then let to equilibrate and spread throughout the system. Once equilibrated, we add a force $F_a$ to the fraction $\varphi$ of cell that we want to be motile and its value is set to get an average speed value of the motile cells that is comparable to the one observed experimentally. In our simulations we consider Peclet numbers in the range $[150, 300]$. This corresponds to self-propelled bodies with an average speed of the order of $[27, 50]$ $\mu$m/s, i.e comparable to the ones of the bacteria analyzed in the experiments.

## § 5.5. Results and discussion

Here we describe our experimental results jointly with the numerical simulations. We first present the concentration profiles of WTM *E. coli* and of wild-type *P. aeruginosa* obtained experimentally for a wall separation of $h \approx 100$ $\mu$m and compare these results with the ones obtained from the simulation of anisotropic cells with either Run and Tumble or Run and Reverse motility patter. We then look at the effects that the degree of confinement (e.g. slit height $h$) and the fraction of motile bacteria can have on the aggregation of the bacteria at the walls. Finally we numerically investigate the role played by

the Peclet number (namely the active force) and the rate of anisotropy (namely the bacterium length) on the expected concentration profile.

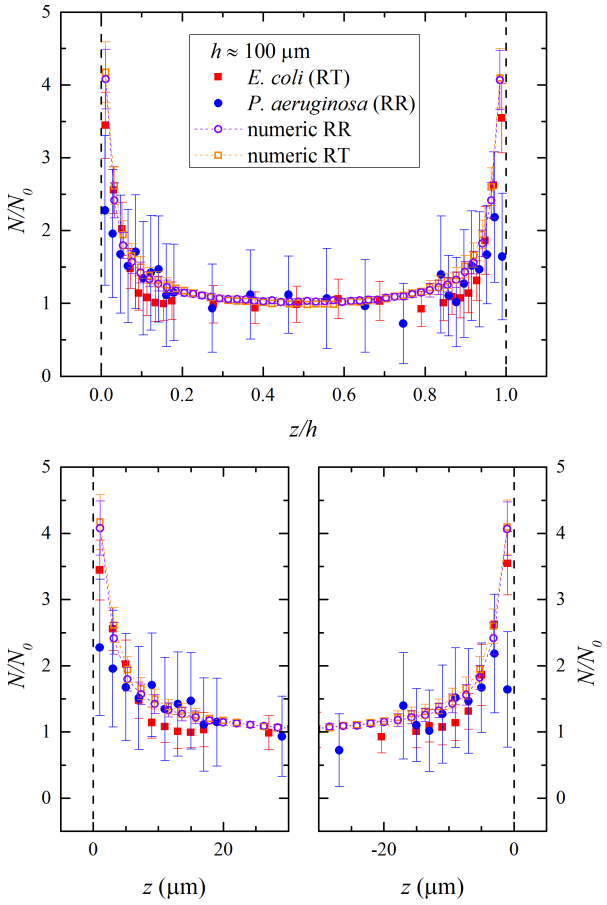


**Figure 5.4 :** Top panel: Experimental concentration profile obtained for WTM *E. coli* (full squares) and wild-type *P. aerugionosa* (full circles). The corresponding results from the simulations of the Run and Tumble (RT) (empty squares) and Run and Reverse (RR) (empty circles) models are reported for comparison. In this case the slit height $h \approx 100$ $\mu$m and 75% of the bacteria are motile. Bottom panels: Zoom of the concentration profiles near the walls.

Figure 5.4 compares the experimental density profiles obtained for MG1655 *E. coli* and wild-type *P. aeruginosa* at $h \approx 100$ $\mu$m with the simulation results for bodies with aspect ratio 1/3 and either Run and Tumble or Run and Reverse motility. Note that the concentration profile is obtained by normalizing the number of motile bacteria at a given height $z$, $N(z)$, with respect to the average value $N_0$ taken away from the walls when the concentration is roughly constant. Some features are worth mentioning: first, although the accumulation peaks for the *P. aeruginosa* are slightly lower with respect to the *E. coli*, the concentration profiles of the two species coincide within the statistical errors. Second, the simulation results agree nicely with the experimental ones and confirm that the aggregation of bacteria at the walls is significant (about 3.5 higher than the plateau away from the wall, see figure 5.4). Third, the whole concentration profile looks qualitatively independent of the motility pattern (Run and Tumble versus Run and Reverse) considered.

These results support the view that, although the details of the microscopic dynamics in proximity of the walls can be rather different, they have a negligible impact on the accumulation at the walls, a

feature that can be faithfully captured also by simple models of anisotropic motile particles confined in a slit.

### § 5.5.1. Effect of the degree of confinement

The effect of spatial confinement on concentration profile has been studied by changing the height $h$ of the spacer between the two glass coverslip. In figure 5.5 we report the experimental concentration profiles estimated at different slit heights $h$ within the range $[100, 250]$ $\mu$m. Panels (a) and (b) refer, respectively, to the WTM *E. coli* (Run and Tumble) and *P. aeruginosa* (Run and Reverse).

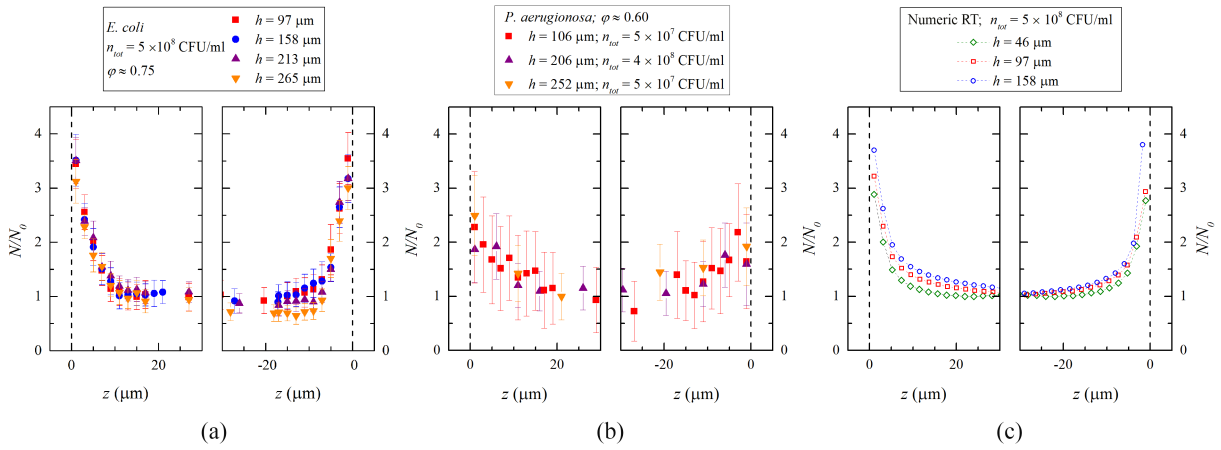


**Figure 5.5 :** Concentration profiles for different separations $h$ between the walls in the case of experimentally observed WTM *E. coli* (a) and wild-type *P. aeruginosa* (b) and numerically simulated Run and Tumble (RT) swimmers. The plots report the number of swimming cells $N$ normalized to the average number $N_0$ of the central plateau as a function of the distance $z$ from the walls in the near-wall regions.

Let us discuss first the behaviour of the *E. coli* (see figure 5.5a). As before, the profile of the number of swimming cells $N(z)$ is normalized to the average number $N_0$ in the region $\approx 30$ $\mu$m away from the walls. These samples have the same concentration $n_{tot} \approx 5 \times 10^8$ CFU/ml and the same fraction of swimming cells $\varphi \approx 0.75$. All profiles exhibit a concentration increase within 20 $\mu$m from the walls and a horizontal plateau in the central region. The values of the peaks observed in the proximity of the walls are about 3.5 times higher than the ones at the plateau.

Figure 5.5a show that all profiles coincide within error bars independently on the wall separation. The main discrepancy is found in the profile for $h = 265$ $\mu$m that displays a top-bottom asymmetry probably due to a mismatch of the buoyant densities. These results are in qualitative agreement with the concentration profiles found for WTM AW405 strain *E. coli* reported in [59], although our experimental profiles show a lower accumulation at the walls. A possible cause of this small discrepancy could be that the bacterial strains used in the two experiments differ either in average velocity or tumbling frequency.

Similar concentration profiles for the swimming *P. aeruginosa* are presented, for different $h$, in figure 5.5b. All samples have the same fraction of motile cells $\varphi \approx 0.60$. Irrespective of the slit height $h$, the profiles exhibit a concentration increase within about 20 $\mu$m from the walls and a horizontal plateau in the central region. The peaks in the proximity of the walls are about 2 – 2.5 times higher than the values observed at the plateau. The error bars for $h = 106$ $\mu$m and $h = 252$ $\mu$m are larger

than the ones for *E. coli* in figure 5.5b because of the lower concentration $n_{tot} = 5 \times 10^7$ CFU/ml. As for the *E. coli*, figure 5.5b displays profiles that, within error bars, can be considered unaffected by the degree of confinement.

In summary, the experimental findings show that, for these bacteria that differ by the swimming pattern, the accumulation at the walls and, more generally, the overall concentration profile are, at least for the volume fraction considered, independent on $h$. Note that the experiments have been performed for slits heights down to $h \gtrsim 100\mu$m. On the other hand the numerical simulations, that have been extended to slits of height as small as $h = 46$ $\mu$m and have smaller statistical errors, suggest a concentration profile that, when plotted as function of the distance $z$ from the wall (see figure 5.5c) is less pronounced at the walls as $h$ decreases It is important to stress that both in the experiments and in the simulations, although the space available changes with $h$, the concentration of the particles in the system is kept fixed. Hence no effects due to higher concentrations are expected.

### § 5.5.2. Results at different fraction of motile bacteria

Since the solution of bacteria used in the experiments often differ by the fraction of motile cells, we can ask whether, at fixed slit height $h$, the aggregation at the wall, and more generally the full profile, depends on the fraction $\varphi$ of motile cells in the system. Figure 5.6 shows the concentration profile of *E. coli* rescaled on the fraction of swimming bacteria $\varphi$ with $n_{tot} = 5 \times 10^8$ CFU/ml and for two values of $\varphi$. As one can see, the profile $N(z)$ scales with the fraction $\varphi$, in agreement with previous results for smooth-swimming *E. coli* [56].

The fact that the profiles do not depend on the fraction of motile cells is probably due to the relatively diluted suspensions of bacteria used in experiments. One can envisage that for very high bacteria concentration the presence of a finite fraction of passive cells would alter the overall profile of either the motile cells or the passive ones and possibly give rise to clustering effects at the walls due to presence of species with different motility.

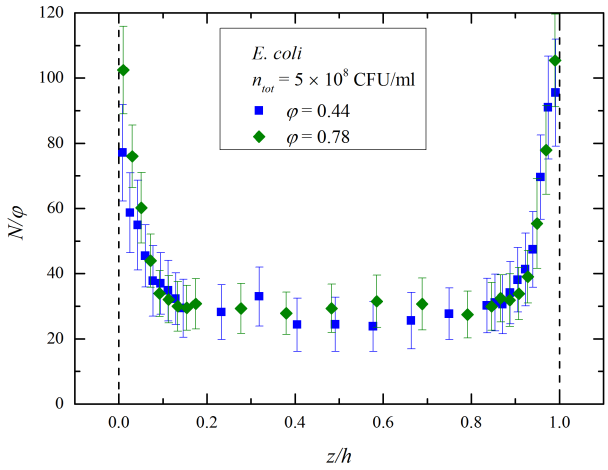


**Figure 5.6 :** Concentration profiles of motile WTM *E. coli* for two different fraction of swimming cells. The number of swimming cells $N$ is rescaled on the fraction $\varphi$.

### § 5.5.3. Effects of speed and anisotropy

The effects of the cells speed and the cell body anisotropy on the accumulation at the walls cannot be experimentally controlled. Motile cells of different speed are indeed expected to behave differently nearby the walls: more precisely, faster bacteria should accumulate more than slower ones [171, 172]. To check this effect, motile Run and Tumbling bodies with different Peclet number are simulated by keeping all the other parameters fixed. This is achieved by simply keeping the temperature fixed and by properly changing the value of the active force $F_a$. As expected, the peak of the cell's concentration at the walls increases as the Peclet number of the system increases (see figure 5.7a). In particular, the accumulation at the walls is twice as large for systems with $Pe = 210$ ($v_0 \sim 27$ $\mu$m/s) and becomes about 3.5 times larger for $Pe = 420$ ($v_0 \sim 50$ $\mu$m/s). In addition, within a distance of almost 20 $\mu$m from both walls, the higher the Peclet number the steeper is the accumulation curve.

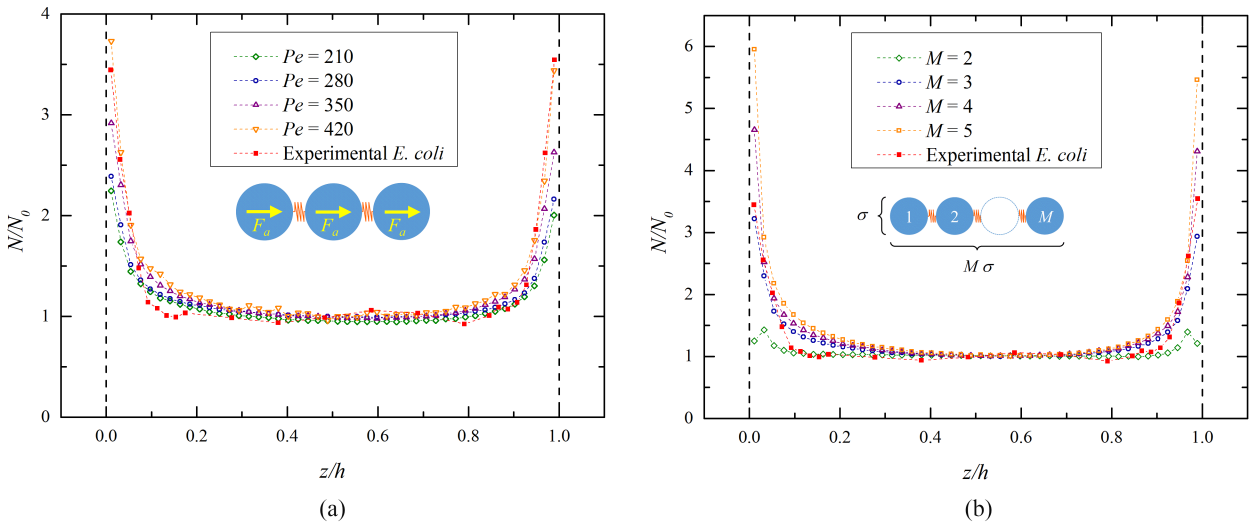


**Figure 5.7 :** (a) Concentration profile of Run and Tumble cells confined in a slit of height $h \simeq 100$ $\mu$m. Different symbols refer to different value of the active force and hence of the average speed. Note that for higher values of the average speed, the aggregation of the active swimmers near the walls increases. (b) Concentration profile of motile with Run and Tumble motion for different body aspect ratio. In the legend $M$ is the number of beads forming a single cell. For all cases the Peclet number is $Pe = 420$ corresponding to a body average speed of $\sim 50$ $\mu$m/s. The concentration of particles is $\sim 5 \times 10^8$ CFU/ml as in most of the experiments considered. The system is confined within a slit of height $h = 97$ $\mu$m.

A geometrical aspect that should affect the accumulation of motile cells at the walls is their degree of anisotropy or their aspect ratio $w/l$, where $w$ and $l$ are, respectively, the width and the length of the cell body. By keeping fixed the diameter of the beads forming a cell we have then varied their number $M$ from $M = 2$ up to $M = 5$, corresponding respectively to aspect ratios from 1/2 to 1/5. The simulation has been performed with all the other parameters (i.e. $\phi$, $\varphi$, $h$ and $F_a$) fixed. The results of how the density profile depend on $M$ have been reported in figure 5.7b: one can notice that, as $M$ increases (i.e. as the cells becomes more anisotropic) the aggregation at the walls is extremely enhanced. For instance, for motile cells with aspect ratio 1/5 the peaks developed in proximity of the walls are about six times higher than the constant values (plateau) in the bulk. This behaviour is independent on the average speed of the swimmer. Notice that, as before, since the beads chains concentration is kept fixed at $5 \times 10^8$ ml$^{-1}$ an increase in $M$ corresponds to a decrease of the total

number of cells. However, further tests performed with concentrations up to $10^9$ ml$^{-1}$ and $M = 5$ (this gives roughly the same number of cells with $M = 3$) yield very similar results.

## § 5.6. Conclusions

To summarize, we have studied experimentally the concentration profiles of bacterial suspensions confined in slits of heights $h$ that are comparable with the typical persistence length of the cells. In particular, we have considered MG1655 *E. coli* and wild-type *P. aerugionosa* bacteria, whose motilities are characterized by the *Run and Tumble* and the *Run and Reverse* patterns, respectively. The experimental results have been compared with numerical simulations of a simple model of self-propelling bodies whose main ingredients are the anisotropy of the bodies and the excluded volume interaction between bodies and with the walls. One of our main findings is that in both experiments and numerical simulations we observe that, although the motility patterns of the two species are different, the concentration profiles are similar and characterised by a consistent increase of the number of bacteria within layers of about 20 $\mu$m from the walls. Moreover the concentration profiles are, within the error bars and for the range of $h$ considered, insensitive to the degree of confinement, as well as on the fraction of motile cells, due to the relatively low concentration of the bacterial solutions.

These findings, that confirm previous studies on bacteria aggregation performed on single species [56–59], indicate that, although the microscopic dynamics in proximity of the walls can be rather different, this has a negligible overall impact on the accumulation at the walls, a feature that has been faithfully captured by our simple model of motile cells. Moreover, the fact that our model does not consider long-range hydrodynamic interactions suggests that, at least for the density of bacteria considered and for the two mechanisms of motion studied (i.e. Run and Tumble and Run and Reverse) this effect is not crucial to establish the profile at the walls. Finally, our simulations show that the amount of motile cells at the walls increases both with their average speed and with the aspect ratio of the cell's geometry. For future work, it would be of interest to perform similar joint theoretical and experimental analysis of suspensions of other micro-organisms confined within slits by considering either other motility patterns (e.g. *smooth-swimming* or *reverse and flick* motion [155]) or cells with different aspect ratios. More important, increasing the bacteria concentration or strongly confining the suspension in microfluidic channels [173, 174] would provide useful insights on the interplay between crowding and confinement.

# Conclusions

This thesis gathers the research work done during the PhD, which has dealt with microfluidic systems. In particular, we have studied:

- the dynamics of sessile drops subject to oscillations of the substrate, with the aim of achieve an active control of drop motion and shape, in the frame of open microfluidics;
- the effects of confined geometries on suspension of swimming bacteria, viewed as active colloids. The study of these effects can help the understanding of microbiological issues, such as bacterial biofilm formation.

Concerning the first topic, we have studied the behaviour of drops deposited on an inclined surface subject to vertical harmonic oscillations ranging from 30 to 120 Hz. In order to vary viscosity and surface tension of the fluid, we have considered distilled water and glycerol/water, ethanol/water and isopropanol/water solutions at different concentrations. Typically, small droplets on inclined surfaces remain pinned because of contact angle hyseresis. When vertical oscillations are applied above a threshold acceleration, the droplets unpin and slide down. Surprisingly, for sufficiently large oscillation acceleration the droplets move upward against gravity. The viscosity of the liquid solution does not seem to affect significantly the dynamical phase diagrams, at least in the explored range. Instead, low surface tensions, i.e. low contact angles, are found to hinder climbing and favour sliding of drops. The time evolution of the drop profile has been observed by mean of a fast camera (operating at 4 kHz). In this way, we could compare the oscillatory behaviour of the contact line with that of the upper and lower contact angles. Complementary numerical simulations reproduce the overall behaviour and the profile evolution, suggesting that the direction of motion is related to the circulation inside the drop.

The exploitation of these effects offer the possibility to control and manipulate droplets on a substrate by tuning frequency and acceleration of the vertical vibration and drop volume.

As next step, we have started the investigation of these phenomena in the case of non-Newtonian fluids displaying elastic behaviour, such as the presence of first normal stress difference. We are considering polymeric aqueous solutions of Xanthan (a stiff rod-like polysaccaride) at high concentration or of polyacrylamide.

Then, we have considered the interfacial morphologies of water confined to the hydrophilic top face of rectangular posts of width $W = 0.5$ mm and lengths between $L = 10W$ and $36W$. For small volumes, the liquid film adopts the shape of a homogeneous filament with a uniform cross section close to a circular segment. For large volumes, the water interface forms a central bulge, which grows with

the volume. For short posts with aspect ratio $L/W < 16$, there was not a well defined separation between the two morphologies, but a countinuous cross-over as the volume varied. On the other hand, for long posts with $L/W > 16$, we found a clear distinction between the morphologies with a sharp and discontinuous transition for changing volume, displaying a hysteretic behaviour associated to a bistability volume interval.

In addition, thanks to the presence of the bistability volume interval, we could induce the transition from channel to bulged morphology by applying vertical oscillations. We observed that the transition occurs for all the frequencies in the scanned range between 350 Hz and 850 Hz, except for the frequencies close to 500 Hz, at which the the channel displays a resonant mode. Currently, our theoretical collaborators are working on a model explaing these intriguing experimental observations.

This experimental study shows the possibility of an active control on the shape of the confined drop, either by changing the volume or by means of vibration of the substrate.

About the second topic, we have investigated the influence of confinement, in particular with a slit-like geometry, on bacterial suspensions of *E. coli* or *P. aeruginosa*, carachterized by *Run and Tumble* and *Run and Reverse* motility patterns, respectively. We found that, although the motility patterns of the two species are different, the concentration profiles are similar and characterised by a consistent increase of the number of bacteria within layers of about 20 $\mu$m from the walls. Moreover the concentration profiles are, for the range of slit thikness $h$ considered, insensitive to the degree of confinement, as well as on the fraction of motile cells. This results are in agreement with numerical simulation based on a collection of self-propelled rod-like particles interacting only through steric interactions.

These findings suggest that the different microscopic behaviour in proximity of the walls has a negligible overall impact on the accumulation. Moreover, the fact that our model does not consider long-range hydrodynamic interactions suggests that, at least for the density of bacteria considered and for the two mechanism of motion studied this effect is not crucial to establish the profile at the walls.

# Appendix A

# Microfabrication details

Here we describe the microfabication techniques based on photolithography and soft-lithography [131, 175, 176] usually employed in the production of microfluidic devices [9] and, in particular, of the posts used in the experiments described in chapter 3. The first step is the production of a master copy by photolithographic techniques. Then, the master is replicated by molding technique in poly(dimethylsiloxane) (PDMS), as described in section 3.2.

## § A.1. Photolithography

Photolithography is one of the most common processes in microfabrication. It allows to transfer a pattern from an optical mask, that presents transparent and opaque areas, to a layer of a photosensitive polymeric material, referred as photoresist or more simply resit, by exposing to UV radiation, typically in the spectral band between 300 nm and 450 nm. Photoresists divide in two types depending on the different reaction induced by UV light (see figure A.1):

- *Positive resist* becomes soluble in proper solvents where exposed due to the weakening and the breaking of the polymeric chains caused by radiation, while it remains insoluble where unexposed.
- *Negative resist* becomes insoluble in proper solvents where exposed because of the light-induced cross-linking of the polymeric chains, while it remains soluble where unexposed.

The products employed in photolithography are solutions composed of the photoresist, a solvent, to reduce the viscosity allowing the deposition on a substrate, and an additive to control the kinetics of the light-induced reaction.

The main steps of the photolithographic process are the deposition of a thin layer of photoresist on a substrate, the illumination through the mask and the removal of the unpolymerized resist. In order to obtain a homogeneous layer, the resist is deposited on a solid substrate, usually a silicon wafer or a glass slide, by spin-coating, i.e. by rotating the substrate, on which the liquid resist is poured, at typical angular velocity between 1000 rpm and 10 000 rpm, depending on the thickness required. After a bake to evaporate the solvent, the layer of resist is exposed to the radiation from a collimated UV lamp through a photolithographic mask, usually consisting in a quartz plate on which the pattern to be reproduced is realized by chrome deposition. At this point, the unpolymerized resist is removed by washing with a proper solvent.

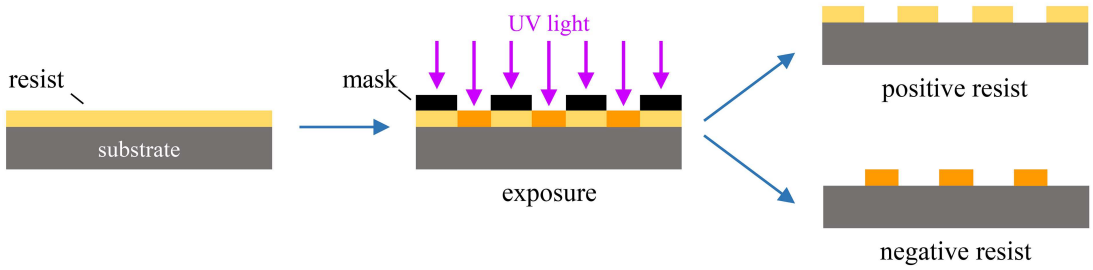


**Figure A.1 :** Different outcome of UV light exposure for positive and negative resists.

The upper limit to the resolution of the transferred pattern is fixed by the resolution of the mask. Other relevant parameters are the wavelength of the radiation, the distance between mask and resist and the thickness of the layer. Since the cleanness of operation environment is also very important, photolithography is carried out in clean room, i.e. a laboratory in which temperature and humidity are regulated and air is filtered and subjected to laminar flow.

### § A.1.1. Photolithography with SU-8 negative resist

For the realization of master copies of the rectangular posts presented in chapter 3, we used SU-8 2050 negative photoresist (MicroChem Corp.) [177] on silicon wafers. SU-8 is an epoxy based photoresist which allows the production of high aspect ratio structures with a very good adhesion to the substrate. Given its high viscosity (12 900 cSt), SU-8 2050 is suitable for the production of thick structures, such as our posts ($\approx 150-200$ $\mu$m). The steps of the photolithographic process, performed in a clean room (ISO 7 class), are schematized in figure A.2.

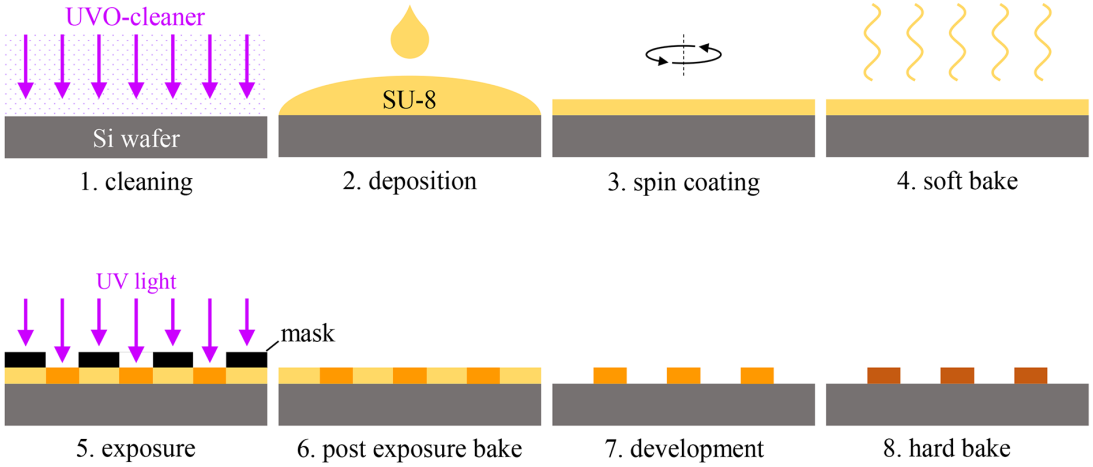


**Figure A.2 :** Steps of photolithographic process with SU-8 negative photoresist: 1. UVO-celaner treatment of the silicon wafer substrate; 2. deposition of the photoresist on the substrate; 3. production of a homogeneous layer with the required thickness by spin-coating; 4. soft bake to make photoresist solvent evaporate; 5. cross-linking induced by UV light exposure through a mask; 6. post exposure bake to promote and stabilize cross-linking; 7. removal of the uncross-linked photoresist by washing with proper organic solvent; 8. final bake to strengthen the structure.

**Preparation of the substrate.** 500 $\mu$m thick silicon wafer is cleaned with isopropanol, dried by nitrogen gas flux and treated in UVO-cleaner for at least 30 minutes. Silicon wafer allows a better

adhesion of the resist with respect to glass due to its lower roughness.

**Deposition.** SU-8 is poured on the wafer and spin-coated by means of the WS-650 Spin Processor (Laurell Technologies Corp.). During rotation, most part of the liquid resist is expelled and a thin homogeneous film remains on the substrate. The film thickness is set by spin velocity (see figure A.3a). The spin-coating procedure consists of three steps, the first and second steps, each 10 s long, have spin velocity 1/10 and 1/2 of the velocity $\omega_{max}$ of the last step, that is 80 s long, respectively (see figure A.3b). A film thickness of $\approx 150 - 200$ $\mu$m is obtained by setting a final spin velocity $\omega_{max} = 1000$ rpm. During the spin-coating, a thick build-up of resist may occur at the edge of the substrate. The removal of this edge bead allows to place the mask into close contact with the film during exposure, resulting in improved resolution. It is recommended to let the coated substrate at rest for 2 or 3 hours before the next step, in order that the resist film relaxes and becomes more uniform and homogeneous.

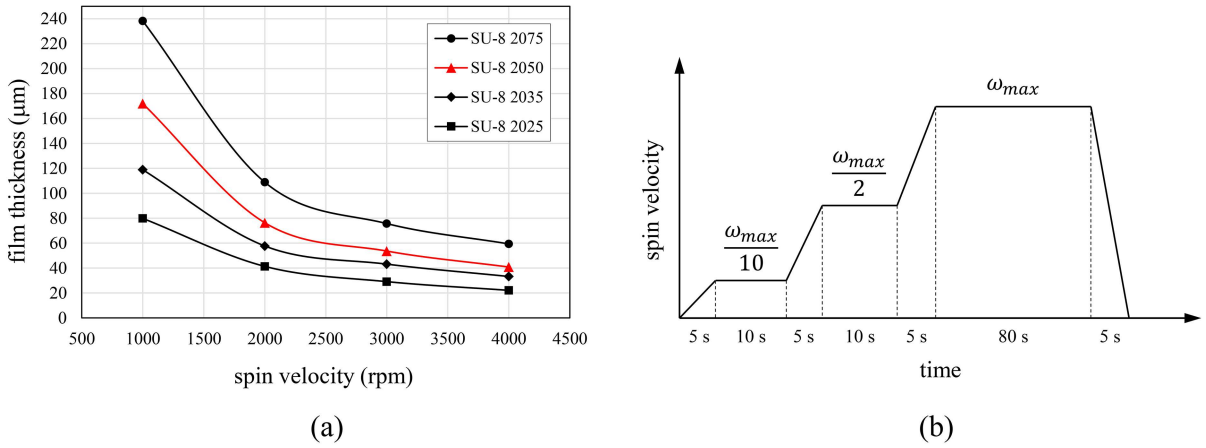


**Figure A.3 :** (a) Spin velocity versus film thickness for SU-8 resists with different viscosities [177]. The red curve refers to SU-8 2050. (b) Three steps of the spin-coating procedure. The first and second steps have spin velocities 1/10 and 1/2 of the final velocity $\omega_{max}$, respectively.

**Soft bake.** The coated substrate is heated on a hotplate to allow the evaporation of photoresist solvent and a partial hardening of the resit. According to the processing guidelines [177], for film thickness of about 150 $\mu$m the soft bake is preformed at 65°C for 5 minutes and then at 95°C for 20 minutes. We found that a bake with a very slow ramp from room temperature to a final temperature of 65°C for about 45 minutes results in a more homogeneous film.

**Exposure.** The resist film, with the mask in close contact, is exposed to collimated UV radiation from a mercury arc lamp (UV400, Reinraumtechnik Lanz). Since the recommended wavelength for SU-8 is 365 nm (i-line), UV radiation below 350 nm is eliminated by a longpass filter (ZUL0350, Asahi Spectra USA Inc.). An important parameter is the exposure dose required for the cross-linking of the whole film thickness. The dose for 150 $\mu$m is 260 mJ/cm$^2$, corresponding to an exposure time of 40 s. Given the lateral dimensions of our structures on millimetric scale, micrometric resolution is not required. Therefore, the masks we employed were realized by high-quality printout (4000 DPI) on transparency sheets (see figure A.4).

**Post exposure bake.** In order to complete and stabilize the cross-linking reactions induced by UV exposure, a second bake is required. The 150 $\mu$m thick film is heated at 65°C for 5 minutes and

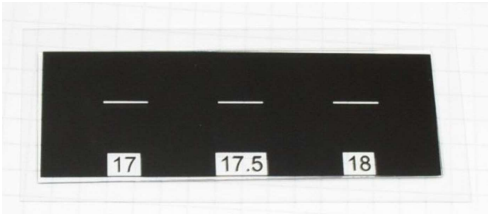


**Figure A.4 :** Photolithographic mask, realized by high-quality printout on transparency sheet, for the production of rectangular posts with width $W = 0.5$ mm and lengths $L = 8.5$ mm, 8.75 mm, 9 mm, corresponding to aspect ratios $\ell = L/W = 17, 17.5, 18$.

then at 95°C for 15 minutes.

**Development.** The unexposed resist is removed by washing the samples immersed in the proper organic solvent (SU-8 Developer Y020100, MicroChem Corp.). After the removal, the samples are dried by blowing nitrogen gas.

**Hard bake.** A final bake at $100 - 150$°C for 30 minutes enhances mechanical and thermal properties of the structures.

An example of the final SU-8 structure on silicon wafer, used as master copy for rectangular posts, is shown in figure A.5.

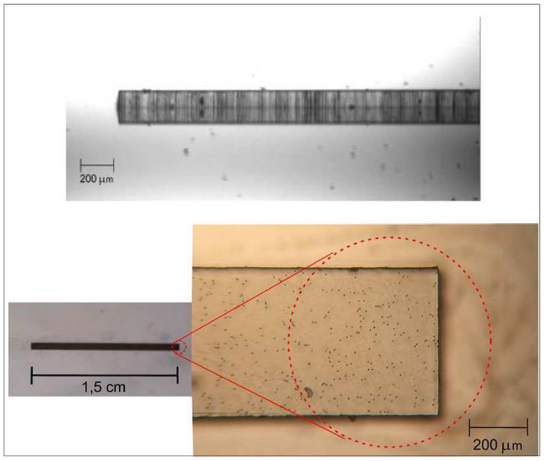


**Figure A.5 :** Side and top views of a SU-8 structure on silicon substrate.

## § A.2. Soft-lithography

Soft-lithography consists of non-photolithographic methods to transfer a geometrical pattern from a mold to a "soft" material, i.e. polymeric material [131]. With respect to photolithography, soft-lithographic techniques involve simpler procedures and equipment, usually do not require a clean room and the typical materials used are cheaper. Nevertheless, soft-lithography allows high-quality and high-reproducibility fabrication of micro- and nano-structures. Among the most common methods we can mention molding techniques, such as replica moding, hot embossing and injection molding, and microcontact printing (see figure A.6).

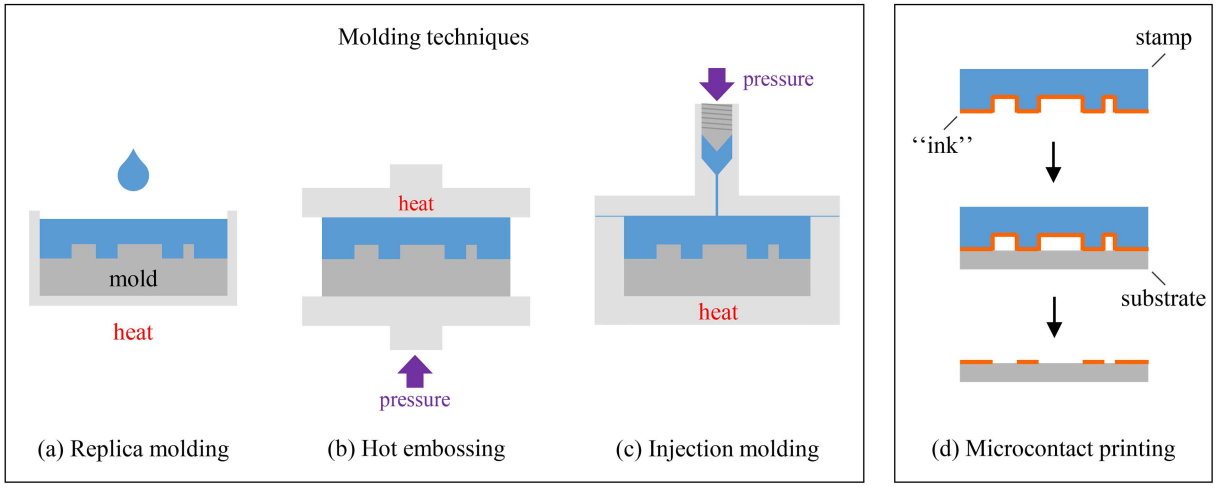


**Figure A.6 :** Examples of soft-lithographic techniques [9, 131]. (a) Replica molding: a mix of liquid polymer and catalyst, poured on the mold, is cured by heating. (b) Hot embossing: the mold is pressed against a heated plastic material. (c) Injection molding: a heated liquid polymeric material is injected into the mold. The result of these three molding techniques is a negative copy of the mold. (d) Microcontact printing: the pattern of a polymeric stamp soaked in a chemical "ink" is transferred onto a substrate forming a self-assembled monolayer (SAM).

### § A.2.1. Replica molding in PDMS

Poly(dimethylsiloxane) (PDMS) is an elastomeric silicon-based organic polymer widely employed for the fabrication of microfluidic devices. Its chemical structure, illustrated in figure A.7, is made of an inorganic siloxane backbone and organic methyl groups attached to silicon. PDMS is fluid at room temperature, due to the low glass transition temperature ($T_g \approx -125°C$), but it becomes a solid elastomer by reticulation when liquid pre-polymer and a platinum based curing agent are mixed together (see figure A.8). The reticulation reaction can be sped up by heating. The main properties of the PDMS elastomer are reported in table A.1.

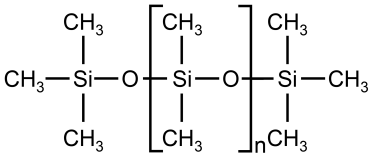


**Figure A.7 :** Chemical structure of poly(dimethylsiloxane) (PDMS): an inorganic siloxane backbone (-Si-O-) and organic methyl groups ($-CH_3$) attached to silicon.

Due to the presence of the methyl groups, PDMS elastomer is hydrophobic with a contact angle of about 110°. Nevertheless, its surface chemistry can be modified by plasma oxidation, adding silanol (SiOH) groups. The result is a hydrophilic surface, which is not stable over time but gradually recovers its hydrophobicity due to the diffusion of low molecular weight chains from the bulk [132]. The oxidized surface can be further functionalized with trichlorosilanes or other polymers, such as poly(ethylene oxide) (PEO) or poly(vinyl pyrrolidone) (PVP) [178–180].

Given its properties and its reticulation process, PDMS is an ideal material for replica molding of very complex and resolute structures: a negative copy of a master can be realized by pouring onto it the liquid polymer, heating and peeling off the reticulated elastomer (see figure A.9). If the master

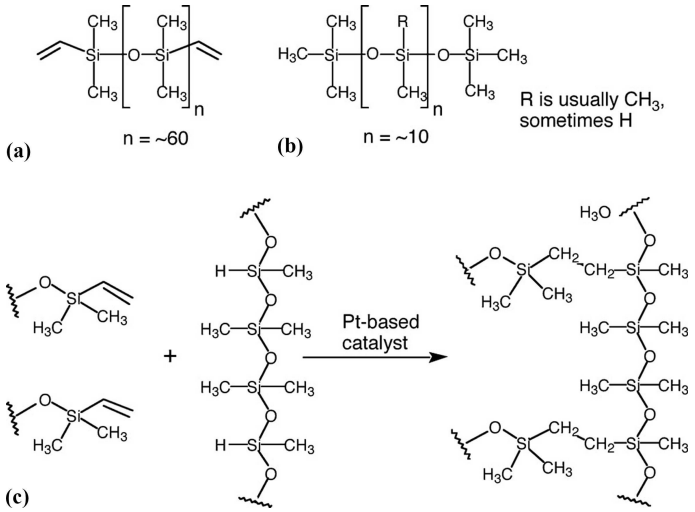


**Figure A.8 :** The commercially available kit for the production of the PDMS elastomer (Sylgard 184, Dow Corning) consists of liquid vinyl-terminated PDMS (a) and the curing agent which is a mixture of a platinum catalyst and copolymer of methylhydrosiloxane and dimethylsiloxane (b). The reticulation occurs via the reaction between vinyl ($SiCH{=}CH_2$) groups and hydrosilane (SiH) groups, activated by the platinum catalyst (c).

| Property | Characteristic |
|---|---|
| Density | $\approx 0.9 \mathrm{kg/m^3}$ |
| Optical | Transparent in the wavelength range from 330 nm to 2200 nm |
| Mechanical | Elastomer with Young's modulus $\sim$ 750 kPa |
| Electrical | Insulator with braking field $\sim 20 kV/cm$ |
| Thermal | Insulator with thermal conductivity $\sim 0.2\ \mathrm{Wm^{-1}K^{-1}}$ |
| Interfacial | Low surface energy $\sim$ 20 mN/m; hydrophobic |
| Permeability | Permeable to gas; swollen by nonpolar organic solvents; nearly impermeable to water |
| Reactivity | Inert, oxidizable by plasma |
| Toxicity | Non-toxic, biocompatible |

**Table A.1 :** Physico-chemical properties of PDMS [9].

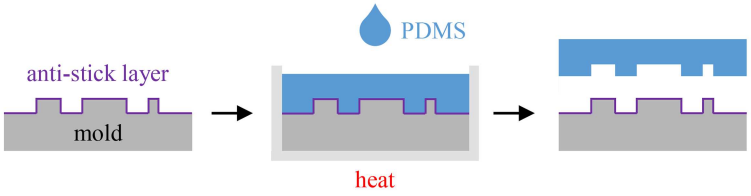


**Figure A.9 :** Replica molding with PDMS on silicon mold.

is fabricated by photolithography on silicon or glass substrate, it is recommended to functionalize its surface with an anti-stick layer in order to avoid PDMS bonding during reticulation. Usually, the master is silanized by exposure to the vapour of trichloroperfluorooctylsilane ($CF_3(CF_2)_6(CH_2)_2SiCl_3$). The steps of the replica molding procedure are:

- mixing of the liquid pre-polymer and curing agent in 10:1 (w/w) ratio;
- removing of air bubbles trapped during mixing by degassing with a vacuum pump;
- pouring of the liquid mixture on the silanized master taking care not to produce air bubbles;
- bake of the PDMS covered master in a oven at 80° for 40 minutes;
- detachment of the replica from the master by gently peeling it off.

# Acknowledgements

At the end of my PhD adventure I have to thank a few people whose support has been essential.

First of all, I would like to thank my supervisor Dr. Matteo Pierno and my co-supervisor Prof. Giampaolo Mistura for guiding me with dedication through the world of research. I am grateful to "Uncle" Giorgio Delfitto and to all my present and past PhD and post-doc colleagues, Davide Ferraro, Silvia Varagnolo, Enrico Chiarello, Daniele Filippi, Carlo Rigoni, Ladislav Derzsi, Emanuele Locatelli and Greshia Cappozzo for the help in many experiments and for the wonderful spirit they contribute to create at the LaFSI (Surface and Interface Physics Lab). I also thank people from the other Matter Physics groups at the Physics and Astronomy department of University of Padova.

Last but not least, my family deserves all my gratitude and my devotion for the never-ending support in every circumstance. In particular, thanks to Enrica for being always patient and lovely.

# Bibliography


[1] W. Federle, W. J. P. Barnes, W. Baumgartner, P. Drechsler, and J. M. Smith, "Wet but not slippery: boundary friction in tree frog adhesive toe pads," *Journal of The Royal Society Interface*, vol. 3, no. 10, pp. 689–697, 2006.

[2] B. N. J. Persson, "Wet adhesion with application to tree frog adhesive toe pads and tires," *Journal of Physics: Condensed Matter*, vol. 19, no. 37, p. 376110, 2007.

[3] P.-G. De Gennes, F. Brochard-Wyart, and D. Quéré, *Capillarity and Wetting Phenomena: Drops, Bubbles, Pearls, Waves*. Springer Science & Business Media, 2004.

[4] D. Myers, *Surfaces, interfaces and colloids*. Wiley-VCH New York etc., 1990.

[5] P.-G. de Gennes, "Wetting: statics and dynamics," *Reviews of Modern Physics*, vol. 57, pp. 827–863, 1985.

[6] J. Berthier, *Micro-drops and digital microfluidics*. William Andrew, 2012.

[7] T. Pfohl, F. Mugele, R. Seemann, and S. Herminghaus, "Trends in microfluidics with complex fluids," *ChemPhysChem*, vol. 4, no. 12, pp. 1291–1298, 2003.

[8] G. M. Whitesides, "The origins and the future of microfluidics," *Nature*, vol. 442, no. 7101, pp. 368–373, 2006.

[9] P. Tabeling, *Introduction to microfluidics*. Oxford University Press on Demand, 2005.

[10] M. Rauscher, S. Dietrich, and J. Koplik, "Shear flow pumping in open micro-and nanofluidic systems," *Physical Review Letters*, vol. 98, no. 22, p. 224504, 2007.

[11] R. Ledesma-Aguilar, R. Nistal, A. Hernández-Machado, and I. Pagonabarraga, "Controlled drop emission by wetting properties in driven liquid filaments," *Nature Materials*, vol. 10, no. 5, pp. 367–371, 2011.

[12] H. Gau, S. Herminghaus, P. Lenz, and R. Lipowsky, "Liquid morphologies on structured surfaces: from microchannels to microchips," *Science*, vol. 283, no. 5398, pp. 46–49, 1999.

[13] R. Seemann, M. Brinkmann, E. J. Kramer, F. F. Lange, and R. Lipowsky, "Wetting morphologies at microstructured surfaces," *Proceedings of the National Academy of Sciences of the United States of America*, vol. 102, no. 6, pp. 1848–1852, 2005.

[14] A. Klingner and F. Mugele, "Electrowetting-induced morphological transitions of fluid microstructures," *Journal of applied physics*, vol. 95, no. 5, pp. 2918–2920, 2004.

[15] D. Ferraro, C. Semprebon, T. Toth, E. Locatelli, M. Pierno, G. Mistura, and M. Brinkmann, "Morphological transitions of droplets wetting rectangular domains," *Langmuir*, vol. 28, no. 39, pp. 13919–13923, 2012.

[16] A. Ghosh, R. Ganguly, T. M. Schutzius, and C. M. Megaridis, "Wettability patterning for high-rate, pumpless fluid transport on open, non-planar microfluidic platforms," *Lab on a Chip*, vol. 14, no. 9, pp. 1538–1550, 2014.

[17] L. Y. Yeo and J. R. Friend, "Surface acoustic wave microfluidics," *Annual Review of Fluid Mechanics*, vol. 46, pp. 379–406, 2014.

[18] S. Daniel, M. K. Chaudhury, and P.-G. De Gennes, "Vibration-actuated drop motion on surfaces for batch microfluidic processes," *Langmuir*, vol. 21, no. 9, pp. 4240–4248, 2005.

[19] M. Abdelgawad and A. R. Wheeler, "The digital revolution: a new paradigm for microfluidics," *Advanced Materials*, vol. 21, no. 8, pp. 920–925, 2009.

[20] K.-i. Ohno, K. Tachikawa, and A. Manz, "Microfluidics: applications for analytical purposes in chemistry and biochemistry," *Electrophoresis*, vol. 29, no. 22, pp. 4443–4453, 2008.

[21] S. K. Sia and G. M. Whitesides, "Microfluidic devices fabricated in poly (dimethylsiloxane) for biological studies," *Electrophoresis*, vol. 24, no. 21, pp. 3563–3576, 2003.

[22] D. B. Weibel and G. M. Whitesides, "Applications of microfluidics in chemical biology," *Current Opinion in Chemical Biology*, vol. 10, no. 6, pp. 584–591, 2006.

[23] A. D. Sommers, T. J. Brest, and K. F. Eid, "Topography-based surface tension gradients to facilitate water droplet movement on laser-etched copper substrates," *Langmuir*, vol. 29, no. 38, pp. 12043–12050, 2013.

[24] C. Semprebon, S. Varagnolo, D. Filippi, L. Perlini, M. Pierno, M. Brinkmann, and G. Mistura, "Deviation of sliding drops at a chemical step," *Soft Matter*, vol. 12, pp. 8268–8273, 2016.

[25] O. Bliznyuk, H. P. Jansen, E. S. Kooij, H. J. W. Zandvliet, and B. Poelsema, "Smart design of stripe-patterned gradient surfaces to control droplet motion," *Langmuir*, vol. 27, no. 17, pp. 11238–11245, 2011.

[26] S. Varagnolo, V. Schiocchet, D. Ferraro, M. Pierno, G. Mistura, M. Sbragaglia, A. Gupta, and G. Amati, "Tuning drop motion by chemical patterning of surfaces," *Langmuir*, vol. 30, no. 9, pp. 2401–2409, 2014.

[27] S. K. Cho, H. Moon, and C.-J. Kim, "Creating, transporting, cutting, and merging liquid droplets by electrowetting-based actuation for digital microfluidic circuits," *Journal of Microelectromechanical Systems*, vol. 12, no. 1, pp. 70–80, 2003.

[28] S. C. C. Shih, H. Yang, M. J. Jebrail, R. Fobel, N. McIntosh, O. Y. Al-Dirbashi, P. Chakraborty, and A. R. Wheeler, "Dried blood spot analysis by digital microfluidics coupled to nanoelectrospray ionization mass spectrometry," *Analytical Chemistry*, vol. 84, no. 8, pp. 3731–3738, 2012.

[29] N.-T. Nguyen, K. M. Ng, and X. Huang, "Manipulation of ferrofluid droplets using planar coils," *Applied Physics Letters*, vol. 89, no. 5, p. 052509, 2006.

[30] X. Noblin, R. Kofman, and F. Celestini, "Ratchetlike motion of a shaken drop," *Physical Review Letters*, vol. 102, no. 19, p. 194504, 2009.

[31] F. Mugele and J.-C. Baret, "Electrowetting: from basics to applications," *Journal of Physics: Condensed Matter*, vol. 17, no. 28, p. R705, 2005.

[32] M. G. Pollack, A. D. Shenderov, and R. B. Fair, "Electrowetting-based actuation of droplets for integrated microfluidics," *Lab on a Chip*, vol. 2, no. 2, pp. 96–101, 2002.

[33] M. J. Jebrail, M. S. Bartsch, and K. D. Patel, "Digital microfluidics: a versatile tool for applications in chemistry, biology and medicine," *Lab on a Chip*, vol. 12, no. 14, pp. 2452–2463, 2012.

[34] R. B. Fair, "Digital microfluidics: is a true lab-on-a-chip possible?," *Microfluidics and Nanofluidics*, vol. 3, no. 3, pp. 245–281, 2007.

[35] Y.-H. Chang, G.-B. Lee, F.-C. Huang, Y.-Y. Chen, and J.-L. Lin, "Integrated polymerase chain reaction chips utilizing digital microfluidics," *Biomedical Microdevices*, vol. 8, no. 3, pp. 215–225, 2006.

[36] K. Choi, A. H. C. Ng, R. Fobel, and A. R. Wheeler, "Digital microfluidics," *Annual Review of Analytical Chemistry*, vol. 5, pp. 413–440, 2012.

[37] N.-T. Nguyen, "Micro-magnetofluidics: interactions between magnetism and fluid flow on the microscale," *Microfluidics and Nanofluidics*, vol. 12, no. 1-4, pp. 1–16, 2012.

[38] S. Mettu and M. K. Chaudhury, "Motion of liquid drops on surfaces induced by asymmetric vibration: role of contact angle hysteresis," *Langmuir*, vol. 27, no. 16, pp. 10327–10333, 2011.

[39] P. Brunet, J. Eggers, and R. D. Deegan, "Vibration-induced climbing of drops," *Physical Review Letters*, vol. 99, no. 14, p. 144501, 2007.

[40] S. Daniel and M. K. Chaudhury, "Rectified motion of liquid drops on gradient surfaces induced by vibration," *Langmuir*, vol. 18, no. 9, pp. 3404–3407, 2002.

[41] G. I. Menon, *Active Matter*, pp. 193–218. Springer New York, 2010.

[42] D. Saintillan and M. J. Shelley, "Theory of active suspensions," in *Complex Fluids in Biological Systems*, pp. 319–355, Springer, 2015.

[43] E. Lauga, "Life around the scallop theorem," *Soft Matter*, vol. 7, no. 7, pp. 3060–3065, 2011.

[44] M. C. Marchetti, J. F. Joanny, S. Ramaswamy, T. B. Liverpool, J. Prost, M. Rao, and R. A. Simha, "Hydrodynamics of soft active matter," *Reviews of Modern Physics*, vol. 85, no. 3, 2013.

[45] M. E. Cates, "Diffusive transport without detailed balance in motile bacteria: does microbiology need statistical physics?," *Reports on Progress in Physics*, vol. 75, no. 4, p. 042601, 2012.

[46] W. C. K. Poon, "From clarkia to escherichia and janus: The physics of natural and synthetic active colloids," in *International School of Physics Enrico Fermi*, vol. 184 of *Proceedings of the International School of Physics Enrico Fermi*, pp. 317–386, 2013.

[47] D. Bray, *Cell movements: from molecules to motility*. Garland Science, 2001.

[48] H. C. Berg, *E. coli in Motion*. Springer Science & Business Media, 2008.

[49] V. Méndez, D. Campos, and F. Bartumeus, *Stochastic foundations in movement ecology: anomalous diffusion, front propagation and random searches*. Springer Science & Business Media, 2013.

[50] E. Lauga, W. R. DiLuzio, G. M. Whitesides, and H. A. Stone, "Swimming in circles: Motion of bacteria near solid boundaries," *Biophysical Journal*, vol. 90, no. 2, pp. 400–412, 2006.

[51] W. R. DiLuzio, L. Turner, M. Mayer, P. Garstecki, D. B. Weibel, H. C. Berg, and G. M. Whitesides, "Escherichia coli swim on the right-hand side," *Nature*, vol. 435, no. 7046, pp. 1271–1274, 2005.

[52] R. Di Leonardo, D. Dell'Arciprete, L. Angelani, and V. Iebba, "Swimming with an image," *Physical Review Letters*, vol. 106, no. 3, 2011.

[53] P. Galajda, J. Keymer, P. Chaikin, and R. Austin, "A wall of funnels concentrates swimming bacteria," *Journal of Bacteriology*, vol. 189, no. 23, pp. 8704–8707, 2007.

[54] R. Di Leonardo, L. Angelani, D. DellArciprete, G. Ruocco, V. Iebba, S. Schippa, M. P. Conte, F. Mecarini, F. De Angelis, and E. Di Fabrizio, "Bacterial ratchet motors," *Proceedings of the National Academy of Sciences of the United States of America*, vol. 107, no. 21, pp. 9541–9545, 2010.

[55] L. Rothschild, "Non-random distribution of bull spermatozoa in a drop of sperm suspension," *Nature*, vol. 198, no. 488, p. 1221, 1963.

[56] A. P. Berke, L. Turner, H. C. Berg, and E. Lauga, "Hydrodynamic attraction of swimming microorganisms by surfaces," *Physical Review Letters*, vol. 101, no. 3, 2008.

[57] G. Li and J. X. Tang, "Accumulation of microswimmers near a surface mediated by collision and rotational brownian motion," *Physical Review Letters*, vol. 103, no. 7, 2009.

[58] G. Li, J. Bensson, L. Nisimova, D. Munger, P. Mahautmr, J. X. Tang, M. R. Maxey, and Y. V. Brun, "Accumulation of swimming bacteria near a solid surface," *Physical Review E*, vol. 84, no. 4, 2011.

[59] M. Molaei, M. Barry, R. Stocker, and J. Sheng, "Failed escape: Solid surfaces prevent tumbling of escherichia coli," *Physical Review Letters*, vol. 113, no. 6, 2014.

[60] O. Sipos, K. Nagy, R. Di Leonardo, and P. Galajda, "Hydrodynamic trapping of swimming bacteria by convex walls," *Physical Review Letters*, vol. 114, no. 25, 2015.

[61] D. Quéré, *Lectures on capillarity and wetting phenomena*. Post-graduate Course in Science & Engineering of Materials and Nanostructures, University of Padova, March 2015.

[62] A. Marchand, S. Das, J. H. Snoeijer, and B. Andreotti, "Contact angles on a soft solid: From young's law to neumann's law," *Physical Review Letters*, vol. 109, p. 236101, 2012.

[63] R. W. Style and E. R. Dufresne, "Static wetting on deformable substrates, from liquids to soft solids," *Soft Matter*, vol. 8, pp. 7177–7184, 2012.

[64] N. Nuraje, W. S. Khan, Y. Lei, M. Ceylan, and R. Asmatulu, "Superhydrophobic electrospun nanofibers," *Journal of Matererials Chemistry A*, vol. 1, pp. 1929–1946, 2013.

[65] D. Quéré, "Non-sticking drops," *Reports on Progress in Physics*, vol. 68, no. 11, p. 2495, 2005.

[66] C. N. C. Lam, R. Wu, D. Li, M. L. Hair, and A. W. Neumann, "Study of the advancing and receding contact angles: liquid sorption as a cause of contact angle hysteresis," *Advances in Colloid and Interface Science*, vol. 96, no. 1, pp. 169–191, 2002.

[67] C. W. Extrand and S. I. Moon, "Repellency of the lotus leaf: Contact angles, drop retention, and sliding angles," *Langmuir*, vol. 30, no. 29, pp. 8791–8797, 2014.

[68] B. Bhushan and M. Nosonovsky, "The rose petal effect and the modes of superhydrophobicity," *Philosophical Transactions of the Royal Society of London A: Mathematical, Physical and Engineering Sciences*, vol. 368, no. 1929, pp. 4713–4728, 2010.

[69] L. Feng, Y. Zhang, J. Xi, Y. Zhu, N. Wang, F. Xia, and L. Jiang, "Petal effect: a superhydrophobic state with high adhesive force," *Langmuir*, vol. 24, no. 8, pp. 4114–4119, 2008.

[70] D. Quéré, M.-J. Azzopardi, and L. Delattre, "Drops at rest on a tilted plane," *Langmuir*, vol. 14, no. 8, pp. 2213–2216, 1998.

[71] C. Semprebon and M. Brinkmann, "On the onset of motion of sliding drops," *Soft Matter*, vol. 10, no. 18, pp. 3325–3334, 2014.

[72] C. G. L. Furmidge, "Studies at phase interfaces. i. the sliding of liquid drops on solid surfaces and a theory for spray retention," *Journal of Colloid Science*, vol. 17, no. 4, pp. 309–324, 1962.

[73] C. W. Extrand and Y. Kumagai, "Liquid drops on an inclined plane: the relation between contact angles, drop shape, and retentive force," *Journal of Colloid and Interface Science*, vol. 170, no. 2, pp. 515–521, 1995.

[74] N. Le Grand, A. Daerr, and L. Limat, "Shape and motion of drops sliding down an inclined plane," *Journal of Fluid Mechanics*, vol. 541, pp. 293–315, 2005.

[75] S. Suzuki, A. Nakajima, M. Sakai, J.-H. Song, N. Yoshida, Y. Kameshima, and K. Okada, "Sliding acceleration of water droplets on a surface coated with fluoroalkylsilane and octadecyltrimethoxysilane," *Surface Science*, vol. 600, no. 10, pp. 2214–2219, 2006.

[76] T. Podgorski, J.-M. Flesselles, and L. Limat, "Corners, cusps, and pearls in running drops," *Physical Review Letters*, vol. 87, no. 3, p. 036102, 2001.

[77] S. R. Annapragada, J. Y. Murthy, and S. V. Garimella, "Prediction of droplet dynamics on an incline," *International Journal of Heat and Mass Transfer*, vol. 55, no. 5, pp. 1466–1474, 2012.

[78] J. F. Oliver, C. Huh, and S. G. Mason, "Resistance to spreading of liquids by sharp edges," *Journal of Colloid and Interface Science*, vol. 59, no. 3, pp. 568–581, 1977.

[79] T. Tóth, D. Ferraro, E. Chiarello, M. Pierno, G. Mistura, G. Bissacco, and C. Semprebon, "Suspension of water droplets on individual pillars," *Langmuir*, vol. 27, no. 8, pp. 4742–4748, 2011.

[80] R. Lipowsky, "Morphological wetting transitions at chemically structured surfaces," *Current Opinion in Colloid & Interface Science*, vol. 6, no. 1, pp. 40–48, 2001.

[81] K. Khare, S. Herminghaus, J.-C. Baret, B. M. Law, M. Brinkmann, and R. Seemann, "Switching liquid morphologies on linear grooves," *Langmuir*, vol. 23, no. 26, pp. 12997–13006, 2007.

[82] S. Herminghaus, H. Gau, and W. Mönch, "Artificial liquid microstructures," *Advanced Materials*, vol. 11, no. 16, pp. 1393–1395, 1999.

[83] M. Brinkmann and R. Lipowsky, "Wetting morphologies on substrates with striped surface domains," *Journal of Applied Physics*, vol. 92, no. 8, pp. 4296–4306, 2002.

[84] C. Schafle, M. Brinkmann, C. Bechinger, P. Leiderer, and R. Lipowsky, "Morphological wetting transitions at ring-shaped surface domains," *Langmuir*, vol. 26, no. 14, pp. 11878–11885, 2010.

[85] R. Seemann, M. Brinkmann, S. Herminghaus, K. Khare, B. M. Law, S. McBride, K. Kostourou, E. Gurevich, S. Bommer, C. Herrmann, *et al.*, "Wetting morphologies and their transitions in grooved substrates," *Journal of Physics: Condensed Matter*, vol. 23, no. 18, p. 184108, 2011.

[86] M. Struwe, *Plateau's Problem and the Calculus of Variations*. Princeton University Press, 1988.

[87] S. L. Goren, "The shape of a thread of liquid undergoing break-up," *Journal of Colloid Science*, vol. 19, no. 1, pp. 81–86, 1964.

[88] L. Kelvin *Mathematical and Physical Papers*, vol. 3, p. 384, 1890.

[89] L. Rayleigh, *The Theory of Sound*. Macmillan, New York, 1894.

[90] H. Lamb, *Hydrodynamics*. Cambridge University Press, 1932.

[91] L. D. Landau and E. M. Lifshits, *Fluid Mechanics*. Pergamon Press, 1959.

[92] H. Rodot, C. Bisch, and A. Lasek, "Zero-gravity simulation of liquids in contact with a solid surface," *Acta Astronautica*, vol. 6, no. 9, pp. 1083–1092, 1979.

[93] M. Strani and F. Sabetta, "Free vibrations of a drop in partial contact with a solid support," *Journal of Fluid Mechanics*, vol. 141, pp. 233–247, 1984.

[94] F. Celestini and R. Kofman, "Vibration of submillimeter-size supported droplets," *Physical Review E*, vol. 73, no. 4, p. 041602, 2006.

[95] X. Noblin, A. Buguin, and F. Brochard-Wyart, "Vibrated sessile drops: Transition between pinned and mobile contact line oscillations," *The European Physical Journal E*, vol. 14, no. 4, pp. 395–404, 2004.

[96] L. Dong, A. Chaudhury, and M. K. Chaudhury, "Lateral vibration of a water drop and its motion on a vibrating surface," *The European Physical Journal E*, vol. 21, no. 3, pp. 231–242, 2006.

[97] R. H. Temperton and J. S. Sharp, "Vibrational modes of elongated sessile liquid droplets," *Langmuir*, vol. 29, no. 15, pp. 4737–4742, 2013.

[98] R. H. Temperton, *Resonant vibrations of microlitre liquid drops.* PhD thesis, University of Nottingham, 2013.

[99] X. Noblin, A. Buguin, and F. Brochard-Wyart, "Triplon modes of puddles," *Physical Review Letters*, vol. 94, no. 16, p. 166102, 2005.

[100] K. A. Brakke, "The surface evolver," *Experimental Mathematics*, vol. 1, no. 2, pp. 141–165, 1992.

[101] S. Daniel, S. Sircar, J. Gliem, and M. K. Chaudhury, "Ratcheting motion of liquid drops on gradient surfaces," *Langmuir*, vol. 20, no. 10, pp. 4085–4092, 2004.

[102] P. Sartori, D. Quagliati, S. Varagnolo, M. Pierno, G. Mistura, F. Magaletti, and C. M. Casciola, "Drop motion induced by vertical vibrations," *New Journal of Physics*, vol. 17, no. 11, p. 113017, 2015.

[103] E. Rio, A. Daerr, F. Lequeux, and L. Limat, "Moving contact lines of a colloidal suspension in the presence of drying," *Langmuir*, vol. 22, no. 7, pp. 3186–3191, 2006.

[104] S. Varagnolo, D. Ferraro, P. Fantinel, M. Pierno, G. Mistura, G. Amati, L. Biferale, and M. Sbragaglia, "Stick-slip sliding of water drops on chemically heterogeneous surfaces," *Physical Review Letters*, vol. 111, no. 6, p. 066101, 2013.

[105] S. Suzuki, A. Nakajima, M. Sakai, A. Hashimoto, N. Yoshida, Y. Kameshima, and K. Okada, "Rolling and slipping motion of a water droplet sandwiched between two parallel plates coated with fluoroalkylsilanes," *Applied Surface Science*, vol. 255, no. 5, pp. 3414–3420, 2008.

[106] A. Nakajima, Y. Nakagawa, T. Furuta, M. Sakai, T. Isobe, and S. Matsushita, "Sliding of water droplets on smooth hydrophobic silane coatings with regular triangle hydrophilic regions," *Langmuir*, vol. 29, no. 29, pp. 9269–9275, 2013.

[107] M. K. Chaudhury and G. M. Whitesides, "How to make water run uphill," *Science*, vol. 256, no. 5063, pp. 1539–1541, 1992.

[108] N. Savva and S. Kalliadasis, "Droplet motion on inclined heterogeneous substrates," *Journal of Fluid Mechanics*, vol. 725, pp. 462–491, 2013.

[109] D. Quéré, "Leidenfrost dynamics," *Annual Review of Fluid Mechanics*, vol. 45, pp. 197–215, 2013.

[110] P. Brunet, J. Eggers, and R. D. Deegan, "Motion of a drop driven by substrate vibrations," *The European Physical Journal Special Topics*, vol. 166, no. 1, pp. 11–14, 2009.

[111] K. John and U. Thiele, "Self-ratcheting stokes drops driven by oblique vibrations," *Physical Review Letters*, vol. 104, no. 10, p. 107801, 2010.

[112] E. S. Benilov and J. Billingham, "Drops climbing uphill on an oscillating substrate," *Journal of Fluid Mechanics*, vol. 674, pp. 93–119, 2011.

[113] E. S. Benilov, "Thin three-dimensional drops on a slowly oscillating substrate," *Physical Review E*, vol. 84, no. 6, p. 066301, 2011.

[114] P. Seppecher, "Moving contact lines in the cahn-hilliard theory," *International Journal of Engineering Science*, vol. 34, no. 9, pp. 977–992, 1996.

[115] D. Jacqmin, "Contact-line dynamics of a diffuse fluid interface," *Journal of Fluid Mechanics*, vol. 402, pp. 57–88, 2000.

[116] X. Yang, J. J. Feng, C. Liu, and J. Shen, "Numerical simulations of jet pinching-off and drop formation using an energetic variational phase-field method," *Journal of Computational Physics*, vol. 218, no. 1, pp. 417–428, 2006.

[117] Y. Sui, H. Ding, and P. D. M. Spelt, "Numerical simulations of flows with moving contact lines," *Annual Review of Fluid Mechanics*, vol. 46, pp. 97–119, 2014.

[118] J. Lee, S. W. Son, M. Y. Ha, and H. R. Kim, "A numerical study on the dynamic behavior of the liquid located between pillar-shaped structures," *Journal of Mechanical Science and Technology*, vol. 28, no. 10, pp. 4221–4232, 2014.

[119] M. Sbragaglia, L. Biferale, G. Amati, S. Varagnolo, D. Ferraro, G. Mistura, and M. Pierno, "Sliding drops across alternating hydrophobic and hydrophilic stripes," *Physical Review E*, vol. 89, no. 1, p. 012406, 2014.

[120] X.-P. Wang, T. Qian, and P. Sheng, "Moving contact line on chemically patterned surfaces," *Journal of Fluid Mechanics*, vol. 605, pp. 59–78, 2008.

[121] J.-B. Dupont and D. Legendre, "Numerical simulation of static and sliding drop with contact angle hysteresis," *Journal of Computational Physics*, vol. 229, no. 7, pp. 2453–2478, 2010.

[122] N. Galvanetto, *Studio preliminare del moto di una goccia indotto da vibrazioni del substrato.* Bachelor thesis, Università degli Studi di Padova, 2011/2012.

[123] D. Stefani, *Moto di una goccia indotto da vibrazioni del substrato.* Bachelor thesis, Università degli Studi di Padova, 2011/2012.

[124] V. Chilese, *Moto unidimensionale di una goccia indotto da vibrazioni del substrato.* Bachelor thesis, Università degli Studi di Padova, 2012/2013.

[125] I. S. Khattab, F. Bandarkar, M. A. A. Fakhree, and A. Jouyban, "Density, viscosity, and surface tension of water + ethanol mixtures from 293 to 323k," *Korean Journal of Chemical Engineering*, vol. 29, no. 6, pp. 812–817, 2012.

[126] Glycerine Producers' Association, *Physical Properties of Glycerine and Its Solutions*, 1963.

[127] F. Magaletti, F. Picano, M. Chinappi, L. Marino, and C. M. Casciola, "The sharp-interface limit of the cahn–hilliard/navier–stokes model for binary fluids," *Journal of Fluid Mechanics*, vol. 714, pp. 95–126, 2013.

[128] A. Carlson, G. Bellani, and G. Amberg, "Contact line dissipation in short-time dynamic wetting," *EPL (Europhysics Letters)*, vol. 97, no. 4, p. 44004, 2012.

[129] D. E. Kataoka and S. M. Troian, "Patterning liquid flow on the microscopic scale," *Nature*, vol. 402, no. 6763, pp. 794–797, 1999.

[130] A. del Campo and C. Greiner, "Su-8: a photoresist for high-aspect-ratio and 3d submicron lithography," *Journal of Micromechanics and Microengineering*, vol. 17, no. 6, p. R81, 2007.

[131] Y. Xia and G. M. Whitesides, "Soft lithography," *Annual Review of Materials Science*, vol. 28, no. 1, pp. 153–184, 1998.

[132] D. Bodas and C. Khan-Malek, "Hydrophilization and hydrophobic recovery of pdms by oxygen plasma and chemical treatmentan sem investigation," *Sensors and Actuators B: Chemical*, vol. 123, no. 1, pp. 368–373, 2007.

[133] S. Ramaswamy, "The mechanics and statistics of active matter," *Annual Review of Condensed Matter Physics*, vol. 1, pp. 323–345, 2010.

[134] E. M. Purcell, "Life at low reynolds number," *American Journal of Physics*, vol. 45, no. 1, pp. 3–11, 1977.

[135] M. Polin, I. Tuval, K. Drescher, J. P. Gollub, and R. E. Goldstein, "Chlamydomonas swims with two gears in a eukaryotic version of run-and-tumble locomotion," *Science*, vol. 325, no. 5939, pp. 487–490, 2009.

[136] E. Lauga and R. E. Goldstein, "Dance of the microswimmers," *Physics Today*, vol. 65, no. 9, p. 30, 2012.

[137] A. Walther and A. H. Müller, "Janus particles," *Soft Matter*, vol. 4, no. 4, pp. 663–668, 2008.

[138] Y. Hong, D. Velegol, N. Chaturvedi, and A. Sen, "Biomimetic behavior of synthetic particles: from microscopic randomness to macroscopic control," *Physical Chemistry Chemical Physics*, vol. 12, no. 7, pp. 1423–1435, 2010.

[139] J. Adler, "Chemotaxis in escherichia coli," *Cold Spring Harbor Symposia on Quantitative Biology*, no. 30, p. 28992, 1965.

[140] J. S. Schuhmacher, K. M. Thormann, and G. Bange, "How bacteria maintain location and number of flagella?," *FEMS Microbiology Reviews*, p. fuv034, 2015.

[141] J. Perrin, *Atoms*. Translated by D. Ll. Hammick, Constable, London, 1920, 1913.

[142] A. Einstein, *Investigations on the Theory of the Brownian Movement*. Dover Publications, New York, 1926.

[143] P. Langevin, "Sur la théorie du mouvement brownien," *CR Acad. Sci. Paris*, vol. 146, no. 530-533, p. 530, 1908.

[144] G. E. Uhlenbeck and L. S. Ornstein, "On the theory of the brownian motion," *Physical Review*, vol. 36, no. 5, p. 823, 1930.

[145] H. C. Berg, *Random walks in biology*. Princeton University Press, 1993.

[146] H. Matsuoka, H. Morikawa, and H. Yamaoka, "Rotational diffusion of ellipsoidal latex particles in dispersion as studied by depolarized dynamic light scattering," *Colloids and Surfaces A: Physicochemical and Engineering Aspects*, vol. 109, pp. 137–145, 1996.

[147] E. Lauga and T. R. Powers, "The hydrodynamics of swimming microorganisms," *Reports on Progress in Physics*, vol. 72, no. 9, p. 096601, 2009.

[148] J. Elgeti, R. G. Winkler, and G. Gompper, "Physics of microswimmerssingle particle motion and collective behavior: a review," *Reports on Progress in Physics*, vol. 78, no. 5, p. 056601, 2015.

[149] H. C. Berg and R. A. Anderson, "Bacteria swim by rotating their flagellar filaments," *Nature*, vol. 245, no. 5425, pp. 380–2, 1973.

[150] M. T. Madigan, J. M. Martinko, D. A. Stahl, and D. P. Clark, *Brock Biology of Microorganisms*. Benjamin Cummings, 2010.

[151] J. Taktikos, H. Stark, and V. Zaburdaev, "How the motility pattern of bacteria affects their dispersal and chemotaxis," *PLoS ONE*, vol. 8, no. 12, p. e81936, 2013.

[152] B. L. Taylor and D. E. J. Koshland, "Reversal of flagellar rotation in monotrichous and peritrichous bacteria: generation of changes in direction," *Journal of Bacteriology*, vol. 119, no. 2, pp. 640–2, 1974.

[153] R. Stocker, "Reverse and flick: Hybrid locomotion in bacteria," *Proceedings of the National Academy of Sciences of the United States of America*, vol. 108, no. 7, pp. 2635–2636, 2011.

[154] C. Qian, C. C. Wong, S. Swarup, and K.-H. Chiam, "Bacterial tethering analysis reveals a "run-reverse-turn" mechanism for pseudomonas species motility," *Applied and Environmental Microbiology*, vol. 79, no. 15, pp. 4734–4743, 2013.

[155] L. Xie, T. Altindal, S. Chattopadhyay, and X.-L. Wu, "Bacterial flagellum as a propeller and as a rudder for efficient chemotaxis," *Proceedings of the National Academy of Sciences of the United States of America*, vol. 108, no. 6, pp. 2246–2251, 2011.

[156] J. Maennik, R. Driessen, P. Galajda, J. E. Keymer, and C. Dekker, "Bacterial growth and motility in sub-micron constrictions," *Proceedings of the National Academy of Sciences of the United States of America*, vol. 106, no. 35, pp. 14861–14866, 2009.

[157] L. Angelani, R. Di Leonardo, and G. Ruocco, "Self-starting micromotors in a bacterial bath," *Physical Review Letters*, vol. 102, no. 4, p. 048104, 2009.

[158] H. C. Berg and D. A. Brown, "Chemotaxis in escherichia coli analysed by three-dimensional tracking," *Nature*, vol. 239, no. 5374, pp. 500–4, 1972.

[159] P. D. Frymier, R. M. Ford, H. C. Berg, and P. T. Cummings, "Three-dimensional tracking of motile bacteria near a solid planar surface," *Proceedings of the National Academy of Sciences of the United States of America*, vol. 92, no. 13, pp. 6195–6199, 1995.

[160] I. D. Vladescu, E. J. Marsden, J. Schwarz-Linek, V. A. Martinez, J. Arlt, A. N. Morozov, D. Marenduzzo, M. E. Cates, and W. C. K. Poon, "Filling an emulsion drop with motile bacteria," *Physical Review Letters*, vol. 113, no. 26, 2014.

[161] N. Dasgupta, M. C. Wolfgang, A. L. Goodman, S. K. Arora, J. Jyot, S. Lory, and R. Ramphal, "A four-tiered transcriptional regulatory circuit controls flagellar biogenesis in pseudomonas aeruginosa," *Molecular Microbiology*, vol. 50, no. 3, pp. 809–824, 2003.

[162] J. Schwarz-Linek, J. Arlt, A. Jepson, A. Dawson, T. Vissers, D. Miroli, T. Pilizota, V. A. Martinez, and W. C. K. Poon, "Escherichia coli as a model active colloid: A practical introduction," *Colloids and Surfaces B: Biointerfaces*, vol. 137, pp. 2–16, 2016.

[163] C. S. Barker, B. M. Pruss, and P. Matsumura, "Increased motility of escherichia coli by insertion sequence element integration into the regulatory region of the flhd operon," *Journal of Bacteriology*, vol. 186, no. 22, pp. 7529–7537, 2004.

[164] G. Mino, T. E. Mallouk, T. Darnige, M. Hoyos, J. Dauchet, J. Dunstan, R. Soto, Y. Wang, A. Rousselet, and E. Clement, "Enhanced diffusion due to active swimmers at a solid surface," *Physical Review Letters*, vol. 106, no. 4, 2011.

[165] H. M. Lopez, J. Gachelin, C. Douarche, H. Auradou, and E. Clement, "Turning bacteria suspensions into superfluids," *Physical Review Letters*, vol. 115, no. 2, 2015.

[166] E. Bulard, M.-P. Fontaine-Aupart, H. Dubost, W. Zheng, M.-N. Bellon-Fontaine, J.-M. Herry, and B. Bourguignon, "Competition of bovine serum albumin adsorption and bacterial adhesion onto surface-grafted odt: In situ study by vibrational sfg and fluorescence confocal microscopy," *Langmuir*, vol. 28, no. 49, pp. 17001–17010, 2012.

[167] M. C. M. Vanloosdrecht, W. Norde, J. Lyklema, and A. J. B. Zehnder, "Hydrophobic and electrostatic parameters in bacterial adhesion," *Aquatic Sciences*, vol. 52, no. 1, pp. 103–114, 1990.

[168] T. B. Doyle, A. C. Hawkins, and L. L. McCarter, "The complex flagellar torque generator of pseudomonas aeruginosa," *Journal of Bacteriology*, vol. 186, no. 19, pp. 6341–6350, 2004.

[169] C. Valeriani, M. Li, J. Novosel, J. Arlt, and D. Marenduzzo, "Colloids in a bacterial bath: simulations and experiments," *Soft Matter*, vol. 7, no. 11, pp. 5228–5238, 2011.

[170] A. Suma, G. Gonnella, D. Marenduzzo, and E. Orlandini, "Motility-induced phase separation in an active dumbbell fluid," *EPL (Europhysics Letters)*, vol. 108, p. 56004, 2014.

[171] J. Elgeti and G. Gompper, "Self-propelled rods near surfaces," *EPL (Europhysics Letters)*, vol. 85, no. 3, 2009.

[172] J. Elgeti and G. Gompper, "Wall accumulation of self-propelled spheres," *EPL (Europhysics Letters)*, vol. 101, no. 4, 2013.

[173] E. Locatelli, F. Baldovin, E. Orlandini, and M. Pierno, "Active brownian particles escaping a channel in single file," *Physical Review E*, vol. 91, p. 022109, 2015.

[174] E. Locatelli, M. Pierno, F. Baldovin, E. Orlandini, Y. Tan, and S. Pagliara, "Single-file escape of colloidal particles from microfluidic channels," *Physical Review Letters*, vol. 117, p. 038001, 2016.

[175] M. J. Madou, *Fundamentals of microfabrication: the science of miniaturization*. CRC press, 2002.

[176] J. C. McDonald, D. C. Duffy, J. R. Anderson, D. T. Chiu, H. Wu, O. J. A. Schueller, and G. M. Whitesides, "Fabrication of microfluidic systems in poly(dimethylsiloxane)," *Electrophoresis*, vol. 21, no. 1, pp. 27–40, 2000.

[177] MicroChem Corporation, *Processing guideline for SU-8 2025-2075*. `http://www.microchem.com/Prod-SU82000.htm`.

[178] I. Wong and C.-M. Ho, "Surface molecular property modifications for poly(dimethylsiloxane) (pdms) based microfluidic devices," *Microfluidics and Nanofluidics*, vol. 7, no. 3, p. 291, 2009.

[179] J. Zhou, D. A. Khodakov, A. V. Ellis, and N. H. Voelcker, "Surface modification for pdms-based microfluidic devices," *Electrophoresis*, vol. 33, no. 1, pp. 89–104, 2012.

[180] M. Yao and J. Fang, "Hydrophilic peo-pdms for microfluidic applications," *Journal of Micromechanics and Microengineering*, vol. 22, no. 2, p. 025012, 2012.